Thermoelectric Transport in Ionic Conducting Copper and Silver Chalcogenides

Dissertation

zur Erlangung des akademischen Grades
"Doktor der Naturwissenschaften"

am Fachbereich Chemie,
Pharmazie und Geowissenschaften der

Johannes Gutenberg-Universität Mainz

Kai Weldert
[redacted]

Mainz 2015

[redacted]

Für meine Familie

[redacted]

Publications

[1] **Weldert K.S.**, Zeier W.G., Panthöfer M., Snyder G.J., Tremel W. "Thermoelectric and Structural Properties of the Argyrodite Ag_8SiSe_6" *in preparation*.

[2] **Weldert K.S.**, Zeier W.G., Zhou S., Gaultois M., Melot B.C., Delaire O., Snyder G.J., Tremel W. "Low Temperature Transport and Anomalously Low Thermal Conductivity of Cu_7PSe_6" *in preparation*.

[3] **Weldert K.S.**, Day T., Zeier W.G., Hanus R., Chen B.-R., Panthöfer M., Bedzyk M.J., Tremel W., Snyder G.J. "Influence of Compensating Defect Formation on the Doping Efficiency and Thermoelectric Properties of $Cu_{2-y}Se_{1-x}Br_x$" *Chem. Mater.* **2015**, *under revision.*

[4] **Weldert K.S.**, Zeier W.G., Day T.W., Panthöfer M., Snyder G.J., Tremel W., "Thermoelectric Transport in Cu_7PSe_6 with High Copper Ionic Mobility" *J. Am. Chem. Soc.* **2014**, 136 (34), 12035-12040, doi:10.1021/ja5056092.

[5] Kieslich G., Veremchuck I., Antonyshyn I., Zeier W.G., Birkel C.S., **Weldert K.S.**, Heinrich C.P., Visnow E., Panthöfer M., Burkhard U., Grin Y., Tremel W. "Using Crystallographic Shear to Reduce Lattice Thermal Conductivity: High Temperature Thermoelectric Characterization of the Spark Plasma Sintered Magneli Phases $WO_{2.90}$ and $WO_{2.722}$" *Phys. Chem. Chem. Phys.* **2013**, 15, 15399-15403, doi:10.1039/C3CP52361F.

Acknowledgments

[redacted]

[redacted]

Contents

List of Figures

List of Tables

List of Symbols, Notations and Abbreviations

a	-	lattice parameter
α	-	thermal diffusivity
a_T	-	linear coefficient of thermal expansion
B	-	quality factor
ΔB	-	altering magnetic field
BTE	-	Boltzmann transport equations
B_T	-	isothermal bulk modulus
C	-	heat capacity / specific heat
C_V	-	specific heat per unit volume
d	-	density
ΔT	-	temperature difference
DOS	-	density of states
DSC	-	differential scanning calorimetry
E	-	electric field
E_g	-	band gap
$E(\vec{k})$	-	band dispersion
E_A	-	activation energy
e	-	electron charge
ϵ	-	reduced carrier energy
ϵ_F	-	Fermi energy
f	-	distribution function
f_0	-	distribution function at equilibrium
f_{FD}	-	Fermi-Dirac distribution function
f_{MB}	-	Maxwell-Boltzmann distribution function
f_i	-	fraction of atoms i
G_m	-	mass disorder scattering parameter
G_S	-	strain disorder scattering parameter
γ	-	Grüneisen parameter
h	-	Planck constant
η	-	reduced electrochemical potential
η_C	-	Carnot efficiency

ICP-MS	-	inductively coupled plasma mass spectrometry
k_B	-	Boltzmann constant
$\vec{k}$	-	electron wave vector
κ	-	thermal conductivity
κ_{lat}	-	lattice thermal conductivity
κ_{el}	-	electronic thermal conductivity
κ_{min}	-	minimum lattice thermal conductivity
l	-	thickness
L	-	Lorenz number
Λ	-	phonon mean free path
LFA	-	laser flash analysis
λ	-	scattering parameter
M	-	molecular weight
m^*	-	effective mass
m^*_b	-	band effective mass
m^*_d	-	density of states effective mass
μ	-	charge carrier mobility
μ_H	-	Hall mobility
μ	-	intrinsic carrier mobility
n_{atom}	-	number of atoms
N_A	-	Avogadro constant
N_V	-	band degeneracy
$N(E)$	-	density of states
n	-	charge carrier concentration/density
n_H	-	Hall carrier concentration
Ξ	-	deformation potential
v	-	wave number
v_d	-	drift velocity
v_g	-	phonon group velocity
p	-	momentum
P	-	power
PF	-	power factor
q_J	-	Joule heat

q	-	heat flow
$\vec{r}$	-	location vector
R_{id}	-	ideal gas constant
R	-	total Resistance
R_H	-	Hall coefficient
R_{wp}	-	profile residual
r_H	-	Hall factor
ρ	-	electrical resistivity
S	-	Seebeck coefficient / thermopower
σ	-	electrical conductivity
T	-	temperature
T_C	-	temperature on the cold side
T_H	-	temperature on the hot side
TGA	-	thermogravimetric analysis
τ	-	phonon scattering relaxation time
τ_N	-	phonon scattering relaxation time for normal scattering
τ_U	-	phonon scattering relaxation time for Umklapp scattering
τ_B	-	phonon scattering relaxation time for boundary scattering
τ_{PD}	-	phonon scattering relaxation time for point defect scattering
τ_{EP}	-	phonon scattering relaxation time for electron-phonon scattering
Θ_D	-	Debye temperature
U	-	alloy scattering potential
V	-	voltage
V_{atom}	-	average volume per atom
V_0	-	minimum band energy
v_d	-	electron drift velocity
v_g	-	phonon group velocity
v_m	-	average velocity of sound
v_l	-	longitudinal speed of sound
v_t	-	transverse speed of sound
XPS	-	x-ray photoelectron spectroscopy
XRD	-	x-ray diffraction
XRF	-	x-ray fluorescence

ZT	-	device thermoelectric figure of merit
zT	-	materials thermoelectric figure of merit
Z	-	formula units per unit cell
ω	-	phonon frequency
ω_D	-	Debye frequency

Abstract

In order to avoid a serious energy crisis in the future, alternative energy sources are required and new, powerful approaches have to be explored to use current energy technologies more efficiently. Based on Seebeck and Peltier effects, thermoelectric materials either convert thermal to electrical energy or vice versa, providing a perspective for both power generation and refrigeration applications, respectively.

The thermoelectric efficiency is governed by the thermoelectric figure of merit $zT = S^2(\rho\kappa)^{-1}T$, and the last decade has seen the discovery of many suitable materials for thermoelectric power generation. In this context the "phonon-glass electron-crystal" (PGEC) concept has proven to be very useful for the exploration of new thermoelectric materials. According to this concept, a good thermoelectric material requires an optimized charge carrier concentration and a low lattice thermal conductivity which can be fulfilled by merging two fractional or structural units responsible for the electronic and thermal properties. In recent years, the PGEC concept has been applied to superionic compounds like Cu_2Se, Cu_2S, Ag_2Se which achieve very high thermoelectric efficiencies. Here, the concept of "phonon-liquid electron-crystal" (PLEC) thermoelectrics has been introduced as an extension of the "phonon-glass electron-crystal" concept because these materials are usually built up of a very simple anion network in which the cations are highly disordered with liquid-like mobility leading to very low lattice thermal conductivities.

It is the goal of this work to discuss structural aspects of several ionic conducting materials and the relations to the thermoelectric transport properties. In order to obtain a deeper understanding of structure-property relationships in these materials, we have investigated different series of solid solutions and discussed the influence of dopants in ionic conducting materials.

The superionic conductor $Cu_{2-\delta}Se$ has proven to be a promising thermoelectric at higher temperatures. Being the best-studied ionic conducting thermoelectric material, it is also the subject of critical discussions, since certain issues concerning chemical stability need to be addressed before a possible application. After a general introduction we present the potential of copper selenide to achieve a high figure of merit at room temperature, if the intrinsically high hole carrier concentration can be reduced. Using bromine as a dopant we show that reducing the charge carrier concentration in $Cu_{2-\delta}Se$ is in fact

possible. Furthermore we provide profound insight in the complex defect chemistry of bromine doped $Cu_{2-\delta}Se$ via various analytical methods and investigate the consequential influences on the thermoelectric transport properties. Here we show, for the first time, the effect of copper vacancy formation as compensating defects when moving the Fermi level closer to the valence band edge. These compensating defects provide an explanation for frequently observed doping inefficiencies in thermoelectrics via defect chemistry and guiding further progress in the development of new thermoelectric materials.

Building on the good thermoelectric performances of the binary superionic compounds, a better and more detailed understanding of PLEC thermoelectric materials is desirable. Therefore, we investigate the thermoelectric transport properties of the compound Cu_7PSe_6 as the first representative of the class of more complex Argyrodite-type copper ion conducting thermoelectrics. The Argyrodite family is well known for a huge variety of compositions, which can even be increased by varying the oxidation states leading to both ternary and quaternary compounds. Therefore, the Argyrodites provide a huge playground for the investigation of structure-property relationships, making this class of materials a well-suited model system for PLEC thermoelectric materials.

The further research on Argyrodite-type compounds addresses the effects of structural aspects on the thermoelectric transport. For this purpose the series of solid solutions $(Cu,Ag)_7PSe_6$ is considered. In this context both the influence of the substitution of copper and silver and the influence of the order-disorder-transitions above room temperature on the thermoelectric properties can be investigated. Here, the Argyrodites are well suitable, since cation substitutions are possible which is much more difficult in binary systems. Within the scope of the investigation of Argyrodite type samples, the influence of the amount of mobile cations per formula unit on the thermoelectric properties can also be investigated. Here, Ag_8SiSe_6 is regarded, which shows outstanding thermoelectric transport properties at temperatures close to room temperature, in combination with very high charge carrier mobility and a complex structure.

The remainder of this thesis focusses on compounds similar to chalcopyrite, which crystallizes in a tetrahedrally bonded network structure. Chalcopyrite-type compounds achieve extremely high thermoelectric efficiencies. $AgGaTe_2$, $CuGaTe_2$ and $CuInTe_2$ are prominent examples for ternary chalcopyrite-type thermoelectric materials with high efficiencies. $CuFeTe_2$, however, crystallizes in a layered structure. In addition to the tetrahedral bonded ions within the layers, it provides additional pyramidal cation sites between

the layers leading to compositions with variable amounts of cations ($Cu_{1+x}Fe_{1+y}Te_2$). As the phase pure bulk synthesis of this compound is difficult, there is hardly any report on the physical properties of these compounds. In this context a method for the phase pure bulk synthesis of this compound is developed and the thermoelectric properties of this series of solid solutions $Cu_{1+x}Fe_{1+y}Te_2$ are investigated with regard to changes in x and y.

Zusammenfassung

Um eine drohende Energiekrise in naher Zukunft zu verhindern, wird neben alternativen Energiequellen vor allem nach Möglichkeiten gesucht, die vorhandenen Energietechnologien effizienter zu nutzen. Basierend auf dem Seebeck und Peltier Effekt, erlauben thermoelektrische Materialien eine direkte Umwandlung von thermischer in elektrische Energie und ermöglichen damit potentielle Anwendungen im Bereich der Erzeugung elektrischer Energie sowie der Kältetechnik.

Im Laufe der letzten Jahrzehnte wurden zahlreiche Materialien entwickelt, die eine hohe Effizienz zur elektrischen Energieerzeugung aufweisen, welche wiederum durch die thermoelektrische Gütezahl $zT = S^2(\rho\kappa)^{-1}T$ bestimmt wird. In diesem Zusammenhang wurde auch der Begriff des „phonon-glass electron-crystal“ (PGEC) Konzepts geprägt, welches äußerst nützlich für die Entdeckung neuer thermoelektrischer Materialien ist. Nach diesem Konzept benötigt ein gutes thermoelektrisches Material zum einen eine ausgeglichene Ladungsträgerkonzentration und zum anderen eine geringe Gitterwärmeleitfähigkeit. Dieser Zusammenhang ist üblicherweise nur in Materialien erfüllt, welche aus zwei strukturellen Untereinheiten aufgebaut sind, von denen die eine für die elektronischen und die andere für die thermischen Eigenschaften verantwortlich ist. Vor einigen Jahren wurde das PGEC Konzept auf superionische Verbindungen wie Cu_2Se, Cu_2S, Ag_2Se angewendet, welche sehr hohe thermoelektrische Effizienz aufweisen. In diesem Zusammenhang wurde der Begriff des „phonon-liquid electron-crystal“ (PLEC) Konzepts als Erweiterung des „phonon-glass electron-crystal“ Konzepts eingeführt, da diese Materialien aus einem einfachen Anionennetzwerk aufgebaut sind, in dem sich die Kationen einer Flüssigkeit gleich bewegen können. Dies hat eine außerordentlich geringe Gitterwärmeleitfähigkeit zur Folge.

Es ist das Ziel dieser Arbeit, strukturelle Aspekte verschiedener ionenleitender Materialien zu untersuchen und Beziehungen zu den thermoelektrischen Eigenschaften herzustellen. Um ein tieferes Verständnis der Struktur-Eigenschaftsbeziehungen innerhalb dieser Materialklasse zu erhalten werden verschiedene Reihen fester Lösungen hergestellt und deren thermoelektrische Eigenschaften ermittelt sowie der Einfluss von Dotierungen auf ionisch leitende Materialien untersucht.

Kupfer(I)selenid ist ein Kupferionenleiter mit vielversprechenden thermoelektrischen Eigenschaften bei hohen Temperaturen und gilt in diesem Zusammenhang als einer

der am besten untersuchten Ionenleiter als Thermoelektrikum. Auf der anderen Seite ist diese Verbindung auch Gegenstand kritischer Diskussionen, da vor einer möglichen Anwendung Probleme bezüglich der chemischen Stabilität bei hohen Temperaturen gelöst werden müssen.

Nach einer generellen Einführung wird zunächst das Potential der Verbindung erörtert, eine hohe thermoelektrische Effizienz auch bei niedrigen Temperaturen zu erreichen. Dies ist unter der Voraussetzung möglich, dass die durch intrinsische Fehlstellen hohe Loch-Ladungsträgerkonzentration mittels Dotierung verringert werden kann. Im Folgenden wird demonstriert, dass eine Reduktion der Ladungsträgerkonzentration in Kupfer(I)selenid durch Dotierung mit Bromid-Ionen tatsächlich möglich ist. Im Zuge dessen geben wir unter Verwendung zahlreicher analytischer Methoden einen detaillierten Einblick in die komplexe Defektchemie dieser Verbindung und untersuchen die daraus folgenden Einflüsse auf die thermoelektrischen Eigenschaften. Wir zeigen hier erstmals den Effekt der Bildung von Kupferfehlstellen, die beim Verschieben des Fermi-Niveaus zur Unterkante des Valenzbandes auftritt. Die entstehenden „Killer-Defekte“ liefern eine Erklärung für eine reduzierte Effizienz der Dotierung, welche häufig in dotierten Chalkogeniden beobachtet wird. Eine Übertragung der hier erhaltenen Ergebnisse auf andere Systeme kann daher bei der Entwicklung neuartiger thermoelektrischer Materialien hilfreich sein.

Aufbauend auf der hohen Leistungsfähigkeit dieser binären Verbindungen soll im Rahmen dieser Arbeit auch ein besseres generelles Verständnis von PLEC Materialien erreicht werden. Aus diesem Grund werden in den folgenden Kapiteln die thermoelektrischen Eigenschaften des Argyrodits Cu_7PSe_6 untersucht, bei dem es sich um eine komplexere, superionische Verbindung handelt. Durch die große Vielfalt an möglichen Zusammensetzungen eignen sich Argyrodite ideal für die Untersuchung von Struktur-Eigenschaftsbeziehungen und machen sie zu einem geeigneten Modellsystem für PLEC thermoelektrische Materialien.

Diesbezüglich wird in den folgenden Abschnitten ebenfalls der Einfluss struktureller Aspekte auf die thermoelektrischen Eigenschaften der Argyrodite untersucht. Zu diesem Zweck wird eine Reihe fester Lösungen mit der Zusammensetzung $(Cu,Ag)_7PSe_6$ betrachtet, an welcher zum einen die Auswirkung des Austausches von Kupfer gegen Silber und zum anderen der Einfluss von Phasenübergängen auf die thermoelektrischen Eigenschaften untersucht wird. Die Argyrodite eignen sich in diesem Fall besonders gut,

da hier Substitutionen im Kationenuntergitter möglich sind, während in binären Systemen häufig Phasensegregationen auftreten. Zusätzlich erlauben Argyrodite die Untersuchung des Einflusses der Menge mobiler Kationen pro Formeleinheit auf die thermoelektrischen Transporteigenschaften. Zu diesem Zweck wird die Verbindung Ag_8SiSe_6 untersucht, welche außergewöhnlich gute thermoelektrische Transporteigenschaften bei niedrigen Temperaturen in Kombination mit hoher Ladungsträgermobilität besitzt.

Das letzte Kapitel dieser Arbeit beschäftigt sich mit Verbindungen, welche in einer für Chalkopyrit charakteristischen, tetraedrisch koordinierten Netzwerkstruktur kristallisieren. Zahlreiche Chalkopyrit-artige Verbindungen besitzen sehr gute thermoelektrische Eigenschaften wie beispielsweise $AgGaTe_2$, $CuGaTe_2$ und $CuInTe_2$. Die Verbindung $CuFeTe_2$ hingegen kristallisiert in einer schichtförmigen Struktur, die zwar innerhalb der Schichten tetraedrisch koordiniert ist, jedoch zwischen den Schichten zusätzliche quadratisch-pyramidal koordinierte Kationenplätze aufweist. Dieser Aufbau macht Zusammensetzungen mit variablem Kationengehalt ($Cu_{1+x}Fe_{1+y}Te_2$) möglich. Bisher existieren nur wenige Veröffentlichungen über physikalische Eigenschaften dieser Verbindung. In diesem Zusammenhang wurde im Rahmen dieser Arbeit zunächst die Methode zur phasenreinen Synthese der Verbindung mit variablem Kationengehalt entwickelt und die thermoelektrischen Eigenschaften der Verbindungen in Abhängigkeit vom Kationengehalt untersucht.

Chapter 1

Introduction

Thermoelectric materials are able to generate electricity from a temperature gradient. This chapter will give a brief introduction on thermoelectricity and discuss the materials properties influencing the efficiency of thermoelectric energy conversion. Within the last years many suitable materials have been discovered exhibiting high thermoelectric efficiencies, mirrored by the dimensionless thermoelectric figure of merit zT. For a wide technical application zT values of 2-3 are necessary, but the zT values for commercial available thermoelectric materials vary around 0.8 with an efficiency of about 5-6 %.[1] Research focusses on several classes of promising materials which tend to be semiconductors and have the potential for higher figure of merits. Some examples are given and strategies are discussed for achieving high figure of merits. Among the importance of controlling the carrier concentration, strategies for lowering the lattice thermal conductivity are particularly important for this work and will be discussed in the first chapters. This thesis focusses on compounds which mostly belong to the class of ionic conductors, a group of materials which have been investigated for high temperature thermoelectric energy conversion in recent years. A general introduction of the pertinent materials will be followed by the main chapters about synthesis, chemical characterization and the characterization of the transport properties of the investigated compounds.

1.1 A turnaround in energy policy

Solving the global energy problems is regarded as one of the major challenges in the 21st century.[2] Of particular significance for the future is the end of humanities reliance on fossil fuels like oil, coal and natural gas. While the demand for energy is rising, global warming, the limited supply of fossil resources and the dangers of the use of nuclear energy make the development of renewable, decarbonized energy technologies more and more necessary. Electricity, heat and mobility are the main industries that have to be considered in that regard. The transition from conventional power generation to greater use of renewables is fully underway in many countries and new technologies are rapidly being developed. Besides the realization of a sustainable energy supply, energy efficiency and energy saving will play important roles in the future. The quantitative and qualitative losses, which occur in energy conversion, transport and storage will have to be significantly reduced. This goes hand in hand with the necessity of a better cross-linking of the different energy sectors, particularly the electrification of heat- and transport-sector.

Based on Seebeck and Peltier effect, thermoelectric materials offer a sustainable way of using current energy technologies more efficiently in many processes. By directly converting heat to electric energy, particular the perspective for effective waste heat recovery remains highly promising.[3,4,5,6] Still, due to the low efficiency, thermoelectric devices are not commonly used these days. Possible applications only appear if small size, low weight or non-moving-parts are required. Thermoelectric materials allow very precise temperature regulation because both heating and cooling is performed by the same module just depending on the direction of the current. Although there is an increasing trend towards this market, the development of new materials for devices with a higher efficiency could intensify this trend significantly.

1.2 The Seebeck and Peltier effect

The Thermoelectric effect describes a direct conversion of thermal and electrical energy as a result of a non-equilibrium situation. A temperature gradient leads to a charge carrier movement to reestablish equilibrium. Figure 1 shows bars of p- and n-type semiconductors, which is heated at one side. Assuming electrons to be the only charge carriers and a temperature independent Fermi level, the temperature difference leads to a soft Fermi distribution on the hot end and a sharp Fermi distribution at the cold end.

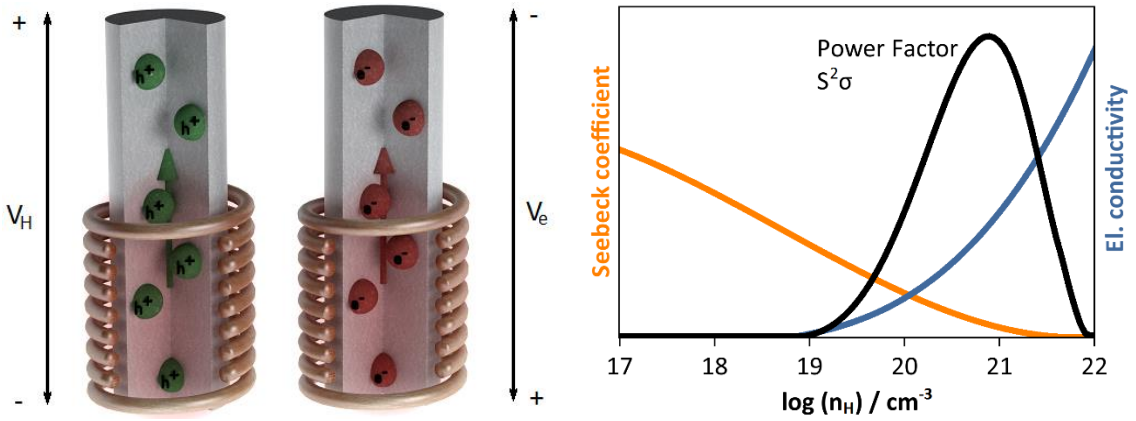

Figure 1. Thermoelectric effect and power factor. A temperature gradient applied to a p- or n-type semiconductor leads to the migration of charge carriers from the hot end to the cold end in analogy to gas molecules which diffuse faster with higher kinetic energy. As a result a small thermovoltage of few microvolts per Kelvin temperature difference builds up. The left images shows the evolution of the Seebeck coefficient and the electrical conductivity as a function of the carrier concentration. Raising the electrical conductivity by increasing the charge carrier concentration leads to a decreasing Seebeck coefficient and vice versa. Therefore, high thermoelectric power factors can be achieved by controlling the charge carrier concentration to an optimum value. Typically this optimal charge carrier concentration is around 10^{19} to 10^{21} carriers per cm^{-3}.

Therefore the electron concentration above the Fermi level is higher at the hot side of the metal bar. The gradient results in a diffusion current until concentration and temperature are equalized. However, if the temperature difference is kept constant, a thermovoltage builds up until it compensates the potential difference due to the diffusion of electrons. The Seebeck coefficient S is defined as the proportionality constant between the measured voltage V and the temperature difference ΔT (for small ΔT).

$$S = V/\Delta T \tag{1.1}$$

Therefore, the thermoelectric effect is the fundamental response to a temperature gradient.[7,8,9] Negative values of the Seebeck coefficient indicate that conduction is dominated by electrons, positive values indicate that the conduction is dominated by holes. In metals, both electrons and holes build up a thermovoltage with opposite signs cancelling each other out. Therefore p- or n-type semiconductors with a band gap are needed for efficient thermoelectric devices where this effect is less pronounced. Here, large Seebeck coefficients of several microvolts per Kelvin temperature difference are possible.

1.3 Requirements for thermoelectric materials

Since the thermoelectric effect is the response of an electric conducting material to a temperature gradient, both electronic and thermal transport properties have to be regarded. The dissipated power P in a circuit is given by:

$$P = V^2/R \tag{1.2}$$

where R is the total resistance and V is the potential.[10] Therefore small electrical resistivity ρ and a large thermopower S are needed for a good thermoelectric material. Furthermore the efficiency of a thermoelectric material is related to the flow of thermal energy through the device. The heat flux in direction x is given by Fourier's law:

$$q_x = -\kappa \frac{dT}{dx} \tag{1.3}$$

where κ is the thermal conductivity.[10,11] For a given thermal flux, a small thermal conductivity will lead to a large temperature gradient ΔT. In consequence, a large thermovoltage can be obtained. An optimal thermoelectric efficiency can be achieved for a material with a high electric and a low thermal conductivity in combination with a high Seebeck coefficient. These properties depend strongly on the materials electronic and phononic transport properties.[12] Regarding the electronic properties of a classic semiconductor (Figure 1) it is obvious that these strongly depend on the doping level with an optimum at around 10^{19} cm^{-3}. If the doping level is significantly higher one ends up with a metal, where the Seebeck coefficient is too small due to minority carrier contributions. At the same time a low doping level leads to a small electric conductivity. To optimize the so called power factor ($S^2\sigma$), a reasonable compromise for the Seebeck coefficient and the electric conductivity has to be found. In good approximation the thermal conductivity corresponds to the sum of electronic and lattice contributions κ_{el} and κ_{lat}, respectively. In many cases κ_{el} can be estimated by the Wiedemann-Franz relation:

$$\kappa_{el} = L\sigma T \tag{1.4}$$

where L is the Lorenz number with a numerical value of $2.45 \cdot 10^8$ WΩ/K^2 for metals.[13, 14] Therefore, a large value of κ_{el} corresponds directly to large σ due to the conduction of heat by charge carriers and cannot be lowered without a negative influence on the electronic conductivity. As κ_{lat} is not related to the electronic conductivity lowering κ_{lat} increases the efficiency of a thermoelectric material directly. As a consequence the main

focus of research on developing new materials for thermoelectric applications focusses on strategies for lowering the lattice thermal conductivity. These qualitative considerations are summed up in the “phonon-glass electron-crystal” concept: a good thermoelectric material requires electronic properties of a crystalline solid with a balanced charge carrier concentration in combination with a low lattice thermal conductivity which is typical for glasses.[4,15,16]

Chapter 2

Electronic transport properties

This chapter will give an introduction of the electronic properties in solids, which are relevant for describing thermoelectric transport. These properties, for example the ability of a material to transport electrical current, is a result of a non-equilibrium situation. Transport theory can be used to describe the deviation of the system from an equilibrium with the help of a distribution function. Without external influences, equilibrium is reached through relaxation after some time. Relaxation times can thereby be influenced by electron-electron and electron-phonon scattering, disorder due to impurities and lattice defects and external influences like magnetic fields.

The electronic transport models used in this thesis later on are based on solutions of the Boltzmann transport equation (BTE), which is an efficient way to deal with dissipation and momentum relaxation of non-stationary electronic states. Still several assumptions are inherently incorporated which result in a limited range of validity. By the introduction of the distribution function, the original many-electron problem is replaced by a one-electron problem with an appropriate potential. Here the equilibrium Fermi-Dirac distribution function is utilized as an approximation for the non-equilibrium distribution function.

Further the BTE is a semi-classical equation and thus not compatible with a quantum mechanical approach, since the carriers are described by Newton's classic equation set of motion. Within BTE, energies of the carriers can be described by an isotropic, parabolic dispersion relationship, a parabolic band. In consequence, the expressions for the relevant transport properties can also be described within parabolic band models. The last major assumption in BTE is that the relaxation of the electron distribution function back to equilibrium can be described by a characteristic relaxation time.

2.1 The Boltzmann equation

Electrons in a periodic crystal are distributed over the states in the energy bands defined by $\vec{r}$ and the wave vector $\vec{k}$. According to the BTE in the steady state there is no net change in the distribution function $f(\vec{r}, \vec{k},t)$ determining the probability of finding an electron at position $\vec{r}$, with crystal momentum $\vec{k}$ at a certain time.[17,18] Here, the sum over the changes in $f(\vec{r}, \vec{k},t)$ due to diffusion, external fields and collisions equals zero.

$$\left.\frac{\partial f(\vec{r},\vec{k},t)}{\partial t}\right|_{diffusion} + \left.\frac{\partial f(\vec{r},\vec{k},t)}{\partial t}\right|_{fields} + \left.\frac{\partial f(\vec{r},\vec{k},t)}{\partial t}\right|_{collision} = 0 \qquad 2.1$$

2.2 The Drude model of electron conduction

The Drude Model is an application of the kinetic theory of gasses, treating electronic transport properties in solid state materials classically as an electron gas.[10] Only electrons close to the electrochemical potential (within few k_BT) contribute significantly to the electric transport. Using the ideal gas theory the electrical and thermal conductivities of materials can be predicted. Assuming a certain concentration of charge carriers n with the charge e, the effective mass m^* and scattering relaxation time τ moving into the direction of an applied electric field E with a drift velocity:

$$v_d = \frac{e\tau E}{m^*} \qquad 2.2$$

leads to the following expression of the electrical conductivity.[10]

$$\sigma = \frac{ne^2\tau}{m^*} = en\mu \qquad 2.3$$

2.3 Band theory

Band theory is also based on a picture of delocalized electrons moving free in the potential of the lattice describing the dynamics of electrons in a material. Instead of having discrete energies as in the case of the electrons in free atoms, the available energy states form bands.

Generally, the full band structure of semiconductors incorporates an anisotropic dispersion relation $E(\vec{k})$ which can only by approximated by numerical methods. However, in order to describe the transport in the semiconductor, the band structure can be expressed in a simplified way. Here, the motion of electrons is described by quantum mechanical wave functions, the "Bloch functions". The energy of a band is a function of the electrons wave vector $\vec{k}$ which is related to the electrons momentum p via $\vec{k} = \hbar p$. Superposition of Bloch functions, leads to the band structure, which is very useful to understand the electronic transport in a given material.[19]

Crucial to the conduction process is whether motion of electrons from occupied to unoccupied states is possible, which is given for a partially filled band. If there is a small band gap in between an occupied valence band and an unoccupied conduction band, it takes a certain amount of energy to excite the electrons from the valence to conduction band leading to semiconducting behavior. The energy of an electron in the conduction band described by a parabolic dispersion is given by:

$$E(\vec{k}) = V_O + \frac{\hbar^2}{2m^*}\vec{k}^2 \qquad 2.4$$

where V_0 is the minimal energy of an electron in the corresponding band.[19] The related density of states $N(E)$ for $V_0 = 0$ is given by:

$$N(E) = \frac{1}{2\pi^2}\left(\frac{2m^*}{\hbar^2}\right)^{3/2}\sqrt{E} \qquad 2.5$$

which possesses a characteristic square root energy dependence.[20] However, the validity of the parabolic band model is restricted to low carrier energies. In many cases the carriers in thermoelectric devices are not driven far from equilibrium and thus the band structure can be described by the parabolic approximation. However, this assumption does not hold for some materials with small band gaps.[21] Here the non-parabolicity of the band structure has to be taken into account.[22,23]

2.4 Fermi Dirac distribution function

Within BTE, the electron equilibrium distribution is described by the Fermi-Dirac distribution function:

$$f_{FD} = (1 + exp[\epsilon - \eta])^{-1} \quad 2.6$$

with the reduced (dimensionless) energy ϵ and the reduced electrochemical potential η which represents the Fermi-energy at zero Kelvin.[17,24] This function applies to fermions considering the Pauli-Exclusion-Principle and indistinguishability of electrons. At absolute zero fermions will fill up all available energy states below the Fermi energy $\epsilon_{F.}$ At higher temperatures some fermions are elevated to levels above the Fermi level. Here, the electrochemical potential is the energy at which *f = 1/2* for all temperatures. The 1 in the denominator can be neglected, if the second term dominates which is given for non-degenerate semiconductors, where the difference between the carrier's energy and η is large. Here, the Maxwell-Boltzmann distribution can be applied:

$$f_{MB} = exp[\eta - \epsilon] \quad 2.7$$

which neglects the Pauli principle and can therefore not be applied for degenerate semiconductors.[25]

2.5 Single Parabolic Band (SPB) model

In many cases the electronic transport in a materials can be displayed by considering only one isolated band with parabolic dispersion, for example the lowest energies of the conduction band in many semiconductors. According to the Drude model, the electrons can be considered as free electrons. However, in order to account for the interaction of the electrons with the lattice, the electrons need to have a different mass. In the case of a single parabolic band one can write down simple expressions for the effective masses.[10]

$$\frac{1}{m^*} = \frac{1}{\hbar^2}\left(\frac{\partial^2 E(\vec{k})}{\partial \vec{k}^2}\right) \quad 2.8$$

The effective mass of an electron increases with decreasing band curvature which is given by the second derivative of energy with respect to electron wave vector $\vec{k}$. As the dispersion of the band decreases with the curvature for a given number of states, the in-

teraction between electrons and the lattice increases. Upcoming polarization effects influence the mobility of the electrons and other charge carriers as well in a way that they seem to have a higher mass.[26,27,28] In summary the "single parabolic band" or "effective mass" model represents a simple model to derive semi-quantitative understandings of the electronic transport properties for many semiconductors,[22,29] and has been applied as an effective tool in this thesis.

2.6 Relaxation time and carrier scattering

The single parabolic band model allows describing the mobility of the charge carriers μ by an effective mass m^* which is related to the curvature of the dispersion curve. Additionally the time between scattering events τ also has an influence on the mobility of the charge carriers.[10,30]

$$\mu = \frac{\tau e}{m^*} \tag{2.9}$$

Within the BTE the interaction of the carriers with the lattice, the influence of ionized impurities, as well as additional scattering caused by inhomogeneity and alloying is described by a collision term in the Boltzmann equation which represents the changes in f due to electron scattering into another phase. In order to obtain an expression for the collision term that can be handled analytically, the relaxation time approximation is commonly used. Here, an external force, such as that induced by electric or magnetic fields, shifts the equilibrium distribution function f_0 by a small amount $f - f_0$. If the scattering events are elastic which means that no energy is lost due to the particular collision, the last term in the BTE can be written as:

$$\left(\frac{\partial f}{\partial t}\right)_{collision} = \frac{f - f_0}{\tau} \tag{2.10}$$

where τ is the energy dependent relaxation time.[31] Within this formulation, the distribution function relaxes to its equilibrium state with the time constant after removing all driving forces. There are various scattering mechanisms such as scattering on defects, impurities, electrons, holes and the lattice which can be described independently.[32] The relaxation time of each particular scattering mechanism depends on the dimensionless charge carrier energy ϵ and λ, which describes the energy dependence of the carrier relaxation time.

$$\tau_i = \tau_{0,i}\, \epsilon^{\lambda-1/2} \qquad 2.11$$

Each scattering mechanism has a characteristic expression for τ_0 and value of λ.[33] When one scattering mechanism does not dominate the other scattering processes in the material, multiple scattering rates must be taken into account. Each scattering rate is equal to $1/\tau_i$, where τ_i is the relaxation time for a particular scattering mechanism. The scattering rates are treated like resistors in series, so the total scattering rate $1/\tau$ is equal to the sum of the individual scattering rates $1/\tau_i$.

$$\frac{1}{\tau} = \sum_{i=1}^{i} \frac{1}{\tau_i} \qquad 2.12$$

Acoustic phonon scattering

Beginning at around 5 K, acoustic phonons scattering becomes the main mechanism limiting the charge carrier mobility at moderate temperatures for many materials as acoustic phonons cause local perturbations in the lattice spacing and thus the bandgap. Scattering between an electron and an acoustic phonon is quasi-elastic leading to relaxation of electron momentum. The presence of these lattice vibrations is taken into account by subjecting electrons to an alternating potential, the deformation potential Ξ, allowing the problem to be described relatively easily despite the reduction of accuracy.[33] Under the assumption, that the acoustic phonon energy $\hbar\omega_q$ is small ($\hbar\omega_q/k_BT \ll 1$), the relaxation time for acoustic phonon scattering within this theory is given by:

$$\tau_{ac} = \frac{2\pi\hbar^4 v_l^2 d}{(2m)^{3/2}\Xi^2 kT}\epsilon^{-1/2} \qquad 2.13$$

where Ξ is the deformation potential, v_l is the longitudinal speed of sound and d is the density. Here, λ equals zero and τ_{ac} is proportional to $m^{*-3/2}$ and $\epsilon^{-1/2}$, which describes the temperature dependence of deformation potential induced acoustic phonon scattering.[34,35]

Ionized impurity scattering

Semiconductors generally contain a large number of donors, acceptors or other impurities. However, charge carrier scattering as a result of neutral impurities is negligible in comparison to that by charge impurities and therefore only ionized impurities have to be considered in that regard.[33,36] The Coulombic field of these randomly distributed ionized impurities disturbs the potential associated with the ideal lattice and scatter the charge carriers. As scattering of this kind relaxes the momenta of the carriers, a relaxation time can be calculated. The relaxation time associated with this scattering process is given by:

$$\tau_{ion} = \frac{16\sqrt{2m^*}\pi\chi^2(kT)^{3/2}\epsilon^{3/2}}{N_{ion}Z^2e^4g}\epsilon^{-1/2} \qquad 2.14$$

where χ is the permittivity, Z the effective charge, N_{ion} the concentration of the ionized impurity, and g given by:

$$g = ln(1+b) - \frac{b}{1+b} \qquad 2.15$$

with

$$b = \frac{8m^*\epsilon kT}{\hbar^2}\frac{\chi kTF_{1/2}(\eta)}{ne^2F_{-1/2}(\eta)} \qquad 2.16$$

and

$$F_j(\eta) = \int_0^\infty \frac{\epsilon^j}{1+exp(\epsilon-\eta)}d\epsilon \qquad 2.17$$

where F are Fermi integrals.[36]

Alloy scattering

If two kind of atoms occupy the same site in a crystal lattice, it is logical to include an alloy scattering mechanism. The relaxation time for alloy scattering is:

$$\tau_{alloy} = \frac{8\hbar^4}{3\sqrt{2}V_{atom}(1-x)U^2m^{*3/2}(kT)^{1/2}}\epsilon^{-1/2} \qquad 2.18$$

where the average volume per atom V_{atom} is equal to $M/n_{atom}N_Ad$, with the molecular weight M, the number of atoms per formula unit n_{atom} and is Avogadro's constant N_A.

U is the alloy scattering potential, which is similar to the deformation potential Ξ in that it describes the way the scattering mechanism changes the energy states of the charge carriers. x is the fraction of substituted atoms. λ equals zero and τ_{ac} is proportional to $\epsilon^{-1/2}$ and $m^{*-3/2}$ as was the case before for acoustic phonon scattering.[37] Under certain circumstances one scattering mechanism can limit τ by producing much shorter relaxation times. In many cases acoustic phonon scattering is the dominating scattering mechanism for high temperatures and ionized impurity scattering for low temperatures.

2.7 Electronic transport equations

The previously discussed approximations can be used for modeling the thermoelectric transport properties of thermoelectric materials at moderate temperatures. Since most thermoelectric materials are heavily doped semiconductors where the electronic transport properties are determined by charge carriers near the electrochemical potential, the SPB model usually can be applied. The charge carrier density n is constant up to a certain temperature, where intrinsic conduction starts to contribute significantly to total conduction.

Within this temperature range the electrical resistivity increases with temperature due to a decrease of the charge carrier mobility as a result of increasing electron-phonon scattering. The Seebeck coefficient also increases due to the decreasing reduced electrochemical potential η and the broadening of the Fermi distribution function. At high temperatures the Seebeck coefficient approaches a maximum due to minority carrier contributions. Here the SPB model is not valid anymore.

A more detailed treatment of the aspects of modeling electrical transport, which are summarized here, can be found in Rowe's *"Thermoelectrics and its Energy Harvesting"* (Chapter 11 by A.F. May and G.J. Snyder).[24]

Seebeck coefficient

As already discussed in the previous chapters, the Seebeck voltage can be described as the difference in the electrochemical potential of the charge carriers across the temperature gradient. Electrons have negative Seebeck coefficients, holes have positive Seebeck coefficients. In an extrinsically-doped semiconductor, the Seebeck coefficient

increases with increasing temperature *T* and decreasing carrier concentration *n*, if minority carriers are not influencing the transport properties. In this case α can be developed as a function of $\tau(\epsilon)$ and the electrochemical potential within the single parabolic band approximation.

$$S = \frac{k_B}{e}\left(\frac{\int_0^\infty \tau\epsilon^{3/2}(\epsilon-\eta)\frac{\partial f}{\partial \epsilon}d\epsilon}{\int_0^\infty \tau\epsilon^{3/2}\frac{\partial f}{\partial \epsilon}d\epsilon}\right) \qquad 2.19$$

Using the expression for τ from the relaxation time approximation (equation 2.11) equation 2.19 can be integrated by parts leading to:

$$S = \frac{k_B}{e}\left(\frac{(2+\lambda)F_{1+\lambda}(\eta)}{(1+\lambda)F_\lambda(\eta)} - \eta\right) \qquad 2.20$$

which only depends on η.[24,25] As a result all parabolic bands have the same Seebeck coefficient for a given η. However, a larger band mass for a given Temperature and charge carrier concentration results in a larger Seebeck coefficient, due to a lower electrochemical potential. Using experimental Seebeck data, the value of η can be estimated assuming one scattering mechanism is dominating and therefore λ is known.

Carrier concentration and carrier mobility

As illustrated in Figure 1 the charge carrier concentration is crucial in order to optimize thermoelectric properties. Within the SPB approach the amount of charge carriers is obtained by integrating over all occupied states within the band (assuming the minimum band energy is zero).[10]

$$n = \int_0^\infty N(E)\,f(E)dE \qquad 2.21$$

Substituting *N(E)* and *f(E)* with the equations given in previous chapters (2.3, 2.4 and 2.6) leads to the following expressions.[24,25]

$$n = 4\pi\left(\frac{2m^* k_B T}{h^2}\right)\int_0^\infty \frac{\epsilon^{1/2}}{1+exp(\epsilon-\eta)}d\epsilon \qquad 2.22$$

$$n = 4\pi\left(\frac{2m^* k_B T}{h^2}\right)^{\frac{3}{2}} F_{1/2}(\eta) \qquad 2.23$$

Experimentally Hall coefficients can be determined in order to obtain Hall carrier concentrations n_H, which can be used to calculate m^*.[21,24,25] Here η is needed which can be obtained from the Seebeck coefficient at a given Temperature as discussed in the previous section. However, due to scattering effects Hall carrier densities (and also Hall carrier mobilities) are not equal to the chemical carrier density (and mobility), which can be taken into account with a Hall factor $r_H = n/n_H = \mu/\mu_H$ that is given within relaxation time approximation by the following equation.[24,25]

$$r_H = \frac{3}{2} F_{\frac{1}{2}}(\eta) \left(\frac{(1/2 + 2\lambda) F_{2\lambda - 1/2}(\eta)}{(1+\lambda)^2 F_\lambda^2(\eta)} \right) \qquad 2.24$$

If transport data of multiple samples are available it is useful at this point to plot the magnitude of the Seebeck coefficient versus the Hall carrier density n_H at a given temperature (Pisarenko plot), in order to ensure that the chosen effective mass leads to a reasonable fit for all experimental data and the SPB model is valid. The SPB model expression for the Hall mobility which depends on the Hall coefficient R_H and the electrical resistivity σ is given by:

$$\mu_H = R_H \sigma = \frac{e}{m} \left(\frac{\int_0^\infty \tau^2 \epsilon^{3/2} \frac{\partial f}{\partial \epsilon} d\epsilon}{\int_0^\infty \tau \epsilon^{3/2} \frac{\partial f}{\partial \epsilon} d\epsilon} \right) \qquad 2.25$$

which is closely related to the carrier relaxation time τ.[24,25] Here, the temperature dependence of the charge carrier mobility provides information about the dominant carrier scattering mechanism. Again, using the expression for τ from the relaxation time approximation (equation 2.11) equation 2.25 can be written as:

$$\mu_H = \mu_0 \left(\frac{(1/2 + 2\lambda) F_{2\lambda - 1/2}}{(1+\lambda) F_\lambda} \right) \qquad 2.26$$

with $\mu_0 = e\tau_0/m^*$ and the Fermi integrals F_j (equation 2.17) which depend on η and therefore provide the temperature dependence.[24,25] Having determined η with the help of the Seebeck coefficient, μ_0 can be estimated experimental via Hall measurements. The charge carrier mobility is particularly useful, because it provides insight in the dominant scattering mechanism. If ionized impurity scattering is the dominating scattering mechanism, the Hall mobility increases with increasing η and n_H (Figure 2).

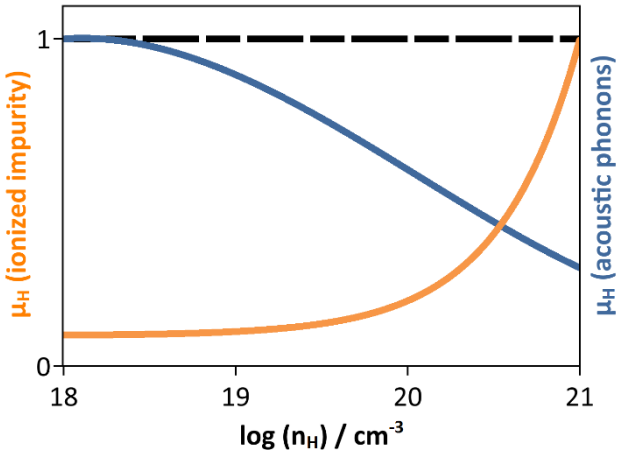

Figure 2. Qualitative dependence of Hall mobility versus Hall carrier density. The three lines represent ionized impurities (orange), neutral impurities (dashed line) and acoustic phonons (blue line) as dominating scattering mechanism.

This can be understood qualitatively by higher energy electrons having higher group velocities and therefore being scattered less likely on localized ionized impurities. In contrast, the Hall mobility decreases with increasing η and n_H for acoustic phonon scattering being the dominating scattering mechanism. In this case, higher energy electrons are scattered more likely by acoustic phonons, because the available states for electrons to be scattered into are higher at higher energies.[25]

Chapter 3

Thermal transport properties

Thermal transport, like electron transport follows from the Boltzmann transport equations. Just as the electrical conductivity characterizes the response of a material to an applied voltage, the thermal conductivity likewise characterizes the response to a temperature gradient. In fact, electrical and thermal conductivity are coupled to a certain extent, since thermal conduction also transports electrons and electrical conduction also transports energy. Exactly this coupling gives rise to thermoelectricity. The first part of the chapter will give an introduction of the thermal conductivity κ of solids.

The thermal conductivity of many crystalline thermoelectric materials behave as expected for doped semiconductors. Here κ decreases with decreasing carrier density due to a decreasing electronic contribution and decreases with increasing temperature due to increased phonon-phonon scattering. However, the thermal conductivity of the crystalline materials investigated in this work often show different temperature dependence which would be expected for amorphous materials. Here, the absolute values are smaller and κ shows almost no temperature dependence. A good example is the thermal conductivity of the Argyrodite Cu_7PSe_6 which increases slightly from about 0.3 $W(Km)^{-1}$ at 300 K to 0.5 $W(Km)^{-1}$ at 575 K.

3.1 Wiedemann-Franz law

The Wiedemann-Franz law describes the relation of the electrical conductivity and the contribution to the thermal conductivity of the associated charge carriers via:

$$\kappa_{el} = LT\sigma \tag{3.1}$$

where L is the Lorentz number, which depends on η and the energy dependence of τ.[10,11,14] This equation is widely used to estimate κ_{el} from the electrical conductivity and calculate the lattice thermal conductivity κ_{lat} via:

$$\kappa_{lat} = \kappa - LT\sigma \tag{3.2}$$

The metallic limit of the Lorentz number is 2.45×10^{-8} WΩK^{-2}.[38] However, significant variations from this degenerate limit are often observed for non-degenerate materials where L converges to 1.5×10^{-8} WΩK^{-2} with an increase in thermopower.[38] In a single parabolic band the Lorenz number can be estimated in analogy to the thermoelectric transport properties in the previous chapter leading to the following expression:[24]

$$L = \frac{k_B^2}{e^2}\frac{(1+\lambda)(3+\lambda)F_{\lambda+2}(\eta) - (2+\lambda)^2 F_{\lambda+1}(\eta)^2}{(1+\lambda)^2 F_\lambda(\eta)^2} \tag{3.3}$$

3.2 Lattice thermal conductivity

Phonons

In an electrically insulating, crystalline material the flow of heat is described through phonons. Phonons are quasiparticles describing collective excitations in the crystalline lattice. They quantum mechanically describe excited states in which the lattice oscillates at a single frequency (analogue to normal modes in classical mechanics). Any arbitrary lattice vibration can be described as a superposition of phonons. For a crystal with at least two atoms in its primitive unit cell, the phonon dispersion relations exhibit two types of phonons, optical and acoustic modes, respectively. The total number of modes is $3N$, where N represents the total number of atoms in the corresponding primitive cell. There are always three acoustic modes, one longitudinal and two transverse acoustic modes. Therefore the number of optical modes is $3N - 3$.[10,11]

Mechanism of heat conduction in crystalline solids

Among others, the mechanism of heat conduction in crystalline substances has been explained by Debye and Peierls.[39,40] Phonons can be described with kinetic theory which relates the thermal conductivity:

$$\kappa_L = \frac{1}{3} C_V v_g \Lambda \qquad 3.4$$

to the specific heat C_V per unit volume, the average phonon group velocity v_g, and the phonon mean free path Λ characterizing the average distance traveled between random scattering events.[41] Finite values of Λ are a result of anharmonic terms in the lattice interactions, even in an ideal crystal. As a consequence, they produce a distribution of phonon frequencies corresponding to thermal equilibrium by coupling together the various lattice vibrations. Since C_V, v_g and Λ depend on this frequency of the lattice vibrations in a continuous manner, equation 3.4 can be written as:

$$\kappa_L = \frac{1}{3}\int_0^{\omega_D} C_V(\omega,T) v_g(\omega,T) \Lambda(\omega,T)\, d\omega = \frac{1}{3}\int_0^{\omega_D} C_V(\omega,T) {v_g}^2(\omega,T) \tau(\omega,T)\, d\omega \qquad 3.5$$

$C_V(\omega,T)\, d\omega$ is the specific heat contributed by phonons within the frequency interval $d\omega$, $\tau(\omega,T)$ is the lifetime of a phonon. In a crystal lattice, there is a minimum wavelength for an oscillation corresponding to a maximum frequency ω_D which is known as the Debye frequency.[10]

Group velocities of acoustic and optical phonons

The frequency dependence of the group velocity is difficult to describe. Only the low frequency acoustic phonons below a certain threshold $\omega_{D,ac}$ can be described by the materials sound velocity v_m which is close to the sound velocity all acoustic phonons. Usually only high frequency acoustic phonons ($\omega \approx \omega_{D,ac}$) show slightly lower sound velocities. Optical phonons with $\omega_D > \omega > \omega_{D,ac}$ generally have a low group velocity. ω_D represents the Debye frequency which is the highest normal mode of vibration for a crystal and has already been introduced as the upper limit in equation 3.5. The related temperature is the Debye temperature Θ_D, which allows the prediction of the heat capacity at any temperature and furthermore provides an indication of the temperature at which the

classical limit of the Dulong-Petit theory is approached.[10,11,17] Therefore the Debye Temperature Θ_D, is a very useful parameter and can be estimated by:

$$\Theta_D = \frac{v_m \hbar}{k_B}\left(\frac{6\pi^2}{V}\right)^{1/3} \qquad 3.6$$

where V is the average volume per atom and v_m is the average speed of sound which can be calculated from the longitudinal and transverse sound velocities (v_l and v_t) via the formula of Anderson for an isotropic material. [42,43]

$$v_m = 3^{1/3}\left(v_l^{-3} + 2v_t^{-3}\right)^{-1/3} \qquad 3.7$$

High Debye Temperatures correspond to a large maximum frequency ω_{max} which implies strong bonds. A good example is diamond with Θ_D = 2230 K.[17] Here, the Dulong-Petit law offers a poor prediction for the specific heat capacity at room temperature. In contrast, lead is an element with weak bonds and a Debye Temperature of 100 K.[17] Therefore Dulong-Petit offers a good prediction for the specific heat at room temperature.

In most cases the heat that is carried by optical phonons is negligible, therefore the heat capacity, group velocity and phonon mean free path in equation 3.4 and 3.5 can be replaced with the corresponding contributions for acoustic phonons $C_{V,ac}$, $v_{g,ac}$ and τ_{ac} leading to the following expression for the lattice thermal conductivity:

$$\kappa_L = \frac{1}{3}\int_0^{\omega_{D,ac}} C_{V,ac}(\omega,T)\,{v_{g,ac}}^2\,\tau_{ac}(\omega,T)\,d\omega \qquad 3.8$$

Volumetric specific heat

The contribution to the volumetric specific heat of the acoustic phonons just has to be scaled by the number of atoms in the corresponding primitive unit cell ($C_{V,ac} = C_V/N$) because only three of the $3N$ degrees of freedom are associated with acoustic phonons. According to the Dulong Petit limit the total heat capacity of a solid C_V is $3k_B$ per atom or $3R_{id}/V_m$, where R_{id} is the ideal gas constant and V_m is the molar Volume. This approximation is usually very accurate for temperatures above the Debye temperature, where all acoustic modes are thermally accessible. Here, the average sound velocity v_m can be uti-

lized to calculate Λ_{ac} for a given lattice thermal conductivity under Dulong Petit approximation. Contrariwise, there are several models to predict phonon scattering relaxation times τ and therefore Λ, allowing a prediction of the lattice thermal conductivity.

Phonon scattering mechanisms

Phonon relaxation times depend on several scattering mechanisms. A combined relaxation time includes contributions of Umklapp scattering (τ_U), mass difference impurity scattering (τ_M), phonon-electron scattering ($\tau_{Ph\text{-}el}$) and boundary scattering (τ_B).[11,44]

$$\frac{1}{\tau} = \frac{1}{\tau_U} + \frac{1}{\tau_M} + \frac{1}{\tau_{Ph-el}} + \frac{1}{\tau_B} \qquad 3.9$$

The different relaxation times depend on frequency and temperature. Since phonon populations are determined by the Bose-Einstein distribution function, phonon occupations and interactions increase linear with temperature at high temperatures.[11] Therefore, at high temperatures the Umklapp scattering contribution dominates τ for many crystalline materials and κ_{lat} shows a with $1/T$ decreasing temperature dependence. Here, κ_{lat} can be estimated with the help of the Klemens formalism:

$$\kappa_L = \frac{\pi}{2\gamma^2}\left(\frac{k}{h}\right)^3 Ma\frac{\Theta_D^3}{T} \qquad 3.10$$

with the lattice parameter a, the molar Mass M and the Grüneisen parameter γ.[45,46] The Grüneisen parameter describes inharmonic effects in a crystal, like the dependency of the phonon frequency from a relative change in volume, which in turn depends on the temperature. The dimensionless parameter is defined as:

$$\gamma = \left(\frac{d\ ln\ \omega_D}{d\ ln\ V_m}\right)_T = \frac{3\alpha_T B_T V_m}{C} \qquad 3.11$$

where α_T is the linear coefficient of thermal expansion and B_T is the isothermal bulk modulus.[46] A second formalism has been proposed by Slack, suggesting that the lattice thermal conductivity decreases with increasing number of atom in the unit cell N.[47] An increasing N results in a larger amount of optical phonons reducing the relative contribution of the acoustic phonons to the lattice thermal conductivity.

3.3 Lattice thermal conductivity of glasslike, anharmonic solids

The thermal conductivity of amorphous materials is quite different from that of crystalline materials. The absolute values of the thermal conductivities of glasses and very similar at a given temperature and considerably lower compared to crystalline substances. In addition, the thermal conductivity of crystalline solids decreases with increasing temperature, whereas the thermal conductivity of glasses increases with increasing temperature. Still the thermal conductivity in glassy solids is provided by thermal phonons as in crystals, therefore equation 3.7 is valid in amorphous materials as well.[41]

As discussed in the previous chapter the numerical value of Λ in a perfect crystal depends on anharmonic interactions, which simply happen more frequently for an increasing density of phonons. Since the phonon density increases with increasing temperature, increasing interactions leads to the commonly observed *1/T* dependence of the thermal conductivity for many crystalline solid materials. However, in the case of glasses, the mean free path is usually limited by geometrical effects due to the lack of long range order. By limiting the mean free path to a constant value Λ_0, which is independent from the phonon frequency and the Temperature, equation 3.4 can be written as:

$$\kappa_L = \frac{1}{3} C_V(\omega, T) v_g \Lambda_0 \qquad 3.12$$

Equation 3.12 explains the increasing lattice thermal conductivity with increasing temperature, because the specific heat increases with temperature. Regarding a periodic, infinite two dimensional lattice the normal modes of vibration are plane waves which propagate indefinitely without loss of energy to other modes of vibration (neglecting anharmonic interactions).

In contrast, in a disordered lattice plane waves are not the normal modes anymore.[41] Here, plane waves will very soon be highly distorted as well, which can be described approximately in terms of a mean free path in the order of the short range ordered building units in the glass. In fact, typical phonon mean free paths for quartz glass at room temperature are in the order of few Å.[11,41] For temperatures significantly below room temperature, where the wavelength of the phonons becomes several times larger than the building units of the glass, scattering becomes less effective resulting in a slightly increasing phonon mean free path.

3.4 Thermal conductivity in liquids

It has to be mentioned that the considerations on a limited phonon mean free path in glasses can be applied in liquids as well, as a glass can be considered as a solidified liquid. In fact, the phonon mean free path in liquids are of molecule dimensions. However, the physics of sound in fluids is much different from that in solids. Because ideal fluids cannot support shear stresses, sound waves in fluids only consist of longitudinal components, whereas sound waves in solids have longitudinal and transverse components (Figure 3).[48,49] As real fluids have a non-zero viscosity they can sustain small amounts of shear stress, leading to a propagation of transverse waves. However, the propagation in most liquids is not very efficient.

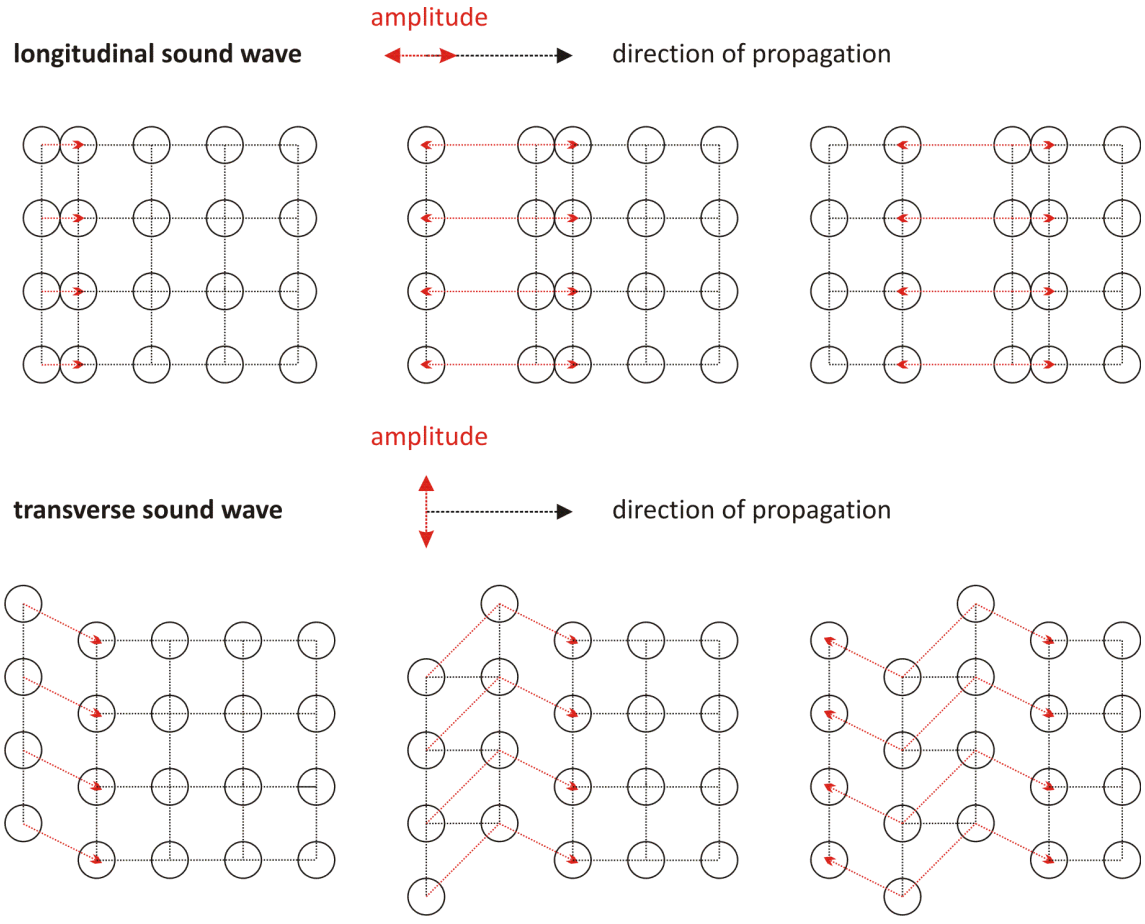

Figure 3. Illustration of longitudinal and transverse wave propagation in a two-dimensional lattice. In a longitudinal wave the particle displacement is parallel to the direction of the wave propagation, whereas in a transverse wave the particle displacement is perpendicular to the direction of wave propagation.

3.5 Minimal phonon conductivity and Cahill formalism

The thermal conductivity of amorphous solids has been qualitatively discussed in chapter 3.3. As atoms in glasses have a short range order, but no translational symmetry, all phonon modes are localized at each atoms. Originally proposed by Slack in 1979,[47] Cahill et al. analyzed the thermal conductivity of various amorphous solids and proposed a theoretical expression for the thermal conductivity of disordered solids.[50]

The model is based on a model by Albert Einstein, who described the thermal conductivity of solids by regarding the interactions between a central atom with the first, second and third neighboring atoms through spring constants using directly the atomic vibrational states. Based on the Debye model of lattice vibrations, Cahill's approach assumes that the thermal energy of each atom is lost during half the period of an oscillation of the atom leading to a phonon mean free path of half the phonon wavelength, which is considered as the lower limit for a phonon. This approach leads to a "glass limit" for the thermal conductivity, which can be written as the sum of three Debye integrals ($x = \Theta_i/T$).

$$\kappa_{min} = \left(\frac{\pi}{6}\right)^{1/3} k_B V^{-2/3} \sum_i v_i \left(\frac{T}{\Theta_i}\right)^2 \int_0^{\Theta_i/T} \frac{x^3 e^x}{(e^x - 1)^2} dx \qquad 3.13$$

Here, the summation over v_i corresponds to the sound velocities of the longitudinal and both transverse modes. Θ_i is given in temperature unit as:

$$\Theta_i = v_i \left(\frac{\hbar}{k_B}\right)\left(\frac{6\pi^2}{V}\right)^{1/3} \qquad 3.14$$

with the average volume per atom V. The high temperature limit for the minimum lattice thermal conductivity is:

$$\kappa_{min} = \frac{1}{2}\left(\frac{\pi}{6}\right)^{1/3} k_B V^{-2/3}(2v_t + v_l) \qquad 3.15$$

which can be used to estimate a lower limit of the thermal conductivity in crystalline solids just by experimentally determining the longitudinal and transverse speed of sound and calculate the average volume per atom for example from crystal structure data.

3.6 Thermal transport modeling

Combining Callaway's model on the effect of point defect scattering at high temperatures with approaches of Alekseeva et al. and Yang et al. a simple model for the reduction of the thermal conductivity due to point defect scattering can be derived.[51,52,53] This model has been successfully applied on Heusler compounds,[53] Skutterudites,[54,55] lead telluride and quaternary copper chalcogenides,[52,56] where one element has been substituted by another element. In this model, point defect scattering is a result of mass difference and strain field fluctuations due to the substituted atoms leading to a change of unit cell size.[57] The ratio between the lattice thermal conductivity of the compound with substitutions κ_{lat}^{mod} and the compound without substitutions κ_{lat}^{pure} is given by:

$$\frac{\kappa_{lat}^{mod}}{\kappa_{lat}^{pure}} = \frac{tan^{-1}(u)}{u} \tag{3.16}$$

with

$$u^2 = \frac{\pi^2 \Theta_D V_{atom}}{h v_m^2} \kappa_{lat}^{pure} \Gamma \tag{3.17}$$

if Umklapp and point defect scattering are dominating phonon scattering. Here, u depends on the Debye temperature Θ_D, the average volume per atom V_{atom}, the average sound velocity v_m and the disorder scaling parameter Γ, which is given by:

$$\Gamma = \chi(1-\chi)\left[\left(\frac{\Delta M}{M}\right)^2 + \epsilon\left(\frac{\Delta a}{a}\right)^2\right] \tag{3.18}$$

The scaling parameter depends on the molar fraction χ, the relative change of the molar mass due to the substitution $\Delta M/M$, the relative change of the lattice parameters $\Delta a/a$ and the fitting parameter ϵ.

Chapter 4

Thermoelectric efficiency

Typically the obtained voltage in a good thermoelectric material is in the range of several microvolts per kelvin. As heat flows from the hot side to the cold side the charge carriers are also driven in the same direction. These are positively charged holes for a p-type semiconductor and negatively charged electrons for a n-type semiconductor. In Chapter 1.3, the requirements for obtaining a good thermoelectric material have already been qualitatively discussed and the “phonon-glass electron-crystal” concept has been introduced.

Regarding the electronic properties, it was pointed out that semiconductors with a certain charge carrier concentration are most suitable for thermoelectric energy conversion, as a compromise for the Seebeck coefficient and the electric conductivity has to be found, which both strongly depend on the doping level. Regarding the thermal transport properties it was pointed out in Chapter 1.3 that a low thermal conductivity is required for an efficient thermoelectric material. Here the electronic contribution to the thermal conductivity cannot be lowered without a negative influence on the electronic conductivity. Therefore, only lowering the lattice thermal conductivity has a direct influence on the thermoelectric efficiency.

4.1 The thermoelectric figure of merit

In order to produce a larger voltage several modules of n- and p-type-semiconductors have to be combined in a way as it is illustrated in Figure 4. Connecting many thermoelectric couples electrically in series and thermally in parallel and sandwiching these between two thin ceramic layers gives a thermoelectric generator, producing a small net voltage proportional to the temperature difference. The conversion efficiency of a thermoelectric device is given by the ratio of power generation and heat transfer:

$$\eta = \frac{\Delta T}{T_h} \cdot \frac{\sqrt{1+ZT}-1}{\sqrt{1+ZT}+T_c/T_h} \qquad 4.1$$

which is limited by corresponding Carnot-efficiency $\eta_c = \Delta T/T_h$.[21,58,59] However the loss of efficiency is described by a factor which describes the complex interplay of counteracting transport phenomena and approaches unity for reaching the Carnot-efficiency limit. However, one typically concentrates on the dimensionless figure of merit:

$$ZT = \frac{S^2\sigma}{\kappa}T \qquad 4.2$$

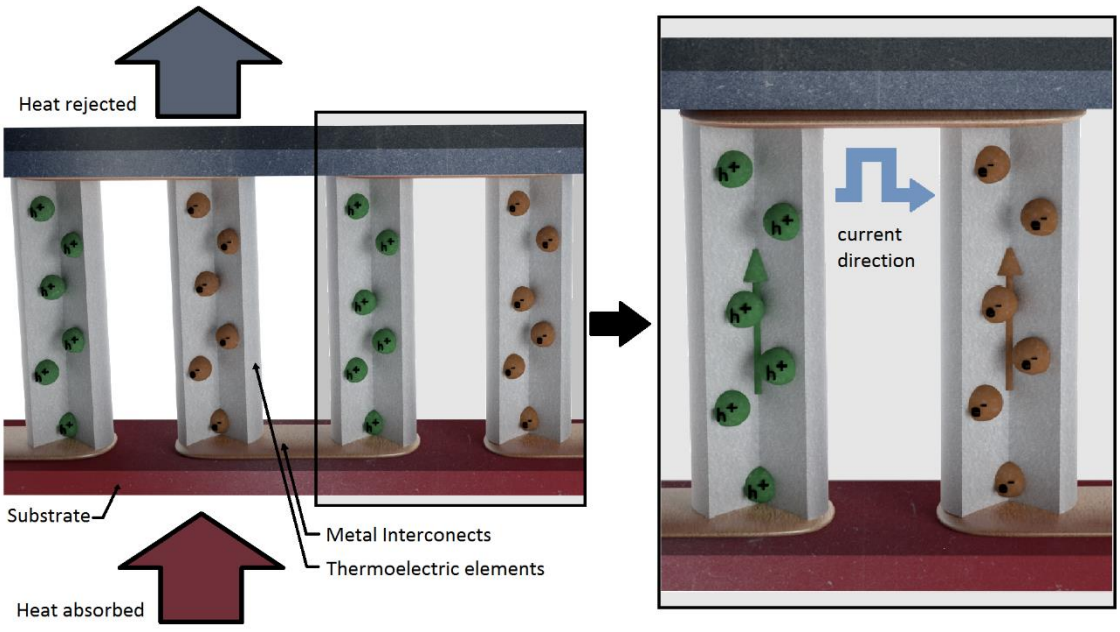

Figure 4. Setup for a thermoelectric generator. Several n- and p-type-semiconductors with electrons and holes as major charge carriers are connected electrically in series and thermally in parallel as illustrated left. The carriers in the semiconductors migrate in the direction of the heat flow building up a thermoelectric voltage. The heat flow from the hot side to the cold site drives the electrical current, determining the power output of the device (right).

with the Seebeck coefficient and the electrical conductivity in the numerator and thermal conductivity in the denominator which corresponds well to the qualitative considerations in the previous chapter.[60] The Carnot efficiency is achieved for *zT* approaching infinity. For a wide technical application *zT* values of 3-4 were necessary, but the *zT* values for commercial available thermoelectric materials vary around 0.8 – 1.5 depending of the desired operating temperature with a device efficiency below 10 %.[61] Usually the figure of merit of the thermoelectric device is even smaller. Some typical *zT* values for some state-of-the-art thermoelectric bulks materials are shown in Figure 5.

However, recent investigations show that drastic improvements of the figure of merit are possible under improved synthesis and consolidation techniques. Here, the peak *zT* of bulk $Bi_{0.5}Sb_{1.5}Te_3$ could be increased from 1.1 near 300 K to 1.86 ± 0.15 at 320 K, due to reduced lattice thermal conductivity as a result of dense dislocation arrays which are formed at low-energy grain boundaries by "liquid-phase compaction". [62,63]

The examples in Figure 5 also reflect the typical temperature dependence of the figure of merit. *ZT* increases with temperature up to a certain point where intrinsic conduction is no longer negligible leading to a drop of the Seebeck coefficient. High *zT* values can be achieved for semiconductors with a balanced charge carrier concentration in order to maximize the power factor $S^2\sigma$. It has been pointed out in the last chapter that the thermal conductivity κ corresponds to the sum of κ_{el} and κ_{lat}, with κ_{el} being proportional to σ. Lowering κ_{el} will therefore lower σ cancelling out any effect. Therefore only κ_{lat} remains as determining factor having a direct influence on *zT*.[5]

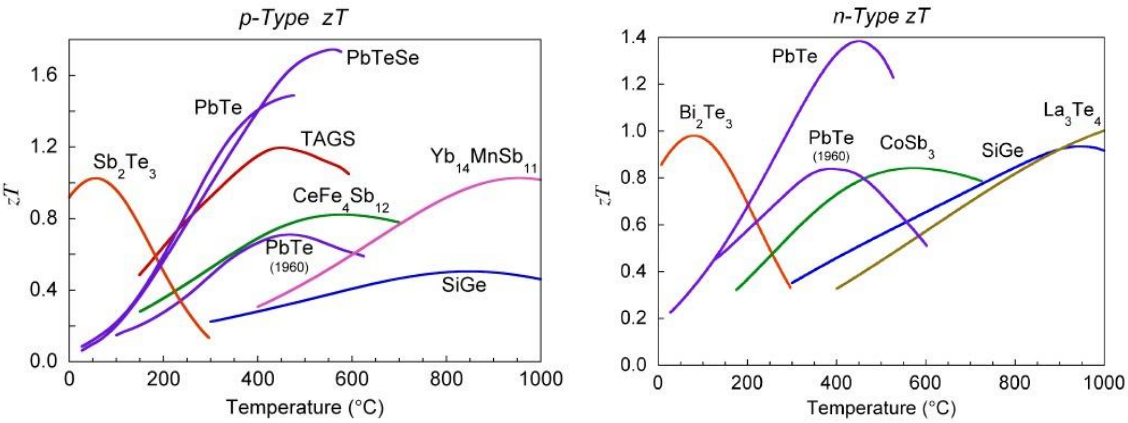

Figure 5. Temperature-dependent *zT* values for popular thermoelectric materials. P-type materials are shown left, n-type are shown right.[64] TAGS stands for $(GeTe)_{1-x}(AgSbTe_2)_x$.

4.2 Enhancement of the thermopower via band structure engineering

In this section, the correlation between the Seebeck coefficient and the electrical conductivity will be discussed in more detail. Qualitatively the Seebeck coefficient decreases with increasing charge carrier concentration *n*, whereas the electrical conductivity increases with *n*. For a degenerate system with high carrier concentrations the Seebeck coefficient is given by:

$$S = \frac{8\pi^2 k_B^2 T m_d^*}{3eh^2} \left(\frac{\pi}{3n}\right)^{2/3} \qquad 4.3$$

where k_B stands for the Boltzmann constant and *h* for the Planck constant and m^*_d for the density of states effective mass.[5] With:

$$\sigma = ne\mu \qquad 4.4$$

for free electrons with the electron charge *e* and the electron mobility μ equation 4.3 shows again that achieving an optimal carrier concentration *n* is crucial for a high figure of merit in a thermoelectric material with a given carrier's effective mass m^*, mobility μ and lattice thermal conductivity κ_{lat}, as *n* is directly related to both Seebeck coefficient and electrical conductivity.

However, equation 4.3 also shows that a high effective mass at the Fermi level m^*_d is beneficial for a large Seebeck coefficient.[65,66,67,68] m^*_d in turn is related to the band curvature via equation 2.4 which makes "band structure engineering" a promising approach for increasing the power factor $S^2\sigma$. Introducing resonant states which represent a flat surface band sharply peaked near the Fermi level via doping is one way which leads to an increased effective mass of the charge carriers and therefore to an increased Seebeck coefficient. This concept has been proposed by *Heremans* et al.[69] and put into practice by doping lead telluride and selenide with thallium, aluminum and chromium leading to an increased Seebeck coefficient.[70,71,72] However, a high carrier effective mass will lead to a low carrier mobility (equation 2.9) and to a low electrical conductivity in consequence (equation 4.4).

Instead of achieving a high DOS at the Fermi level with a resulting high m^*_d via flat bands with a high band effective mass m^*_b, large improvements of the thermoelectric figure of merit could be achieved by increasing the number of band degeneracy N_V. Band

degeneracy describes the number of bands contributing to the electronic transport and therefore linking m^*_d and m^*_b via:

$$m_d^* = N_V^{2/3} m_b^* \qquad 4.5$$

Large band degeneracy can be a result of orbital degeneracy or multiple pockets in the Brillouin zone which is a result of a high symmetry crystal structure.[68,64,73,74] Since new bands cannot be created without changing the crystal symmetry it is necessary to converge bands in order to achieve larger N_V which could be achieved in lead telluride and almost double the zT.[64] Here, doping the material moves the Fermi level, making both a small effective mass valence band at the L-point and a higher effective mass valence band at the Σ point contribute to the transport. At a certain temperature, both bands converge, leading to an increased band degeneracy and increasing the zT to a value of 1.8.

4.3 Reduction of the lattice thermal conductivity

The lattice thermal conductivity describes the heat conductivity due to lattice vibrations. At one part of a solid atoms are vibrating with higher amplitude and transfer that energy to less energetic neighboring atoms. Cooperative motion in form of propagating lattice waves are quantized as phonons. The lattice thermal conductivity can be described in analogy to kinetic gas theory (equation 3.3).[30] Because of the direct influence of the lattice thermal conductivity on the thermoelectric figure of merit materials require low lattice thermal conductivities for high zT. There are many different approaches to achieve a low κ_{lat} in a certain crystal structure. Besides materials with low heat capacities, which are typically found in materials with weak bond strengths, heavy atoms and large unit cell volumes, research often focusses on lowering the phonon mean free path.[30] The easiest way is to introduce lattice defects as sources for phonon scattering. Yet, charge carriers are scattered as well on the defects, thus canceling out the positive effect on the thermoelectric performance.[75] Still, very good results could be achieved for example in Heusler compounds, SiGe or lead Telluride via alloying with other elements to create point defects scattering mostrly high frequency phonons.[51,76,77,78] Low lattice thermal conductivities can be found in Skutterudite-type $CoSb_3$-derivates. [79,80,81] Here, heavy atoms in the vacancies of a cubic crystal lattice act as centers for phonon scattering reducing the thermal conductivity. Another promising approach to reduce κ_{lat} is to use interphases or nanostructured materials.[82,83,84,85,86] Already in the early nineties Dresselhaus et al. showed in

theoretical approaches, that low dimensional semiconductors like bismuth nanowires with a diameter less than 15 nm can have significantly higher zT values up to 3.[87,88]

4.4 Quality factor

In summary, the thermopower of a material can be increased by increasing the density of states of a material at the Fermi level, either by resonant impurities or multiple bands via band engineering. For a given carrier concentration, the thermoelectric figure of merit therefore depends on the charge carrier mobility μ, the number of band degeneracy N_V with the band effective mass m^*_b and the lattice thermal conductivity, which is combined in the quality factor B.

$$B = \frac{\mu N_V m_b^{*\,3/2}}{\kappa_{lat}} \qquad 4.6$$

Chapter 5

Summary of research and motivation

The "phonon-glass electron-crystal" concept has been introduced in the previous chapters as a fundamental approach in the search for new and more advanced thermoelectric materials. According to this concept, potentially good thermoelectric materials require an optimized charge carrier concentration and a low lattice thermal conductivity.[15] In recent years new classes of thermoelectric materials have been discovered fulfilling this concept in various ways, usually by merging two fractional or structural units responsible for the electronic and thermal properties. In this context special attention was paid to Skutterudites[89,90,91] and chalcopyrite-like structures.[92,93] The latter, for example, are doped ternary chalcogenides consisting of an electrically conducting tetrahedral network in combination with a highly disordered structure. These point defects act as phonon scattering centers, reducing the lattice thermal conductivity.[93]

Here, high *zT* values could be achieved for doped samples, despite the fact that these compounds are wide band gap materials with a low mobility of the charge carriers.[92]

In recent publications the concept of using two structural units, one -responsible for suitable electronic properties and the other for lattice thermal conductivity has been applied to superionic compounds like Cu_2Se, Cu_2S, Ag_2Se and related compounds.[94,95,96,97]

In this context the concept of phonon-liquid electron-crystal (PLEC) thermoelectrics has been introduced as an extension of the phonon-glass electron-crystal concept. These materials are usually built up of a very simple anion network, in which the cations are highly disordered with liquid-like mobility at high temperatures, leading to very low lattice thermal conductivities.[98,99] These binary copper and silver selenide or sulfide compounds have been investigated as potential thermoelectric materials for a much longer time.[100] Particularly for the development of radioisotope thermal generators (RTGs) within the NASA space program in the 1960s, huge efforts were made to investigate the potential of copper selenide as thermoelectric material.[101] Here, a radioactive source ($^{238}PuO_2$) emits radiation absorbed by a layer in contact with a thermoelectric device. The other side of the device is cooled by the low temperature of outer space.

However, it could never be successfully used in thermoelectric generators due to chemical stability issues. Because of the drift of copper ions in the material upon an external electrical field, precipitation of copper takes place at the cathode, leading to drastic changes of the thermoelectric performance.[102] Fe was tested as diffusion barrier which unfortunately led to a reduced efficiency due to reactions with the material.[103] In addition, a weight loss due to the evaporation of selenium as well as chemical reactions between material and device contacts could be observed at higher temperatures and current flow in copper selenide.[101] The evaporation of selenium could be suppressed by adding boron nitride and boron oxide glassy coatings which also led to a decrease of device efficiency.[104] Because of these severe degradation issues the project of developing a copper selenide base RGT was terminated.[103]

These problems have to be solved or evaded before these materials can be used for thermoelectric devices. A possible solution would be the operation of the materials at low temperature where the chemical stability of the compounds can be achieved more easily. However, both copper sulfide and copper selenide show high zT values at high temperatures above 600 K.[98,99]

The main chapters of this thesis focus on two possible solutions. First, we have investigated the potential for copper selenide to achieve high *zT* values at room temperature, if the intrinsically high hole carrier concentration can be reduced and attempted to dope the material to optimize its properties (Chapter 7). Using bromine as a dopant we show that reducing the charge carrier concentration in $Cu_{2-\delta}Se$ is in fact possible. Furthermore we provide profound insight in the complex defect chemistry of bromine doped $Cu_{2-\delta}Se$ via various analytical methods and investigate the consequential influences on the thermoelectric transport properties. Here we show, for the first time, the effect of copper vacancy formation as compensating defects when moving the Fermi level closer to the valence band edge. These compensating defects provide an explanation for the often seen doping inefficiencies in thermoelectrics via defect chemistry and guiding further progress in the development of new thermoelectric materials.

Second, we investigated the thermoelectric properties of several compounds, which is belong to the family of the Argyrodite-type minerals with the general formula $A^{x+}_{12-y/x}B^{y+}Q^{2-}_{6}$ for ternary compounds. Argyrodites are a class of more complex ionic conductors. Argyrodites show high ionic mobility at very low temperatures, some representatives even at room temperature and below. The ionic conductivity results from positional disorder characterized by a coalescence of the different A-cation positions through voids into a molten A-cation sublattice, while the B-cations and the anions remain stationary. Partially ordered and disordered modifications can also be found.[105,106,107] Argyrodite-type compounds have already been investigated in the past with a focus on understanding their ionic conductivity.[108,109,110] Highly disordered modifications of lithium Argyrodites with high ionic conductivities are considered as solid electrolytes for all solid state batteries.[111,112]

Due to a huge variety of compositions, which can even be increased by varying the oxidation states leading to both ternary and quaternary compounds, the Argyrodites provide a huge playground for the investigation of structure-property relationships, making this class of materials a well-suited model system for phonon-liquid electron-crystal thermoelectric materials.[113,114] As a starting point, we investigate the thermoelectric transport properties of the compound Cu_7PSe_6 as a more complex Argyrodite-type substitute for Cu_2Se (Chapter 8). Very high copper ionic conductivities even at low temperatures and an extraordinarily low thermal conductivity arising from a high structural dis-

order make Cu_7PSe_6 an interesting representative of phonon-liquid electron-crystal thermoelectrics. In order to investigate the effects of structural aspects on the thermoelectric transport in PLEC thermoelectrics, the series of solid solutions $(Cu,Ag)_7PSe_6$ is considered (Chapter 9). In this context the influence of the substitution of copper and silver on the thermoelectric properties can be easily investigated, which is much more difficult in binary systems. In addition, the influence of the amount of mobile cations per formula unit on the thermoelectric properties can be investigated. Here, Ag_8SiSe_6 has been investigated, which shows outstanding thermoelectric transport properties at temperatures close to room temperatures, in combination with very high charge carrier mobilities (Chapter 10). The remainder of this thesis focusses on the compound $CuFeTe_2$, which is closely related to the Chalcopyrite family, but has a layered PbO-type structure. In contrast to chalcopyrite-type compounds this layered structure provides additional cation sites leading to compositions with variable cation contents ($Cu_{1+x}Fe_{1+y}Te_2$). As the phase pure bulk synthesis of this compound is difficult, there is hardly any research on the physical properties of these compounds. In this context a method for the phase pure bulk synthesis of this compound has been developed and the thermoelectric properties of series of solid solutions $Cu_{1+x}Fe_{1+y}Te_2$ with different x and y have been investigated.

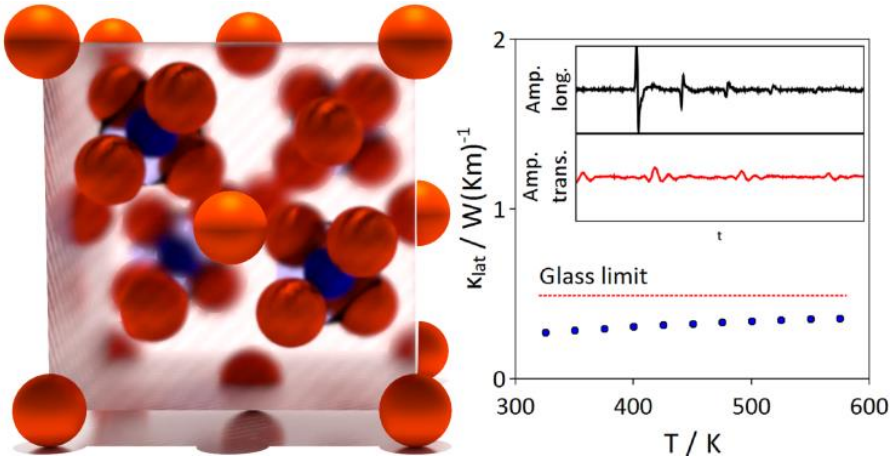

Figure 6. Schematic representation of the crystal structure of Cu_7PSe_6 (left). Selenium is shown in orange and phosphorous in blue. The "molten" cation sublattice is represented by the transparent cube. The right part of the image shows the temperature dependence of the lattice thermal conductivity of Cu_7PSe_6 (blue dots). The glassy limit of the lattice thermal conductivity κ_{min} has been determined by Cahill's formulation and is represented by the red dotted line which lies above the values for κ_{lat}. Ultrasonic measurements of longitudinal and transverse sound velocities are shown in the inset.

5.1 Pertinent materials

Anion doped copper selenide $Cu_{2-x}Se_{1-y}Br_y$

Copper selenide is a p-type semiconductor with a band gap of 1.23 eV, and a wide range of stoichiometric deviation ($Cu_{2-x}Se$).[115] Above 130°C, the compound has an average cubic structure with Se ions forming a face centered cubic lattice and copper ions being distributed over tetrahedral and trigonal sites (Figure 7). This high temperature modification is known to be a superionic conductor owing to the high mobility of the copper ions.[116] The ionic conductivities are as high as those found in molten salts (about $1\Omega m^{-1}$) which is a result of high ionic diffusivities in the order of the value for liquid water at room temperature with a diffusion coefficient is about 10^{-5} cm^2s^{-1}.[117] The room temperature phase shows a very complex superstructure.[118] Several structure models have been proposed within the last decades and controversially discussed. A tetragonal cell with a = 14.06 Å and c = 11.40 Å has been proposed by Borchert in 1945 using x-ray diffraction.[119] Here the lattice constant a is about twice as long as the corresponding lattice parameter in the high temperature phase. Stevels and Jellinek proposed an orthorhombic structure with a = 4.118 Å, b = 20.381 Å and c = 14.06 Å in 1971.[120] This structure was modified by Murray and Heyding, leading to a monoclinic structure with β = 90.38°.[121] Using electron diffraction, two more monoclinic structures have been proposed with a = c = 12.30 Å, b = 40.47 and β = 120°, as well as a = c = 7.14 Å, b = 81.9 and β = 120° in the 1980s.[118,122]

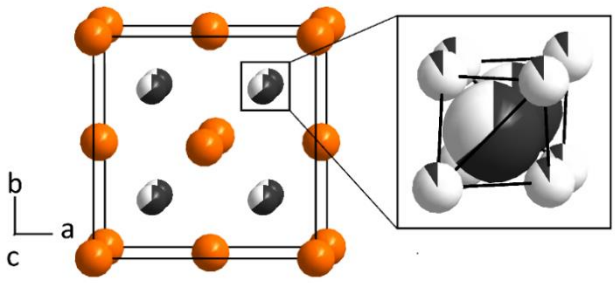

Figure 7. Crystal structure of $Cu_{2-x}Se$ in the fully disordered high temperature β-phase with cubic antifluorite structure. Selenium is shown in orange, the partly filled spheres represent the Cu^+-ions, which are delocalized throughout the structure. The degree of filling represents the site occupancy according to Yamamoto and Kashida.[123] The remainder of the copper ions are located at the 32f interstitial position which are only shown in the enlarged representation on the right. The copper ions can freely travel along the interstitial sites.

Binary copper chalcogenides like Cu_2Se and Cu_2S have been investigated since the 1960s for both photovoltaic and thermoelectric applications. Particularly Cu_xS/CdS Schottky photovoltaic devices developed around 1980, reaching about 9% conversion efficiency attracted much interest in the 1980s.[124,125] In the field of thermoelectrics the first detailed investigations on Cu_2Se and Cu_2S were performed by Ishikawa et al. and El Akkad et al. few years earlier.[126,127]

The thermoelectric performance at high temperatures in Cu_2Se with a zT of about 1.5 at 1000 K is one of the highest zT of any bulk material making it competitive with PbTe, the leading thermoelectric material in hundreds of kelvin temperature range.[74] According to Liu et al. this is attributed to the liquid-like mobility of copper ions within the selenium anion lattice.[98] Due to the lack of long range order, the phonon mean free path is reduced to the minimum wavelength in a glass leading to extremely low lattice thermal conductivities. In addition they also observed a significant reduction of the specific heat below the Dulong petit value of $3Nk_B$ per atom, which is also attributed to the liquid-like behavior of the copper ions. In liquids most transverse vibrational modes do not propagate, reducing the specific heat.

However, the severe electro-migration of copper in this compounds leads to the severe degradation issues already mentioned in the previous chapter. This spurred interest in the properties of copper selenide below the phase transition, where the ionic conductivity would not be of concern. In this work we have investigated the potential for copper selenide to achieve high zT values at room temperature and attempted to dope the material to optimize the thermoelectric properties. SPB calculations on undoped samples indicate, that reducing the charge carrier concentration in this material leads to a significant increase of the thermoelectric figure of merit at room temperature to a competitive value. Since copper selenide is a p-type material, n-type dopants are required.

Here, both cation doping with nickel and zinc as well as anion doping with bromine has been considered as potential route, but only anion doping delivered good results. A series of solid solutions of $Cu_2Se_{1-x}Br_x$ with x = 0.02 to 0.10 has been synthesized (in 0.01 steps) and the thermoelectric transport properties have been characterized.

Copper Argyrodite Cu_7PSe_6

Inspired by the promising thermoelectric properties of copper selenide, here we present the thermoelectric properties of Cu_7PSe_6, representing an Argyrodite-type of analogue of copper selenide. The crystal structure of Cu_7PSe_6 has been investigated in previous publications.[113,128,129,130] As a representative example of the Argyrodite structure type and the structure type variants derived from this, Cu_7PSe_6 can be described as a cubic close-packing of Se^{2-} anions, with additional Se^{2-} and tetrahedral $[PSe_4]^{3-}$ units alternately occupying the tetrahedral voids, which is illustrated in Figure 8.

This anionic framework is stuffed with copper cations, capable of moving along preferential diffusion paths within the $[PSe_6]$-framework at higher temperatures. Cu_7PSe_6 exhibits two structural phase transitions.[107] At temperatures above 320 K, Cu_7PSe_6 crystallizes in a face-centered-cubic structure ($F\bar{4}3m$) with a fully disordered A-cation sublattice. A partial localization of the Cu^+ ions occurs below 320 K, resulting in a cubic primitive structure ($P2_13$), whereby the partial ordering occurs at the highest probability density sites of the high-temperature phase diffusion paths. Below 250 K a second phase transformation occurs where all cations preferably occupy the most stable sites along the diffusion paths resulting in a complete ordering of the copper atoms. [106]

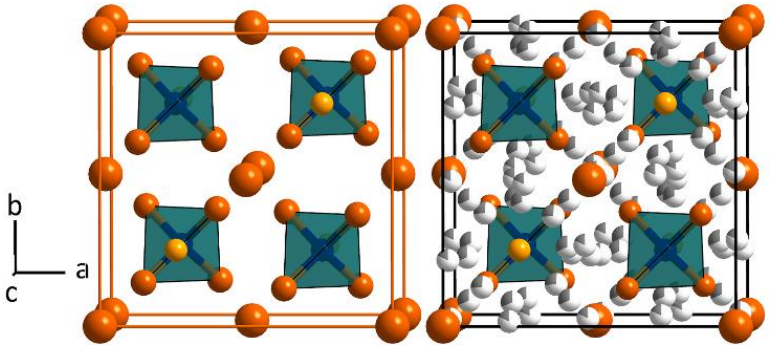

Figure 8. Crystal structure of Cu_7PSe_6 in the fully disordered, face-center-cubic ($F\bar{4}3m$) modification. Selenium is shown in orange and phosphorous in blue. The orange bordered selection is an illustration of the $[PSe_6]^{7-}$ anion sublattice. Se^{2-}-ions form a cubic close packed framework with Se^{2-} and tetrahedral $[PSe_4]^{3-}$ units alternately occupying the tetrahedral voids. Partly filled spheres in the black bordered selection (right) represent the Cu^+ cations, which are delocalized throughout the structure. The degree of filling represents the site occupancy according to Gaudin et al., who also showed images of the joint probability density function (jpdf) illustrating the high disorder of the copper ions.[106]

In this work we describe the synthesis and chemical characterization of Cu_7PSe_6 as well as the characterization of the thermoelectric transport properties, including Seebeck coefficient, electrical resistivity and thermal conductivity. Simultaneous measurements of electrical resistivity and Hall coefficients provided additional information on the electrical transport. Speed of sound measurements were performed in order to estimate the Debye temperature and the minimal lattice contribution to the thermal conductivity.

The obtained data are compared with those of the closely related superionic thermoelectric material Cu_2Se in order to obtain a deeper understanding of the thermoelectric transport in ionic conductors within the phonon-liquid electron-crystal concept.

$(CuAg)_7PSe_6$ series of solid solutions

The further research on Argyrodite-type compounds addresses their structural and thermoelectric properties. Therefore different materials compositions have to be investigated and the effects of structural aspects on the thermoelectric transport have to be discussed. In particular, the influence of the particular species of the mobile A-Cations on the thermoelectric properties can be investigated. For this purpose the compound $(Cu,Ag)_7PSe_6$ is considered.

Both Cu_7PSe_6 and Ag_7PSe_6 have been investigated with respect to their structural properties and their ionic conductivity.[128,129,130,131,132] Cu_7PSe_6 exhibits two structural phase transitions, one from the orthorhombic $Pna2_1$ structure to the simple cubic $P2_13$ lattice at about 250 K and a second at 325 K to the cation disordered face-centered-cubic $F\bar{4}3m$ structure. In comparison, Ag_7PSe_6 undergoes a single phase transition to the $F\bar{4}3m$ structure at about 420-450K.[131,132] Furthermore, the effect of Ag substitution on the electric properties in Cu_7PSe_6 have been investigated by Beeken, Driessen and Wilson.[109] $(Cu,Ag)_7PSe_6$ crystallizes in the $P2_13$ structure at room temperature throughout the whole composition range, and therefore represents an ideal candidate to investigate the influence of mobile cation substitution in PLEC thermoelectric materials.[132]

In this context both the influence of the substitution of copper and silver and the influence of the order-disorder-transitions on the thermoelectric properties can be investigated. Within this work, we describe the synthesis, chemical and thermoelectric characterization of $(Cu_6Ag)PSe_6$, $(Cu_4Ag_3)PSe_6$, $(Cu_4Ag_3)PSe_6$ and Ag_7PSe_6.

Silver Argyrodite Ag_8SiSe_6

Besides a high efficiency several other factors become important for the search for new thermoelectric materials. In this context the mechanical properties, environmental aspects or the limited supply of chemical elements are also highly relevant. In the last years the thermoelectric properties of several promising compounds have been investigated, with high efficiencies at different operating temperatures. Above 800°C Si-Ge-alloys show very good thermoelectric efficiencies.[133,134] Between 500°C and 800°C PbTe and PbSe are studied for more than 50 years still showing the best thermoelectric performances in this temperature regime.[5,135] However, the high toxicity and the mechanical properties of lead chalcogenides preclude wide applications. Therefore research is focusing on Skutterudites and half-Heusler compounds, providing good alternatives with high thermoelectric efficiencies in similar temperature regions.[136] Some compositions even show good thermoelectric performance at temperatures below 200°C.[137]

Still, when the temperature of the heat source is moderate, Bismuth-telluride based materials show superior thermoelectric transport properties. Since the first Peltier cooling devices have been developed over 60 years ago using bismuth telluride, the *zT* of this compound has been steadily improved. The peak *zT* of typical p-type bulk bismuth-telluride could be raised from about 0.5 to 1 using bismuth antimony telluride alloys.[62] Nanostructured alloys even show zT values up to 1.4 at 100°C.[138] However, both electrical and thermal conductivities are anisotropic. For p-type samples the anisotropy of the hole mobility and the lattice conductivity compensate resulting in an almost isotropic *zT*. In contrast the *zT* of n-tpye bismuth telluride is much more anisotropic.[139] Therefore, oriented materials are needed for a figure of merit around 1 which are difficult to produce. In addition the very high costs of the compound itself make bismuth telluride based thermoelectric generators too expensive for commercial use. Finding alternative materials which achieve similar efficiency to bismuth telluride is very challenging, since most materials exhibit high *zT* values only for higher temperatures.

Initially Ag_8SiSe_6 was prepared in order to investigate the influence of the amount of mobile cations per formula unit on the thermoelectric properties by comparing the thermoelectric properties with Ag_7PSe_6. While Ag_7PSe_6 is electrically insulating without any potential for thermoelectric application, Ag_8SiSe_6 shows outstanding thermoelectric transport properties at temperatures close to room temperatures.

In contrast to the other investigated Argyrodites, Ag_8SiSe_6 also shows very high charge carrier mobilities making it potentially competitive with bismuth telluride.

$CuFeTe_2$-type compounds

Chalcopyrite compounds can achieve extremely high thermoelectric efficiencies. For example Kurosaki et al. investigated the thermoelectric properties of ternary chalcopyrites like $AgGaTe_2$, $CuGaTe_2$ (Figure 9), $CuInTe_2$ as well as various solid solution series. $CuInTe_2$ has a zT of 0.6 at 700K and $CuGaTe_2$ has a zT of 1.5 at 1000K.[38,39] Structurally derived from the diamond structure, these so called "adamantine" compounds are characterized by a tetrahedrally bonded network and represent a large family of multinary chalcogenides with many potential ternary and quaternary thermoelectric compounds.

Inspired by the promising thermoelectric properties of these compounds we investigate the thermoelectric properties of $CuFeTe_2$. In contrast to $CuGaTe_2$, $CuFeTe_2$ crystallizes in defect variant of the layered Rickardite structure (Cu_2Sb) which is closely related to the PbO structure type and characterized by a pronounced composition deficiency. The Rickardite structure type provides layers of tetrahedrally bonded ions, interspersed with additional cation sites in between the layers which are pyramidal coordinated.[140] In stoichiometric $CuFeTe_2$ these pyramidal coordinated cation sites are not occupied (Figure 10, left). However, stoichiometric $CuFeTe_2$ does not show single phase behavior.[141] Single crystals, which were grown by directional crystallization from stoichiometric samples by Vaipolin et al.,[142] had the composition $Cu_{1.13}Fe_{1.22}Te_2$ leading to the assumption that stoichiometric $CuFeTe_2$ is not stable and a certain amount of excess metal is needed which occupies the pyramidal coordinated sites. $Cu_{1.13}Fe_{1.22}Te_2$ can be synthesized as a phase pure bulk sample. Neutron diffraction and magnetic measurements do not indicate any signs of ordering on either type of cation site (Figure 10, right).

As the cations can occupy both, tetrahedral and octahedral sites, the structural disorder should have a strong influence on the lattice thermal conductivity. Therefore, two series of solid solutions with different amounts of excess Fe ($Cu_{1.13}Fe_{1.25}Te_2$, $Cu_{1.13}Fe_{1.30}Te_2$, $Cu_{1.13}Fe_{1.35}Te_2$, $Cu_{1.13}Fe_{1.40}Te_2$,) and Cu ($Cu_{1.15}Fe_{1.22}Te_2$, $Cu_{1.20}Fe_{1.22}Te_2$, $Cu_{1.25}Fe_{1.22}Te_2$, $Cu_{1.30}Fe_{1.22}Te_2$,) have been synthesized and the thermoelectric properties have been determined.

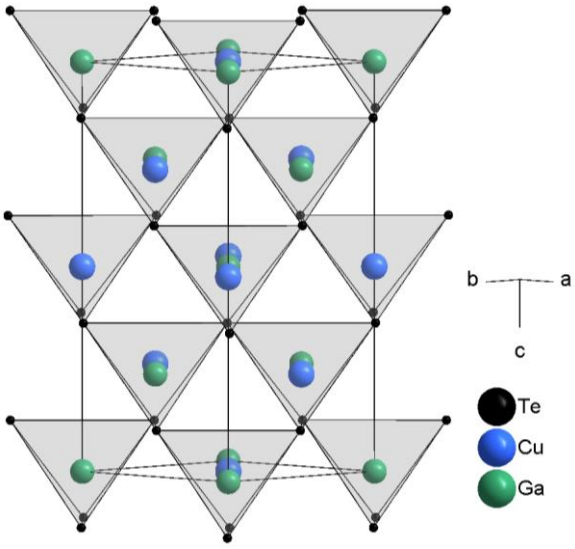

Figure 9. Crystal structure of $CuGaTe_2$ with chalcopyrite structure ($CuFeS_2$). Cu ions are blue, Ga ions are green and Te ions are black with a tetrahedral coordination of the elements indicated. These structures are closely related to the diamond structure, where each ion is coordinated by four nearest neighbors, leading to a tetrahedrally bonded structure.

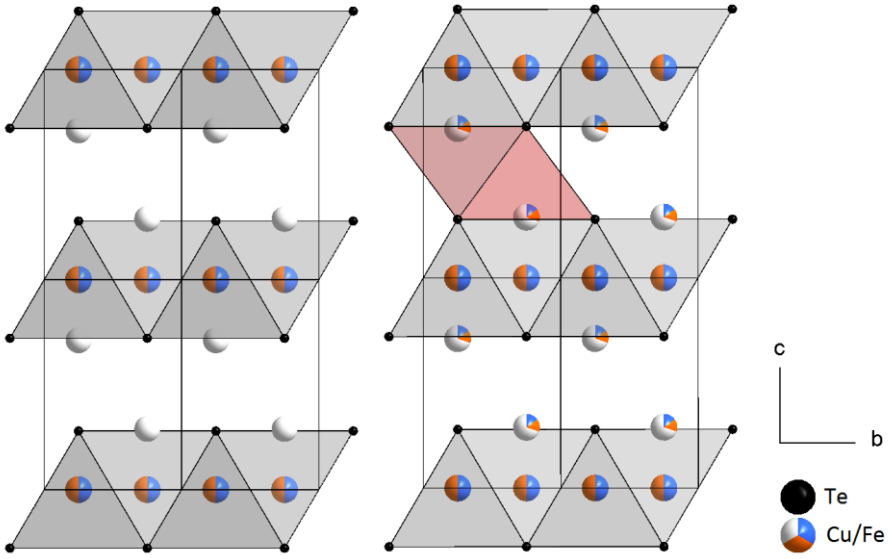

Figure 10. Crystal structure of $CuFeTe_2$ (left), crystallizing in the Rickardite structure type. The cations are tetrahedrally surrounded by Te ions forming layers. In addition to the tetrahedral sites the structure provides pyramidal coordinated cation positions which are not occupied in the case of $CuFeTe_2$ (white). If additional cations are added, these are located at the pyramidal coordinated position. A partial occupation can be found in $Cu_{1.13}Fe_{1.22}Te_2$ (right). Here, a statistically distribution of the cations is assumed, as investigations on magnetic measurements and neutron scattering data show no signs of ordering on either type of site.

Chapter 6

Experimental methods

The first part of this chapter focusses on the synthesis of the materials which have been investigated in the course of this thesis. Detailed information about the used starting materials, synthetic procedures and sample consolidation will be provided for Argyrodite-type samples, doped copper selenides and chalcopyrite related compounds.

The second part focusses on the characterization techniques which were used for the chemical characterization of the synthesized compounds. X-ray powder diffraction was the primary tool to check for phase purity and investigate the crystal structure of the synthesized materials. In the case of $Cu_{2-y}Se_{1-x}Br_x$ a more detailed analysis of the sample stoichiometry was utilized using x-ray photoemission spectroscopy (XPS), x-ray fluorescence (XRF) and inductively coupled plasma mass spectroscopy (ICP-MS).

The final part of the chapter focusses on the characterization of the thermoelectric transport properties, including Seebeck coefficient, Hall coefficients as well as electrical and thermal conductivities. The measurement of the thermal diffusivity was performed under continuous argon flow, the other measurements under dynamic vacuum. All measurements were performed on multiple samples for each composition. Shown measurement data represent both heating and cooling data. The combined uncertainty for all measurements involved in zT determination is ~20 %.

6.1 Synthesis of Argyrodite-type materials

General procedure

Bulk samples of polycrystalline Argyrodite-type compounds were prepared by melting and annealing techniques using elemental powders as starting materials. In order to ensure the absence of metal oxides in the reaction mixture all metal powders were heated for several hours to 525 K under N_2/H_2 (95:5) flow in a tube furnace using a corundum boat as the reaction vessel. Phase purity of all starting materials was verified by x-ray diffraction and all synthetic procedures were carried out in a N_2 dry box. In order to ensure completely dry conditions, the synthesis was performed in evacuated quartz ampoules, which were dried at 1073 K under dynamic vacuum for several hours before usage. All procedures were carried out in horizontal tube furnaces with heating and cooling rates of 5 K/min.

Copper Argyrodite Cu_7PSe_6

For the preparation of polycrystalline bulk samples of Cu_7PSe_6 elemental powders of Cu (Alfa Aesar, 99.999 %) and Se (Alfa Aesar, 99.999 %), as well as P pieces (Alfa Aesar, 99.999 %) were used. The starting elements were thoroughly ground, sealed in quartz ampoules and heated to 1323 K for 3 hours. The obtained chunks were crushed, ground to a fine powder, sealed in quartz ampoules again, and re-annealed at 773 K for at least 72 hours. Here, the ampoule was placed close to the plug of the tube furnace as it is illustrated in Figure 11 in order to have a very small temperature gradient within the ampoule during the annealing process. After an annealing time of 72 hours a very small chunk of a shiny black substance could be observed at the cold end of the ampoule. Since the amount was extremely small and could not be removed from the quartz it was not possible to obtain x-ray powder diffraction data. The second annealing step was necessary to prevent the formation of Cu_2Se in small amounts as byproduct, which can be observed in x-ray powder diffraction data after the first reaction step.

The obtained powders were hand ground and consolidated into 1-1.5 mm thick, 10 mm diameter pellets at 473 K for 24 hours under a force of 50-75 kN by hot pressing in steel dies. The resulting discs are extremely brittle and have more than 95 % theoretical density, determined from the geometric densities.

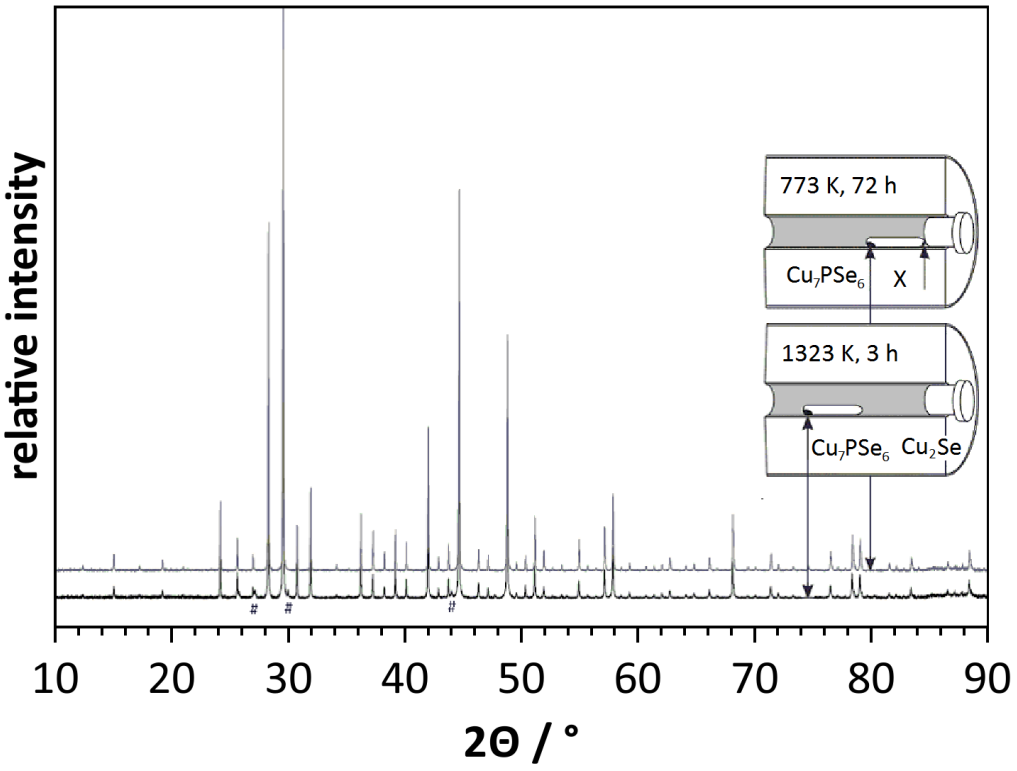

Figure 11. X-ray powder diffraction data of Cu_7PSe_6 after the first reaction step at 1023 K for three hours (black line). Most reflections can be assigned to the simple cubic Cu_7PSe_6 phase. However, some additional reflections with very low intensities can be observed (#), which can be attributed to a Cu_2Se impurity phase. After an additional annealing step of at least 72 hours at 773 K the additional reflections are not observed anymore (grey line).

$(CuAg)_7PSe_6$ series of solid solutions

In addition to Cu_7PSe_6, a series of solid solutions has been prepared, where a certain amount of the copper ions have been replaced with silver ions. Using elemental powders of Cu (Alfa Aesar, 99.999 %) and Se (Alfa Aesar, 99.999 %), as well as P pieces (Alfa Aesar, 99.999 %) $Cu_6Ag_1PSe_6$, $Cu_4Ag_3PSe_6$, $Cu_2Ag_5PSe_6$ and Ag_7PSe_6 have been prepared. The starting elements were thoroughly ground, sealed in quartz ampoules and heated to 1073 K for 12 hours. The obtained chunks were crushed, ground to a fine powder, sealed in quartz ampoules again, and re-annealed at 773 K for 72 hours.

The obtained powders were hand ground and consolidated into 1-1.5 mm thick, 10 mm diameter pellets at 473 K for 24 hours under a force of 50-75 kN by hot pressing in steel dies. The resulting discs are extremely brittle and have more than 95% theoretical density, determined from the geometric densities.

Silver Argyrodite Ag_8SiSe_6

Bulk samples of polycrystalline Ag_8SiSe_6 were prepared by melting and annealing techniques using elemental powders of Ag (Alfa Aesar, 99.999 %) and Se (Alfa Aesar, 99.999 %), as well as Si pieces (Alfa Aesar, 99.9999 %), which were grounded into fine powder before use. For the synthesis of Ag_8SiSe_6 the starting elements were thoroughly ground, sealed in quartz ampoules and heated to 1173 K for 1 hour. The obtained chunks were crushed, ground to a fine powder, sealed in quartz ampoules again, and re-annealed at 773 K for 72 hours.

The obtained powders were hand ground and consolidated into 1-1.5 mm thick, 10 mm diameter pellets at 473 K for 24 hours under a force of 50-75 kN by hot pressing in steel dies. The resulting discs were much less brittle compared to the other Argyrodite samples and have more than 95% theoretical density, determined from the geometric densities.

6.2 Anion doped copper selenide $Cu_{2-x}Se_{1-y}Br_y$

Bulk samples of polycrystalline $Cu_{2-y}Se_{1-x}Br_x$ with x = 0, 0.02, 0.03, 0.04 and 0.05 were prepared by melting and annealing techniques using powders of Cu (Alfa Aesar, 99.999 %) and Se (Alfa Aesar, 99.999 %), as well as CuBr (Sigma, 99.999 %). The synthesis was performed in evacuated quartz ampoules, which were dried at 1073 K under dynamic vacuum for several hours before usage. For the synthesis of $Cu_{2-y}Se_{1-x}Br_x$ the starting elements were thoroughly ground, sealed in quartz ampoules and heated to 1423 K for 1 hour, then cooled down to 1073 K and annealed for 48 hours. All procedures were carried out in box furnaces with heating and cooling rates of 5 K/min. Each mixture of starting materials had the nominal composition of $Cu_2Se_{1-x}Br_x$. However, after the annealing step, a small amount of unreacted elementary copper could be removed from the reaction product, indicating that the synthesized samples are slightly copper deficient (Figure 12).[143,126]

The obtained powders were hand ground and consolidated into 1-1.5 mm thick, 12 mm diameter discs at 873 K for 5 hours under a pressure of 40 MPa by induction hot pressing in high density graphite dies.[144] The resulting pellets have more than 95% theoretical density, determined from the geometric densities.

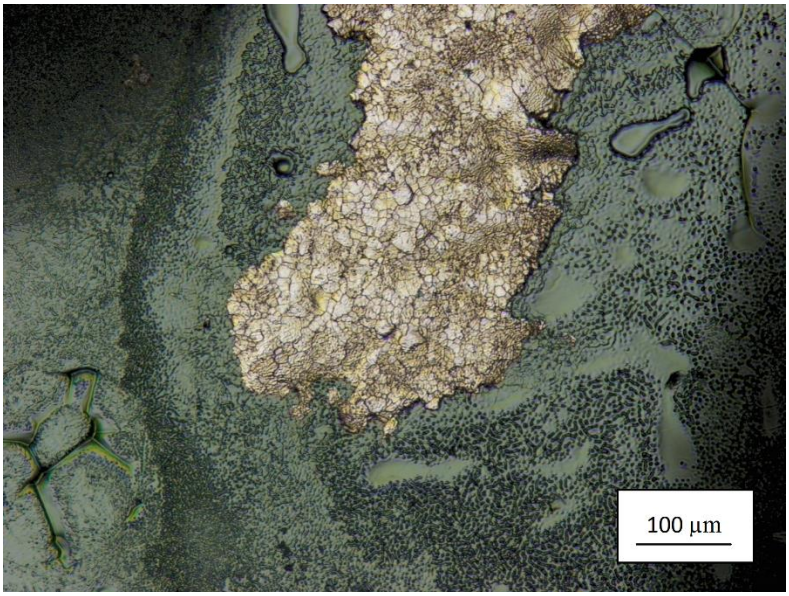

Figure 12. Laser microscope image of the synthesized copper selenide chunks. The image shows excess copper on the surface of the copper selenide after the annealing process. The copper can be easily separated from the chunk using tweezers. Afterwards the surface is removed with sand paper.

6.3 $CuFeTe_2$-type compounds

Bulk samples of polycrystalline $Cu_{1+x}Fe_{1+y}Te_2$ were prepared by melting and annealing techniques using elemental powders of Cu (Alfa Aesar, 99.999 %) Fe (Alfa Aesar, 99.999 %), as well as Te pieces (Alfa Aesar, 99.9999 %), which were grounded into fine powder before use. The synthesis was performed in evacuated quartz ampoules, which were dried at 1073 K under dynamic vacuum for several hours before usage. For the synthesis of $Cu_{1+x}Fe_{1+y}Te_2$ the starting elements were thoroughly ground, sealed in quartz ampoules and heated to 1173 K for 1 hour. After annealing the chunks at 823 K for 7 days they were crushed and ground to a fine powder. A very long annealing time was essential in order to obtain a phase pure reaction product. Huge, flaky and shiny crystals could be observed in the reaction mixture, indicating a preferred crystal orientation.

The obtained powders were hand ground and consolidated into 1-1.5 mm thick, 12 mm diameter discs at 873 K for 5 hours under a pressure of 40 MPa by induction hot pressing in high density graphite dies. The resulting pellets have more than 95% theoretical density, determined from the geometric densities.

6.4 Pressure-Assisted Sintering

Rapid hot-press system

The custom-built hot press system at Caltech has been employed for the consolidation of the powdered $Cu_{2-x}Se_{1-y}Br_y$ and $CuFeTe_2$ samples. The hot press system has been developed to rapidly consolidate thermoelectric materials over a large temperature range (400-2300 K) within an inert atmosphere. The heat in this system is provided by an induction coil operated in the RF range applied directly to a graphite die. Before the powders can be loaded into the graphite die, a grafoil sheet is used to cover the inside of the die. Then a short plunger is inserted into the base of the die which also has to be covered by a circular piece of grafoil. After filling the powder into the dye and compressing by hand, another circular piece of grafoil is put on top of the powder in order to completely separate powder and dye with a grafoil layer. Then the top-plunger is put into the die. By using short plungers as spacers more than one consolidated disc can be obtained in one press run. After placing the die in the induction coil and inserting the thermocouple, the chamber door is closed and a small load of about 5 MPa is applied on the die. After evacuating and flooding the chamber with argon for three times, the desired load is applied to the die slowly with less than 1% of the total load per second under a small argon flow. Afterwards the induction heating power supply is turned on and heating begins.

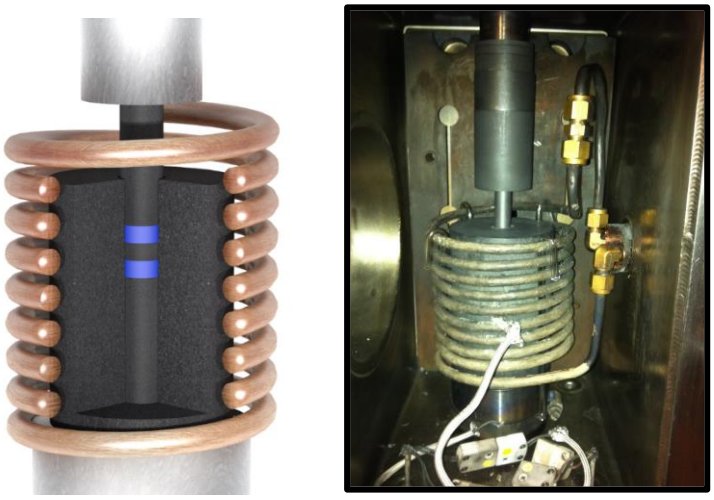

Figure 13. Schematic illustration of an induction hot press setup (left) and picture of the hot press chamber at Caltech (right). The powdered sample is loaded into the die and separated from the die with a thin layer of grafoil on all sides. Pressure is attained with a graphite plunger and the induction coil is utilized to heat up the die.

Weber lab-press system

A Weber manual lab press has been employed for the consolidation of the powdered Argyrodite samples. Here, steel dyes are used for the consolidation of the powdered samples, which allow sample consolidation at a pressure of 200 MPa. The heat in this system is provided by resistive heating and allows hot pressing at temperatures up to 575 K. For the consolidation of Argyrodite type samples, a temperatures of 575 K and a Pressure of 150 MPa were used. Before pressing, the compounds were ground into a fine powder and loaded into the pressing tool. Usually vacuum can be applied to the pressing tool before the consolidation, in order to remove air between the grains. Unfortunately this step leads to cracks when removing the pellet from the pressing tool after consolidation and therefore has to be omitted.

Density determination

Some laser microscopy images of the consolidated pellets after polishing with sand paper are shown in Figure 15. Laser microscope images of cross sections were also used to determine the density of the obtained pellets. After polishing, weighing and quartering one of the pressed pellets, the thickness was determined at ten different points and used to calculate the density of several Argyrodite pellets. For several pressed pellets, densities of 98% ± 1% were determined.

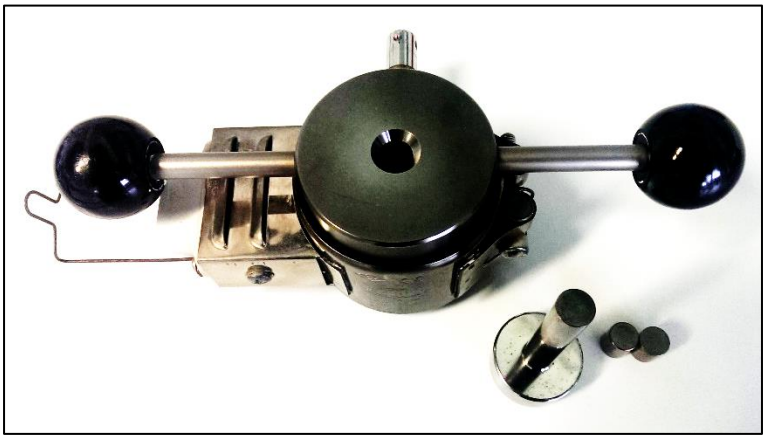

Figure 14. A Weber lab press system was used for the sample consolidation of Argyrodite-type samples. The picture shows the inductively heated pressing tool, allowing sample consolidation at a pressure of around 200 MPa (right).

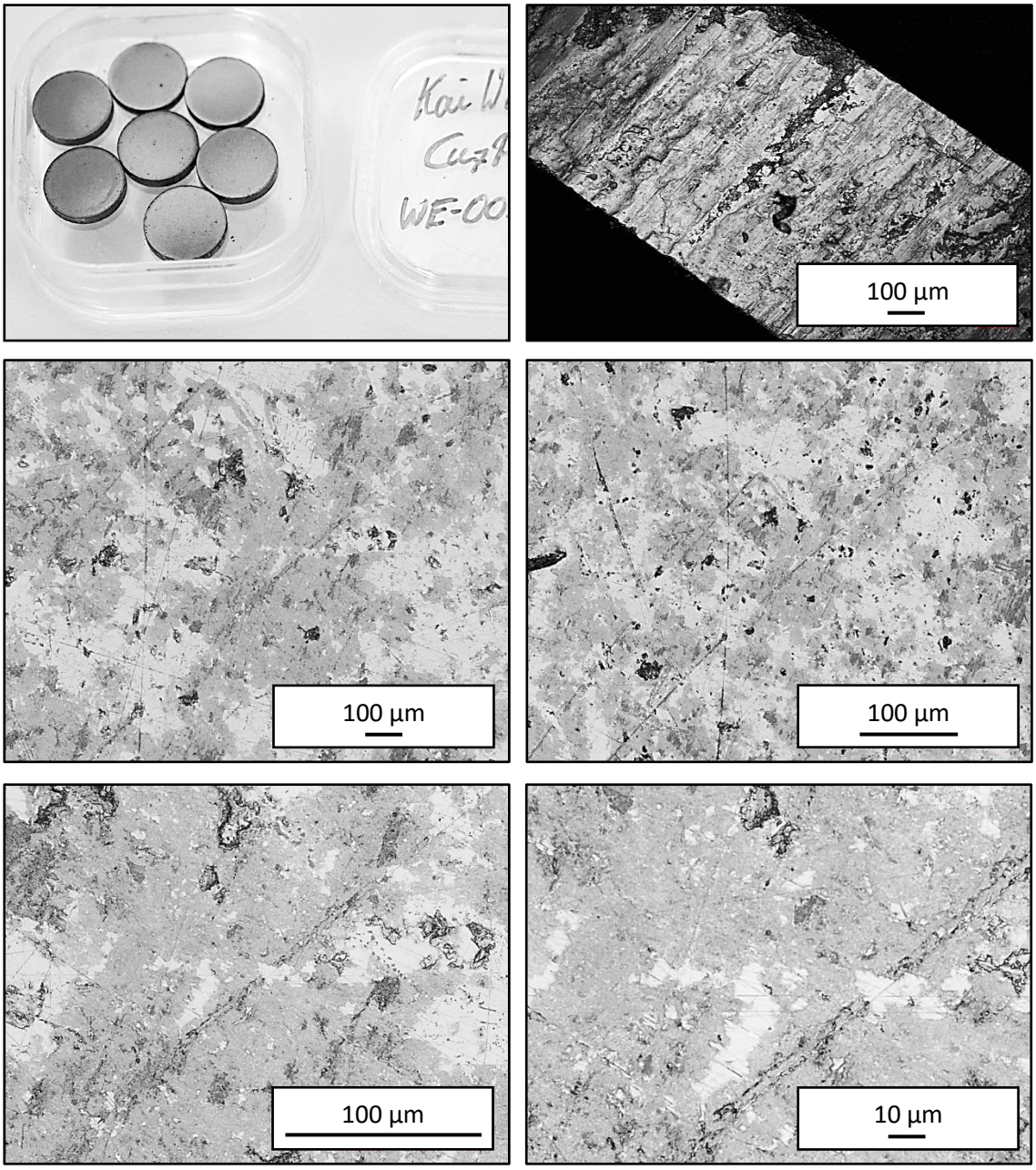

Figure 15. Images of Argyrodite-type samples after consolidation (top left). Several pellets of the compositions $(Cu,Ag)_7PSe_6$, and Ag_8SiSe_6 were pressed and their thermoelectric properties determined. Before measuring the thermoelectric transport properties, the pellets were polished with sand paper. The laser microscope images show the surface of a pellet of Cu_7PSe_6 after polishing. Pictures of different cross sections were also taken in order to determine the thickness of the pellets on several positions, which were used to determine the density of the pressed pellets.

6.5 Chemical Characterization

X-ray powder diffraction

X-ray diffraction experiments were performed on a Siemens D5000 powder diffractometer equipped with a Braun M50 position-sensitive detector, Ge (111) monochromator (Huber 615 002), and Cu K_α radiation, with a step size of 0.0078°.

High temperature x-ray diffraction experiments were performed on a Bruker D8-Advance powder diffractometer equipped with a Vantec detector, Ge (111) monochromator, and Cu K_α radiation, in a 0.5 mm capillary.

Rietveld refinements for Argyrodite type samples and $CuFeTe_2$ were performed with TOPAS Academic V4.1 applying the fundamental parameter approach.[145] Pawley fits for the doped copper selenide samples were performed with TOPAS Academic V5.0 applying the fundamental parameter approach.[146]

X-ray fluorescence (XRF)

X-ray fluorescence (XRF) analysis was used to obtain a precise atomic percent ratio of bromine to selenium in each synthesized $Cu_{2-y}Se_{1-x}Br_x$ sample. The measurements were performed on an 18-kW rotating anode, two-circle diffractometer with monochromated Mo K_α radiation (E = 17.4 keV) operating at 50 kV and 160 mA. Spectra were taken at an incident angle of $\theta = 20°$, resulting in an average penetration depth of 9.3 μm. The horizontal by vertical beam footprint at the sample was 0.6 × 6.3 mm and the total collection time for each sample was 6 minutes.

XRF data were collected with a Vortex-EM 350 μm thick silicon drift detector. The fluorescence yield was corrected for self-absorption and detector efficiency. These ratios were determined by using: 1) the measured Se Kα (11.2 keV) and Br Kα (11.9 keV) net photon counts from the solid-state detector XRF spectra (Figure S4), 2) the cross-sections for these XRF emission lines at the incident energy of 17.4 keV,[147] 3) the calculated transmissions for the incident and emitted x-rays in the sample, 4) the transmissions for the emitted x-rays through the air path between the sample and the detector, and 5) the detector efficiency.

Experimental-XPS.

The photoelectron spectra (XPS) were collected on pressed pellets with a Thermo Scientific ESCALAB 250Xi with monochromatic Al K_α x-ray (1486.74 eV) and energy resolution of 0.42 eV. The surface was sputtered by a 3 keV electron gun for 120 seconds in order to remove the surface oxide layer prior to taking the measurement. The oxygen 1s peaks of both samples were completely removed after sputtering (Figure 16, left). The carbon 1s peak (binding energy 284.5 eV) was used as a reference to calibrate the binding energies of the other core level spectra (Figure 16, right).

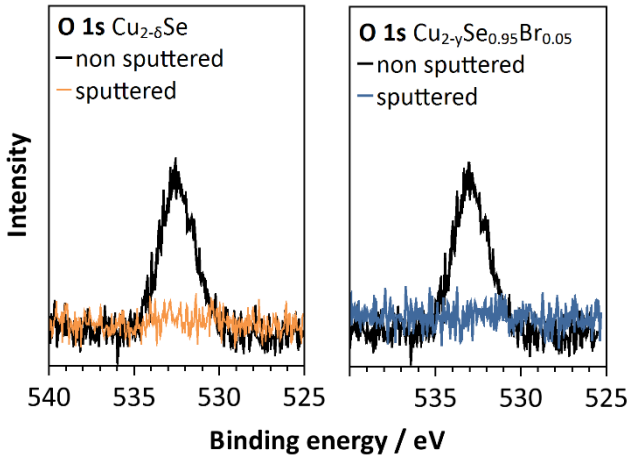

Figure 16. Oxygen 1s peak in the XPS spectra for $Cu_{2-\delta}Se$ and $Cu_{2-y}Se_{0.95}Br_{0.05}$ before and after sputtering for 120 seconds in order to remove native oxides.

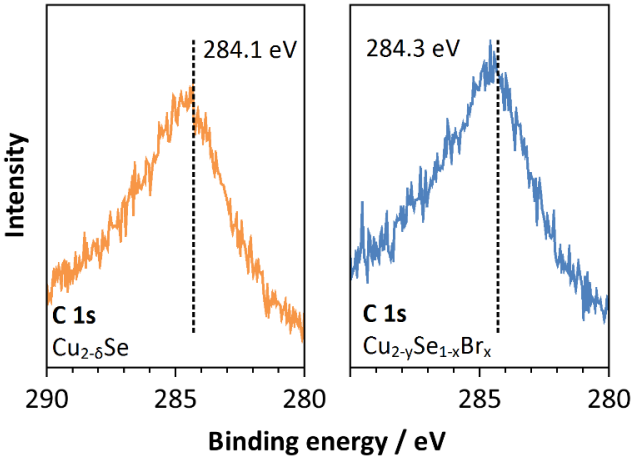

Figure 17. Carbon 1s peak in the XPS spectra (binding energy 284.5 eV) for $Cu_{2-\delta}Se$ and $Cu_{2-y}Se_{0.95}Br_{0.05}$, which was used as a reference to calibrate the binding energies of the other core level spectra.

ICP-MS.

The variation of the Cu/Se ratio was determined with ICP-MS. Data were obtained by dissolving 50 mg of the powdered samples in conc. HNO_3 (Merck, Suprapure). The obtained solutions were diluted to the required concentration of 10-100 ppb Cu and Se. As internal standard 5ppb Rh were added. The measured isotopes were Cu(63), Cu(65), Se(77), Br(79) and Rh(103). Table 1 lists the operating parameters for the ICP mass spectrometer. Typical signal intensities were $1.6\text{-}2.7 \times 10^7$ with $1.0\text{-}2.1 \times 10^5$ blind count rates for Cu(65), $3.0\text{-}6.0 \times 10^5$ with $4.7\text{-}5.4 \times 10^3$ blind count rates for Se(77) and $8.2\text{-}4.3 \times 10^6$ for Rh(103). A significant decrease in absolute sample flow rate during the measurement could be observed. The decrease was quantified by the absolute Rh(103) counts which decreased about 30% during the measurement. This is due to blockage of the capillaries and cannot be avoided. However, the absolute count rate is related to the measured Cu/Se ratio due to mass load effect. Therefore a calibration curve for the Cu/Se ratio vs the absolute Rhodium counts had to be created. This was done for the undoped sample by measuring the Cu/Se ratio at the beginning and at the end of the experiment as well as between the measurements of samples with a different Br content (Figure 17). Each measurement consists of 180 scans with a sample time of 0.002 s per scan for each isotope. Washout time between each measurement was 120 s. Afterwards, the relative difference of the Cu/Se ratio between the doped samples and the calibration curve were determined and used to calculate the relative stoichiometry.

Table 1. Operating parameters for the ELEMENT2 ICP-MS for trace element analysis

Rf power / W	1105
Cool gas flow rate / l min^{-1}	16
Auxilary gas flow rate / l min^{-1}	0.9
Sample gas / l min^{-1}	0.735
Sample time / s	0.002
Samples per peak	100
Mass window / %	10
Scan mode	Escan
Detector mode	Both (Analog + Counting)

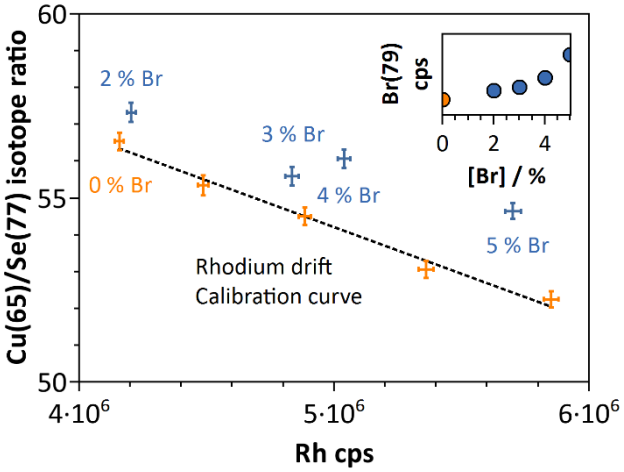

Figure 18. ICP-MS analysis of the bromine doped copper selenide samples. Linear calibration curve of the Cu(65)/Se(77) ratio versus the absolute Rh(103) count rate for the $Cu_{2-\delta}Se$ sample (black dotted line). Orange dots represent measurements of the undoped $Cu_{2-\delta}Se$ sample which were used to obtain the calibration curve, blue dots represent measurements of the doped samples. The inset shows the absolute Br(79) counts for the undoped sample and the doped samples (blue). The absolute bromine count rate increases with the nominal bromine amount in each sample indicating that the absolute amount of bromine increases which is consistent with the XRF data.

Thermogravimetry

Simultaneous thermogravimetry and differential thermal analysis (TG-DTA) have been performed with a Netzsch STA 449 F3 Jupiter device between room temperature and 875 K at 10 K/min, under argon flow.

6.6 Characterization of Transport Properties

Seebeck coefficient.

The Seebeck coefficient is the essential property for evaluating the potential performance of thermoelectric materials. It can be determined by measuring the voltage and the temperature gradient between two points of a sample at the same time. Here, a good electrical and thermal contact between sample and measuring probes is highly important which can be achieved by a setup illustrated in Figure 19. A plane parallel pellet is covered on both sides with a thin layer of grafoil and placed in between two cylindrical resistance heating blocks.

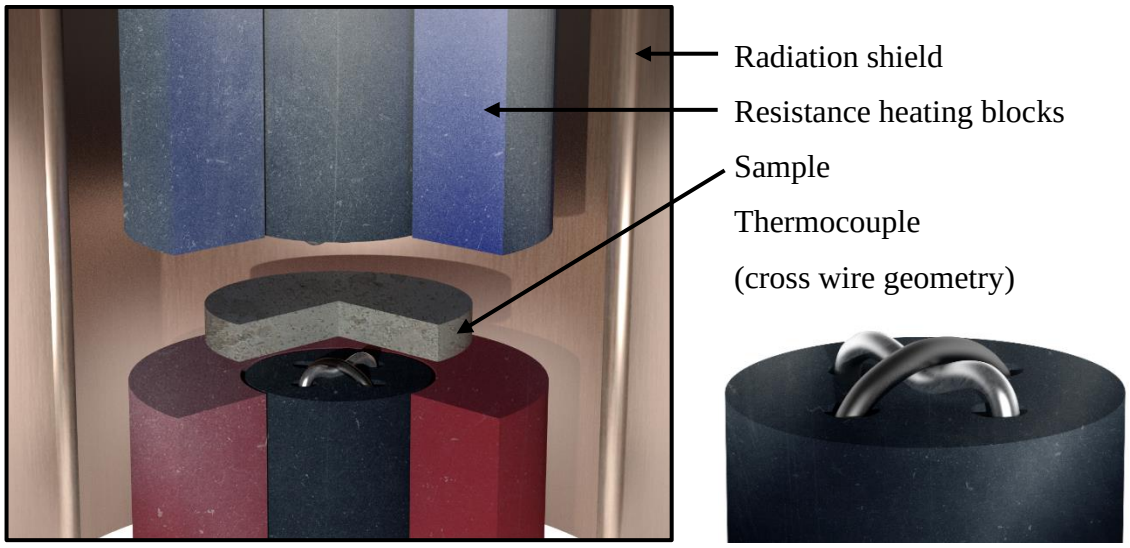

Figure 19. Schematic setup of a thermocouple for the Seebeck coefficient measurement. The upper and lower blocks represent resistive heaters which create a temperature gradient along the pellet. In the middle of the heaters thermocouples can be pressed from each side on the sample, which are able to simultaneously measure voltage and temperature.

The simultaneous measurement of temperature and voltage at both sides of the pellet is achieved by pressing two thermocouples made of chromel-Nb wires with cross wire geometry through holes in the middle of the heaters from each side on the pellet surface. In addition, radiation shields are placed around the heaters to create best possible isothermal conditions. During the measurement the heaters oscillate around a certain average value of temperature. For a series of ΔT the corresponding ΔV are recorded and the Seebeck coefficient can be calculated from the slope of the voltage versus temperature gradient. A good contact between pellet and the hater blocks with thermocouple is highly important for reproducible data. Here it is important to check if the ΔT versus ΔV plots show a linear trend for each data point.

Speed of sound measurements

Normal and shear ultrasonic measurements were performed at room temperature to extract the longitudinal and transverse sound velocities, respectively. Honey was used as the couplant on a Panametrics NDT 5800 pulser/receiver, which was employed with a Tektronix TDS 1012 digital oscilloscope.

Thermal diffusivity

Thermal diffusivity was determined via the laser flash thermal diffusivity method, using a Netzsch laser flash diffusivity instrument (LFA 457). After polishing the samples in order to get a pellet with plane parallel surfaces, pellets were coated with a thin layer of graphite before the measurement in order to maximize the samples emissivity and absorptivity to obtain strong radiation signals in the measurement. The pellets were then placed in a sample holder with a circular cutout at the top and bottom. As Figure 20 illustrates a laser pulse irradiates the sample in a vertical setup at the bottom side. The temperature rise on the backside due to the energy input is detected by an infrared sensor then detects at the top side. The thermal diffusivity α can then be determined from the sample thickness and the time constant of the temperature rise. The thermal diffusivity is related to the thermal conductivity κ via

$$\kappa = \alpha C_v d \ , \qquad 6.1$$

where C_V is the heat capacity and d is the density of the sample. Theoretical densities can be calculated from the molar mass and the lattice parameters derived from Rietveld refinements of the corresponding x-ray powder diffraction data. The heat capacity can either be directly measured, or determined via the Dulong Petit approximation.

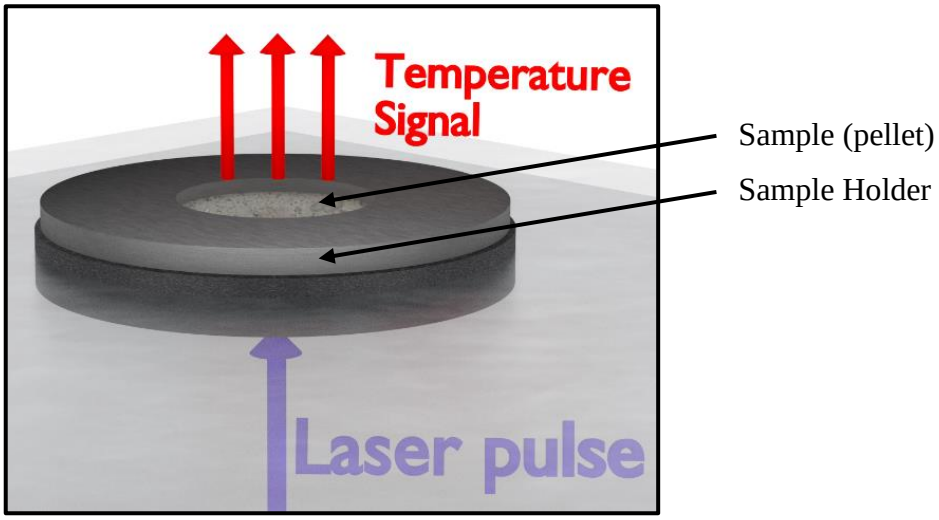

Figure 20. Schematic illustration of the laser flash analysis. After placing the pellet in a sample holder with a circular cutout at the top and bottom, a laser pulse irradiates the sample in a vertical setup at the bottom side. An infrared sensor then detects the time-dependent temperature rise at the top side.

Usually LFA measurements of the thermal conductivity are performed under vacuum. However, due to very small leaks all thermal diffusivity data presented in this work were performed under a slight argon flow.

Electrical resistivity and Hall coefficients.

Besides the electrical resistivity, which is necessary to determine the thermoelectric figure of merit, Hall coefficients also provide helpful information as Hall charge carrier mobilities and Hall charge carrier concentrations can be directly calculated from the Hall coefficients. Due to the direct influence to all thermoelectric transport properties the charge carrier concentration is extremely important for optimizing thermoelectric materials. Furthermore the temperature dependence of the charge carrier mobility provides information about the scattering mechanism of the charge carriers. Electrical resistivity and Hall coefficients were obtained using the Van der Pauw technique with a magnetic field of 2 T and pressure-assisted contacts. The nail shaped contacts are placed on the edges of the disc shaped sample as it is illustrated in Figure 21. The electrical resistivity can be determined by passing a current between two adjacent contacts, while the voltage is measured between the other two. The electrical resistivity can then be calculated from the total resistance *R*. In order to measure the Hall coefficient the sample needs to be placed in a magnetic field perpendicular to the sample plane, which is achieved by placing the sample holder vertically in between two electromagnets as it is shown in Figure 21 (left picture).

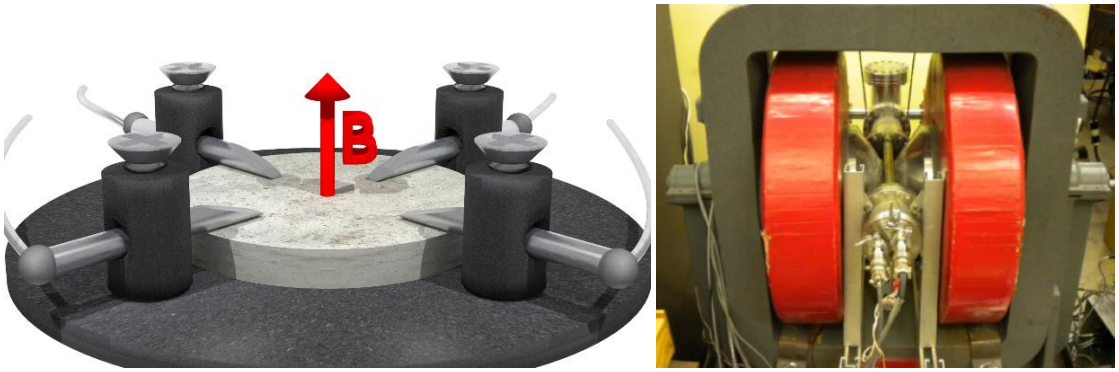

Figure 21. Schematic setup of a 4-point Van der Pauw Hall measurement system. The pellet is pressed on the sample holder with four pressure assisted contact pins. The sample holder is then fixed vertically in a vacuum chamber between two electro-magnets as illustrated right on the Hall measurement system at Caltech.

Under the influence of an altering magnetic field ΔB a current is passed diagonal across the sample and the Hall coefficient R_H can be determined from the average change of the total resistance ΔR as:

$$R_H = l\frac{\Delta R}{\Delta B}\ , \qquad 6.2$$

where l is the sample thickness. In order to obtain reproducible data with small noise, it is crucial that the pellet is freshly polished before the measurement and each nail is in good contact with the sample. A check of the contact resistance before the measurement is advisable here.

Chapter 7

Anion doped copper selenide

Influence of killer defect formation on the doping efficiency and thermoelectric properties of $Cu_{2-y}Se_{1-x}Br_x$

In this chapter we investigate the potential for copper selenide to achieve high *zT* values at room temperature. Using bromine as a dopant we show the effect of carrier scattering on the thermoelectric quality factor and how the dopant bromine itself prevents possibly high figures of merit at room temperature. Furthermore we explore the underlying principle for doping inefficiencies in copper selenides via the intrinsic defect chemistry of this material. We show that doping not only introduces carriers into a semiconductor, but also changes the overall stoichiometry of the host material. In the case of $Cu_{2-\delta}Se$, substitution of Se with Br introduces compensating defects in the form of additional Cu vacancies, which effectively pin the Fermi level and lead to a lower doping efficiency. In the following sections the notation $Cu_{2-y}Se_{1-x}Br_x$ with $y > \delta$ will be used to take account for the additional defects in the Br doped samples.

7.1 Potential for high *zT* at room temperature in $Cu_{2-\delta}Se$.

Figure 22 shows the temperature dependence of thermoelectric properties of different $Cu_{2-\delta}Se$ samples with a nominal composition of $Cu_{2-\delta}Se$. However, a significant variation of the measured transport can be observed, which is related to the intrinsic Cu deficiency δ in $Cu_{2-\delta}Se$ and the resulting changes in n_H. The actual stoichiometry of our Cu_2Se sample is about $Cu_{1.982}Se$. While the Cu vacancy in $Cu_{2-\delta}Se$ is of intrinsic nature, the holes behave extrinsically, and a single parabolic band model can be applied to analyze the transport and predict the optimum carrier densities for a maximum *zT*.[127,24] The resulting prediction of *zT* versus Hall carrier concentration is shown in Figure 23.

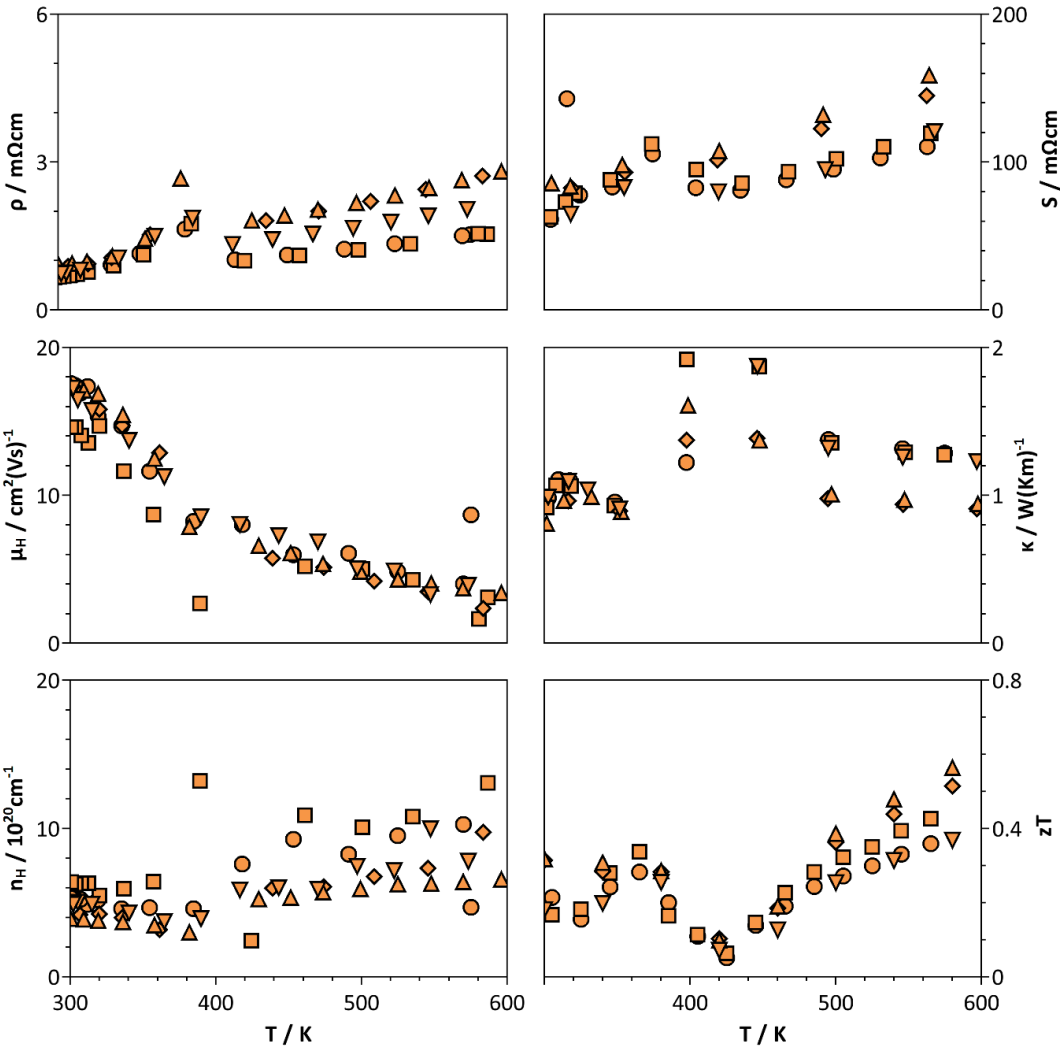

Figure 22. Temperature dependence of the thermoelectric transport data in $Cu_{2-\delta}Se$. Five different copper selenide samples with a nominal composition of $Cu_{2-\delta}Se$ were measured showing the spread of values due to the intrinsic Cu deficiency.

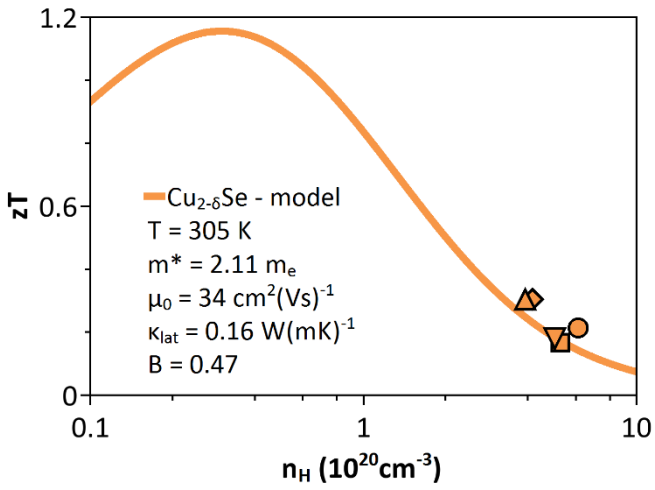

Figure 23. Single parabolic band model of the transport data in $Cu_{2-\delta}Se$ leading to estimates of the effective mass m^*, the mobility parameter μ_0 and the quality factor B allowing a prediction of the thermoelectric figure of merit zT for different carrier concentrations. The model assumes acoustic phonon scattering limits the carrier mobility. Reducing the hole-carrier concentration in $Cu_{2-\delta}Se$ by one order of magnitude is predicted to result in a maximum zT of 1.16 at 305 K.

Copper selenide is predicted to reach a maximum zT of 1.16 at 305 K with a quality factor B of 0.47 (Equation 3). This value is greater than the state-of-the-art zT value for bulk materials at room temperature, which is around 1.1 achieved in $Bi_{2-x}Sb_xTe_3$.[62,148] The large zT value is a result of a relatively high weighed mobility ($\mu_0 m^{*3/2}$) of around 100 cm^2(Vs)$^{-1}$, which is comparable to the values found for PbTe and PbS, in combination with a very low lattice thermal conductivity of 0.16 W(Km)$^{-1}$. The lattice thermal conductivity was obtained using the Wiedemann-Franz law and calculated Lorenz numbers, and is much lower than typical lattice thermal conductivities of 1 W(Km)$^{-1}$ found in thermoelectric materials and possibly a result of the low symmetry crystal structure and high Cu disorder in $Cu_{2-\delta}Se$ at room temperature, which transitions into a molten Cu sublattice at high temperatures. These mechanisms are also responsible for the lattice thermal conductivity of ~0.22 W(Km)$^{-1}$ observed in Cu_7PSe_6. Modeling the thermoelectric transport and predicting where the optimum carrier density has proven to be a powerful tool in thermoelectrics.[149,150,151,152] Figure 23 shows that the samples of copper selenide intrinsically have a Hall carrier concentration of 4-7 × 10^{20} carriers per cm^3, much greater than the optimum value of 3 × 10^{19} cm^{-3}. Doping this material with an electron donor should reduce the amount of holes in $Cu_{2-\delta}Se$ and therefore lower the carrier concentrations into a range of much higher figures of merit.

7.2 Chemical characterization

X-ray powder diffraction data of the synthesized samples are shown in Figure 24. Position and intensity of the observed reflections fit well to other experimental data of copper selenide in the literature.[153,154,155] Rietveld refinements against standard laboratory x-ray powder diffraction data with the published structure models do not provide reasonable information on positions or site occupancies. Se^{2-} and Br^{-} cannot be distinguished by x-ray diffraction techniques due to their similar atomic scattering form factors for x-rays. However, lattice parameters were derived from Pawley-fits using a small, anorthic unit cell derived from a LP search. Related Pawley fits are shown in Figure 25 to Figure 29.

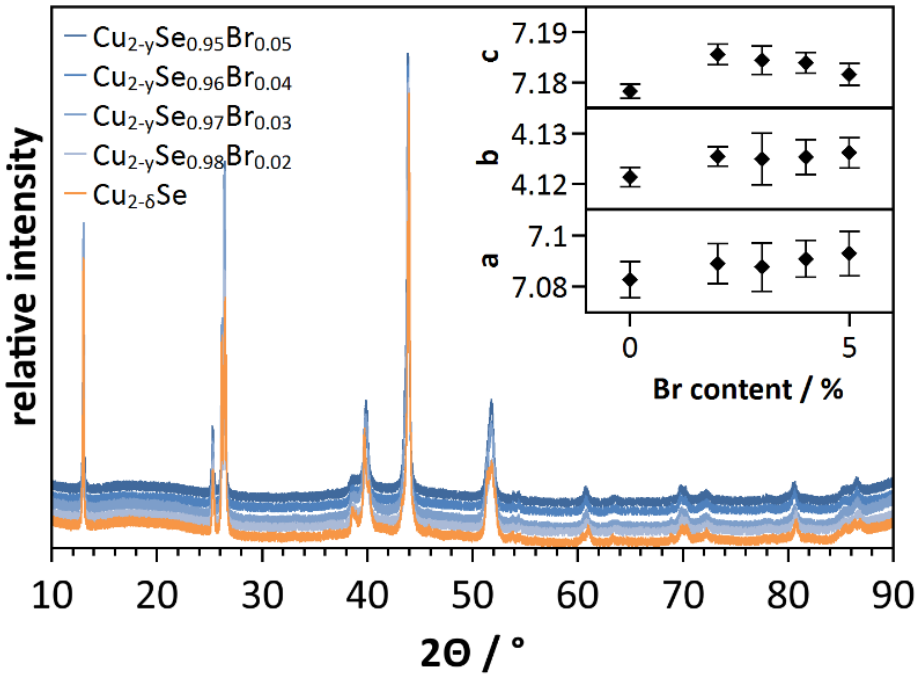

Figure 24. Room temperature x-ray powder diffraction data of $Cu_{2-y}Se_{1-x}Br_x$ with the formal composition $Cu_{2-y}Se_{1-x}Br_x$ (x = 0.00, 0.02, 0.03, 0.04, 0.05). A triclinic anorthic unit cell derived from LP search (TOPAS Academic 4.1) was used in order to determine lattice parameters by Pawley fits for each composition. Lattice parameters show no significant changes with composition, nevertheless the obtained data are in very good agreement with literature diffraction data of $Cu_{2-\delta}Se$. No reflections of starting materials or possible impurity phases could be observed.

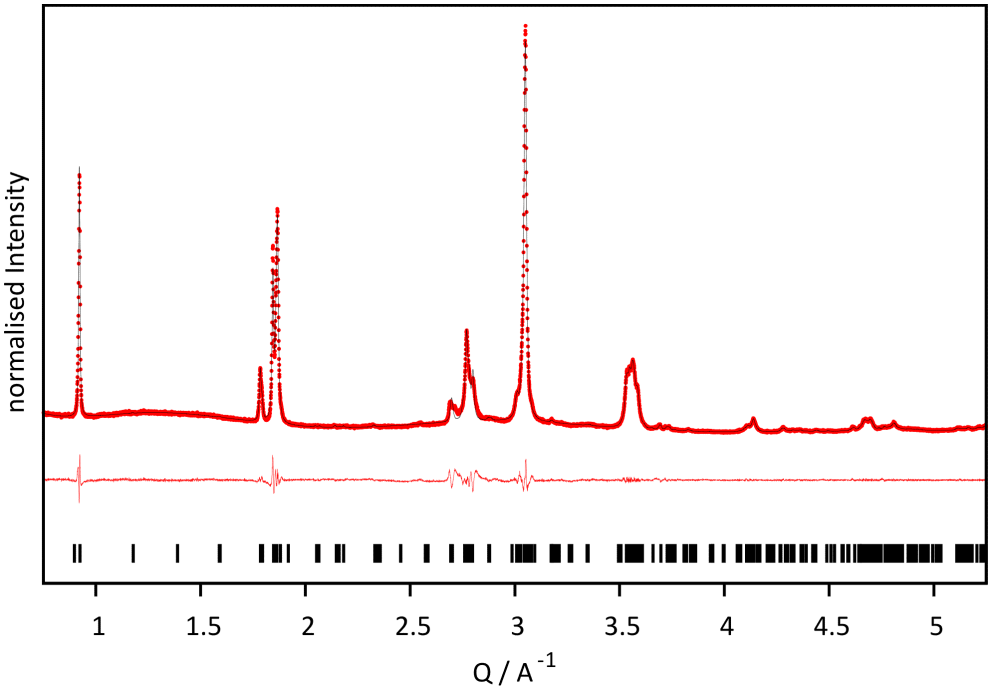

Figure 25. X-ray powder diffraction data for $Cu_{2-y}Se_{1-x}Br_x$ for x = 0 (red dots), including profile fit (black solid line) and profile difference (red solid line) from the corresponding Pawley fit. All reflections could be indexed to a triclinic, anorthic cell with a = 7.083, b = 4.121, c = 7.178, α = 106.1, β = 99.1 and γ = 90.1. No side phases were observed.

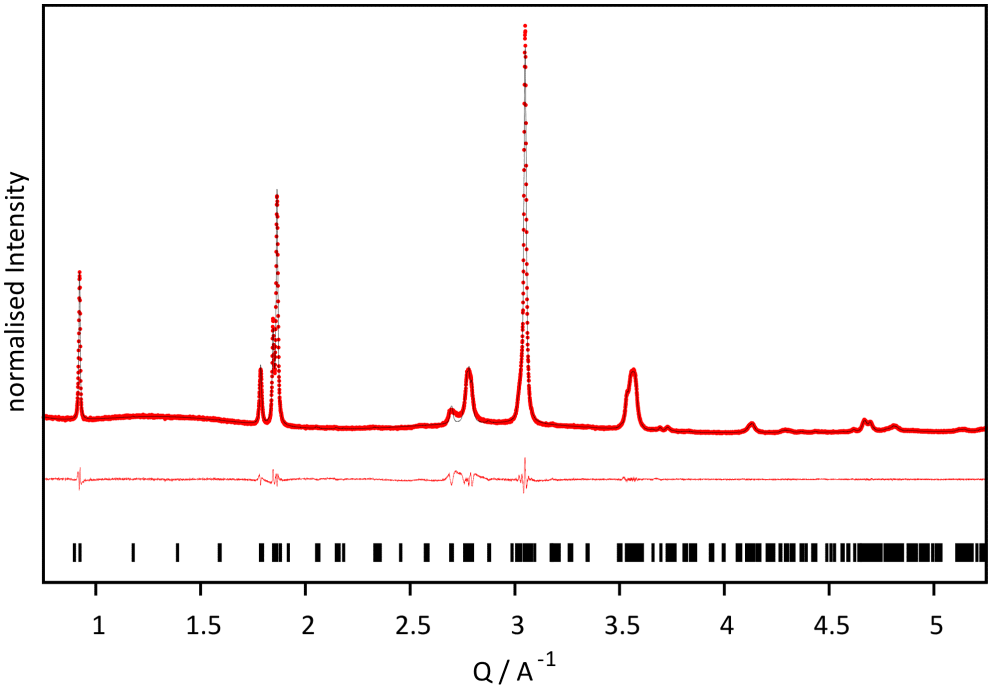

Figure 26. X-ray powder diffraction data for $Cu_{2-y}Se_{1-x}Br_x$ for x = 0.2 (red dots), including profile fit (black solid line) and profile difference (red solid line) from the corresponding Pawley fit. All reflections could be indexed to a triclinic, anorthic cell with a = 7.089, b = 4.126, c = 7.186, α = 106.4, β = 99.0 and γ = 90.0. No side phases were observed.

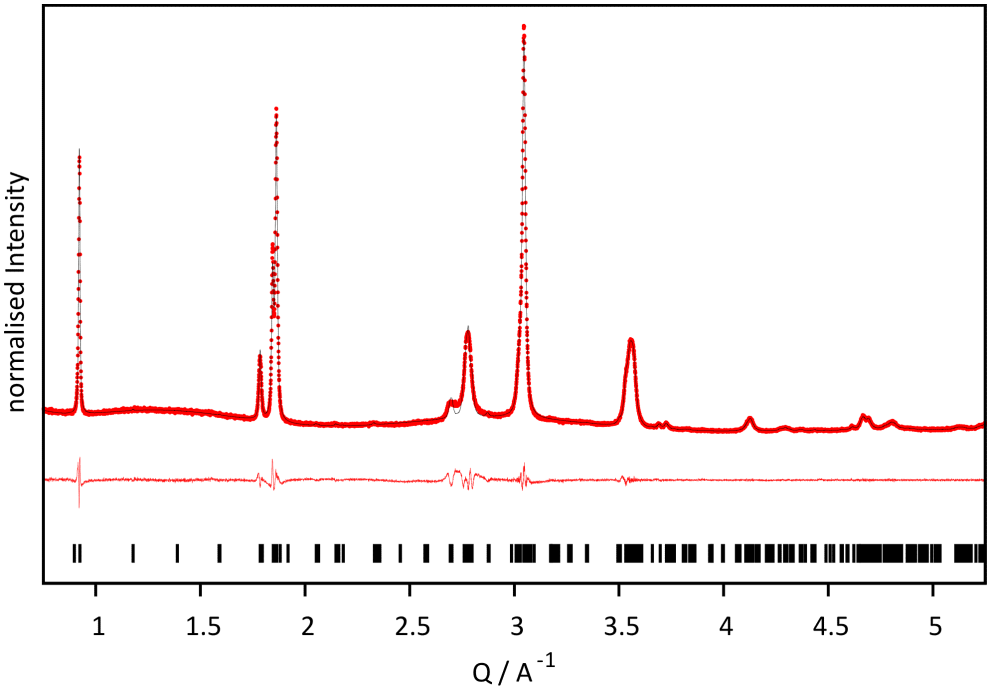

Figure 27. X-ray powder diffraction data for $Cu_{2-y}Se_{1-x}Br_x$ for x = 0.3 (red dots), including profile fit (black solid line) and profile difference (red solid line) from the corresponding Pawley fit. All reflections could be indexed to a triclinic, anorthic cell with a = 7.088, b = 4.125, c = 7.184, α = 106.3, β = 98.9 and γ = 90.2. No side phases were observed.

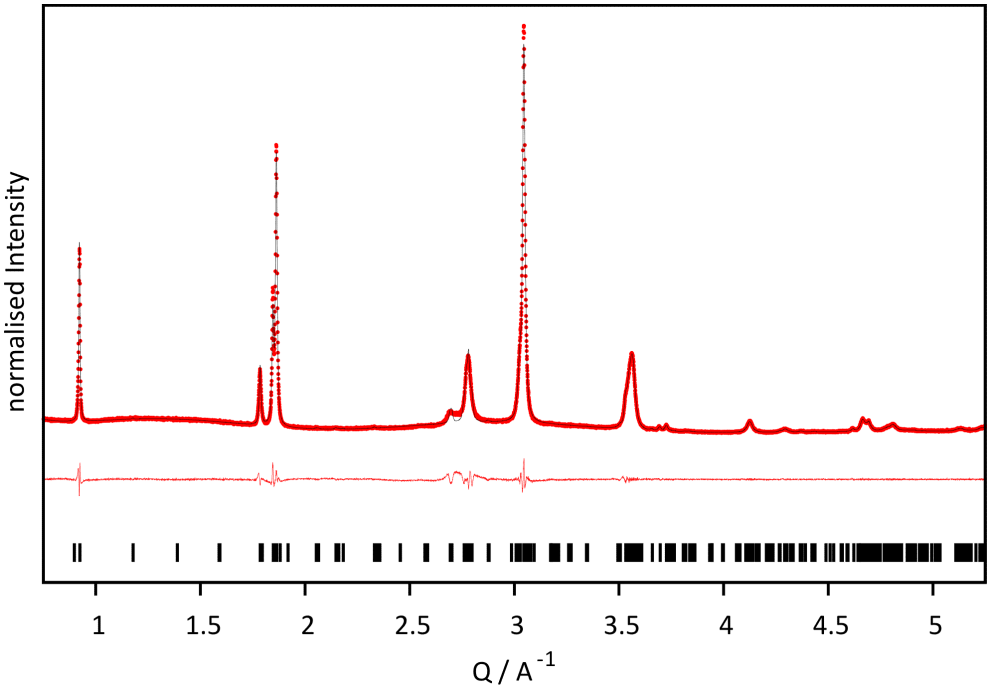

Figure 28. X-ray powder diffraction data for $Cu_{2-y}Se_{1-x}Br_x$ for x = 0.4 (red dots), including profile fit (black solid line) and profile difference (red solid line) from the corresponding Pawley fit. All reflections could be indexed to a triclinic, anorthic cell with a = 7.090, b = 4.125, c = 7.184, α = 106.4, β = 98.9 and γ = 90.2. No side phases were observed.

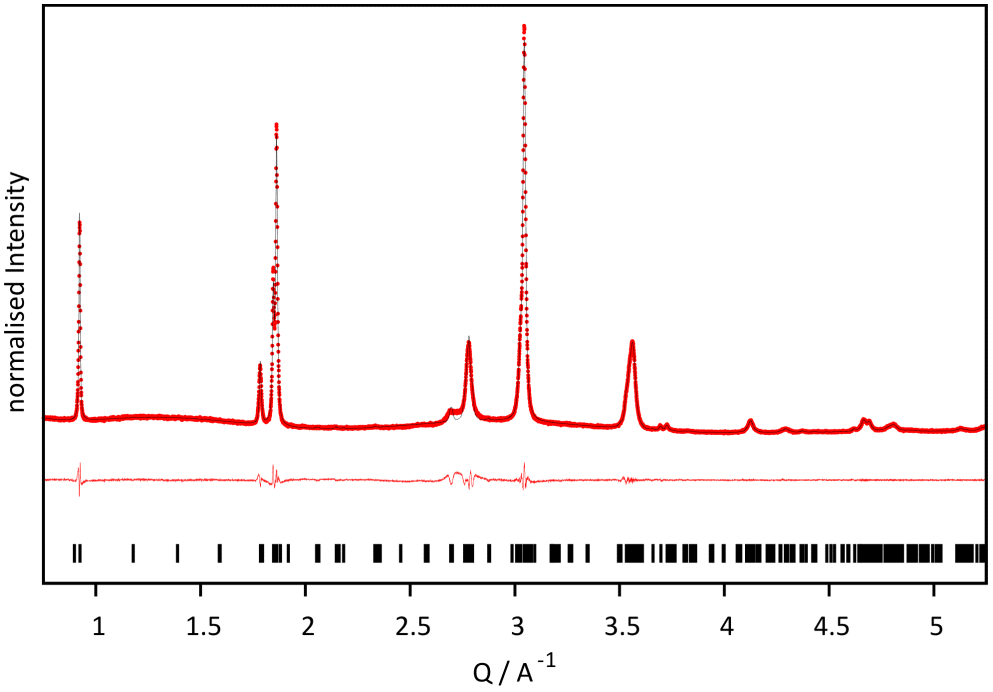

Figure 29. X-ray powder diffraction data for $Cu_{2-y}Se_{1-x}Br_x$ for x = 0.5 (red dots), including profile fit (black solid line) and profile difference (red solid line) from the corresponding Pawley fit. All reflections could be indexed to a triclinic, anorthic cell with a = 7.093, b = 4.126, c = 7.182, α = 106.4, β = 99.0 and γ = 90.2. No side phases were observed.

Lattice parameters for the different compositions do not vary significantly nor do these values display a trend upon increasing bromide concentration, as can be expected from the similar ionic radii of Se and Br. The standard-laboratory x-ray powder diffraction data provides a hint that no secondary phases are present, as there are no signs of remaining starting materials or other crystalline secondary phases, however it does not fully corroborate the extent of formation of a solid solution for substitution of Se with Br.

Besides $Cu_{2-y}Se_{1-x}Br_x$ samples with a substitution grade of selenium versus bromine up to 5 % additional samples have been prepared with a substitution grades of 6 to 10 %. X-ray powder diffraction data of these samples is shown in Figure 30. Unfortunately these samples are not single phase as data from the samples with a substitution grade from 7 to 10 % show reflections of CuBr. In order to rule out phase segregation influences on the transport properties the samples from 6 to 10 % have not been further investigated with respect to thermoelectric properties. To check for a) Br incorporation, b) possible CuBr impurity phases and/or c) differences in the oxidation states resulting from impurity phases, x-ray photoemission spectroscopy (XPS) was used on pellets of the nominal compositions $Cu_{2-\delta}Se$ and $Cu_{2-y}Se_{0.95}Br_{0.05}$.

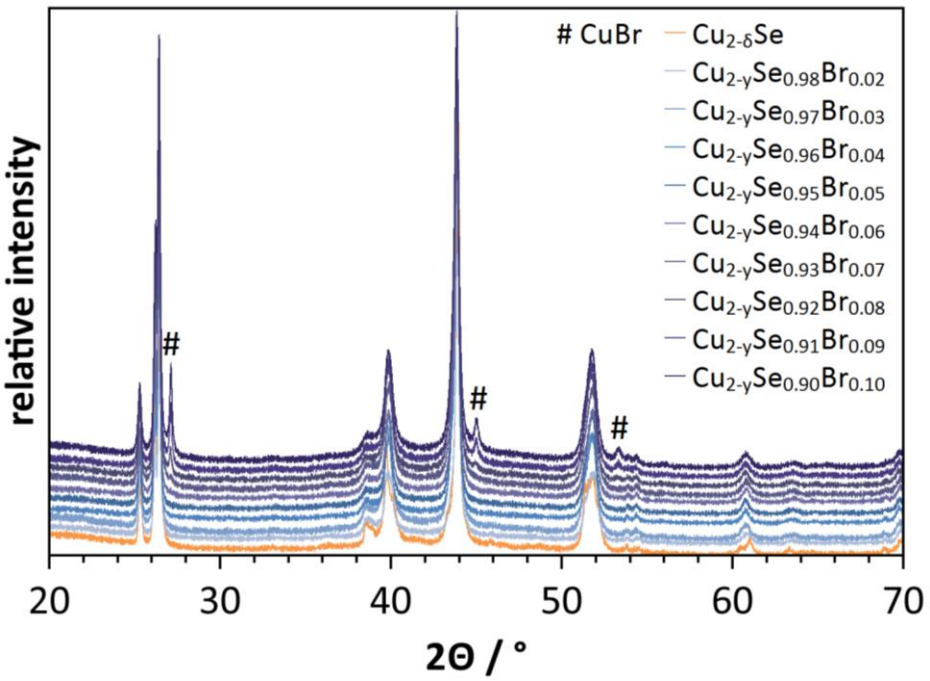

Figure 30. Room temperature x-ray powder diffraction data of $Cu_{2-y}Se_{1-x}Br_x$ with the formal composition $Cu_{2-y}Se_{1-x}Br_x$ (x = 0.00, 0.02, 0.03, 0.04, 0.05, 0.06, 0.07, 0.08, 0.09, 0.10). Samples with a substitution grade from 7 to 10 % show additional reflections (#), which can be attributed to a CuBr impurity phase. In order to rule out phase any influences on the transport properties, the samples from 6 to 10 % have not been further investigated with respect to thermoelectric properties.

Comparing the measured XPS spectra (Figure 31) of the sputtered $Cu_{2-\delta}Se$ sample with previously reported XPS data,[156,157] neither significant differences in peak position and peak shape nor additional peaks can be observed, indicating that no side phases or other oxidation states are present in the sample. For copper selenides this is particularly important, because they exhibit low carrier mobilities and an impurity phase with high mobility would dominate the transport.[158] The presence of bromide ions in the doped sample can also be verified, as the corresponding 3d peak can only be seen in the doped sample.

In addition, a shoulder on the high binding energy side can be observed in the Cu $2p^{3/2}$ and Se 3d peaks in the undoped but not in the doped sample. The account for the shoulder is not entirely clear, but it might be due to slight variations of the local bonding environment in the undoped sample. Since Br^- is expected to be an n-type dopant (electron donor), additional analysis with respect to the exact composition and the Br content is highly important in order to understand the thermoelectric transport properties.

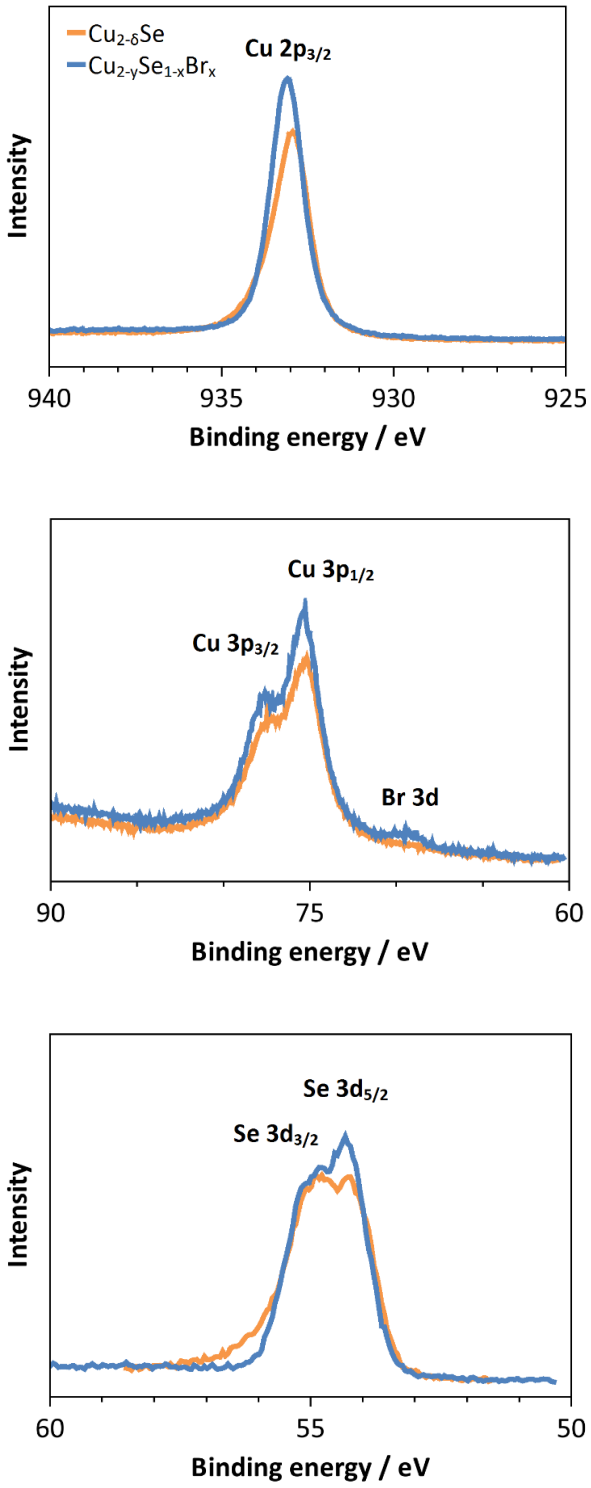

Figure 31. XPS core level spectra of $Cu_{2-\delta}Se$ and nominal $Cu_{2-y}Se_{0.95}Br_{0.05}$ (orange and blue). After sputtering, only intensities from copper and selenium can be observed in the undoped sample and additionally bromine in the Br-doped sample. Comparing with standard CuO and Cu_2O spectra, there are no features of oxidation in the investigated samples.[159] In combination with the diffraction data, the samples can therefore be considered as phase pure. Comparing doped and undoped samples directly, slight changes in peak position and peak shape can be observed, indicating that the local bonding environment might be slightly different in the investigated samples.

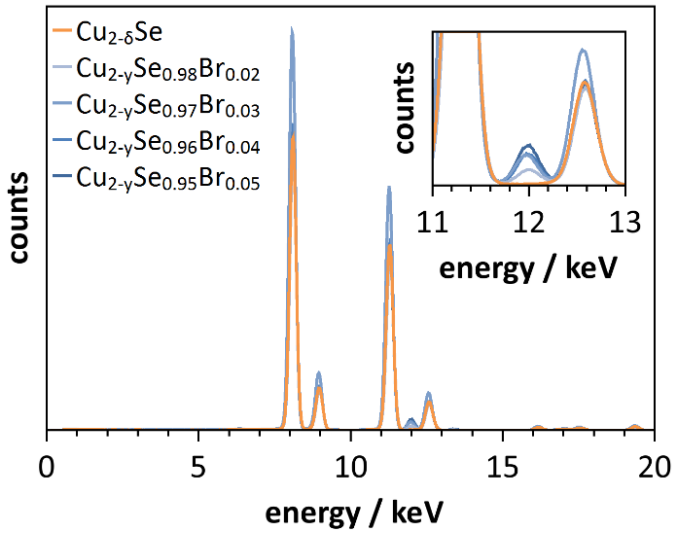

Figure 32. XRF spectra for the investigated copper selenide samples in order to obtain a precise atomic percent ratio of bromine to selenium in each synthesized $Cu_{2-y}Se_{1-x}Br_x$ sample.

X-ray fluorescence (XRF) analyses were utilized in order to obtain the exact ratios of bromine to selenium in each sample (Figure 32). Due to an additional Cu signal in the XRF spectra from the sample holder the relative Cu-Se composition cannot be extracted via XRF and relative changes in the copper to selenium ratios were obtained using inductively coupled plasma mass spectroscopy. Assuming that the undoped sample has the nominal composition of Cu_2Se, the changes in the stoichiometry of the doped samples can be calculated and are shown in Figure 33 and Table 2.

Table 2. Relative composition of $Cu_{2-y}Se_{1-x}Br_x$ with respect to the undoped sample with the nominal composition $Cu_{2-\delta}Se$. First, the ratio of selenium versus bromine has been determined for the investigated samples by x-ray fluorescence (XRF) analysis. Second, relative changes in the copper to selenium ratio could be determined using inductively coupled plasma mass spectroscopy (ICP-MS).

x nominal	x (XRF)	1-x (XRF)	y (ICP-MS)
0.00	0.000	1.000	0
0.02	0.022 ± 0.001	0.978	0.005 ± 0.014
0.03	0.032 ± 0.001	0.968	0.030 ± 0.014
0.04	0.043 ± 0.001	0.957	0.027 ± 0.014
0.05	0.058 ± 0.001	0.942	0.037 ± 0.013

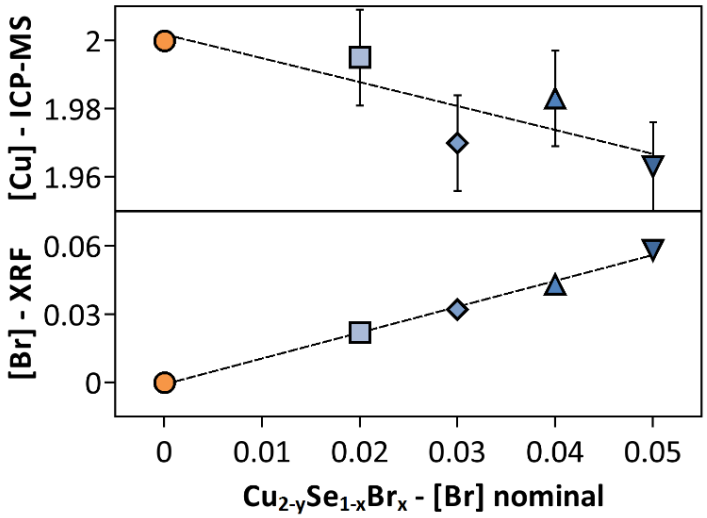

Figure 33. Composition of $Cu_{2-y}Se_{1-x}Br_x$ with the relative changes in the copper content [Cu] determined using ICP-MS and the Br content [Br] determined by XRF. With increasing Br substitution for Se, the Cu content in the matrix decreases as well, leading to a larger Cu non-stoichiometry. Error bars in the ICP-MS analyses represent the standard error, the error bars in the XRF analyses are smaller than the symbols.

First of all, these data show an increasing amount of bromide ions in the samples with increasing synthetic content. While the absolute values are slightly higher than expected, this shows the stoichiometric incorporation of Br for Se. Using the ICP-MS data, the relative amount of copper with respect to selenium and bromine decreases with increasing bromine concentration. In other words, with the increasing substitution of Se with *x* Br in $Cu_{2-y}Se_{1-x}Br_x$, the amount of Cu decreases as well, leading to a larger Cu non-stoichiometry as already observed for the undoped $Cu_{2-\delta}Se$ ($y > \delta$).[143,126]

Therefore, y is influenced by both the intrinsic Cu non-stoichiometry of δ in $Cu_{2-\delta}Se$ and the change in x. As the absolute value of δ is small and there is a wide range of stoichiometric deviation in $Cu_{2-\delta}Se$, all compositions determined for $Cu_{2-y}Se_{1-x}Br_x$ are regarded with respect to Cu_2Se ($\delta = 0$) in Figure 32 (right). Here, the relative changes in the Cu content show that when two bromide ions are substituted for two selenium ions, the material becomes more deficient of roughly one Cu ion. The occurrence of this interesting defect chemistry and its influence on the thermoelectric transport will be discussed below.

7.3 Thermoelectric transport properties in $Cu_{2-y}Se_{1-x}Br_x$.

Since copper selenide is intrinsically a material with extrinsic p-type behavior, an n-type dopant will be needed. A possible candidate is Br as substituent on the Se site. Measured transport properties of $Cu_{2-y}Se_{1-x}Br_x$ are shown in Figure 34.

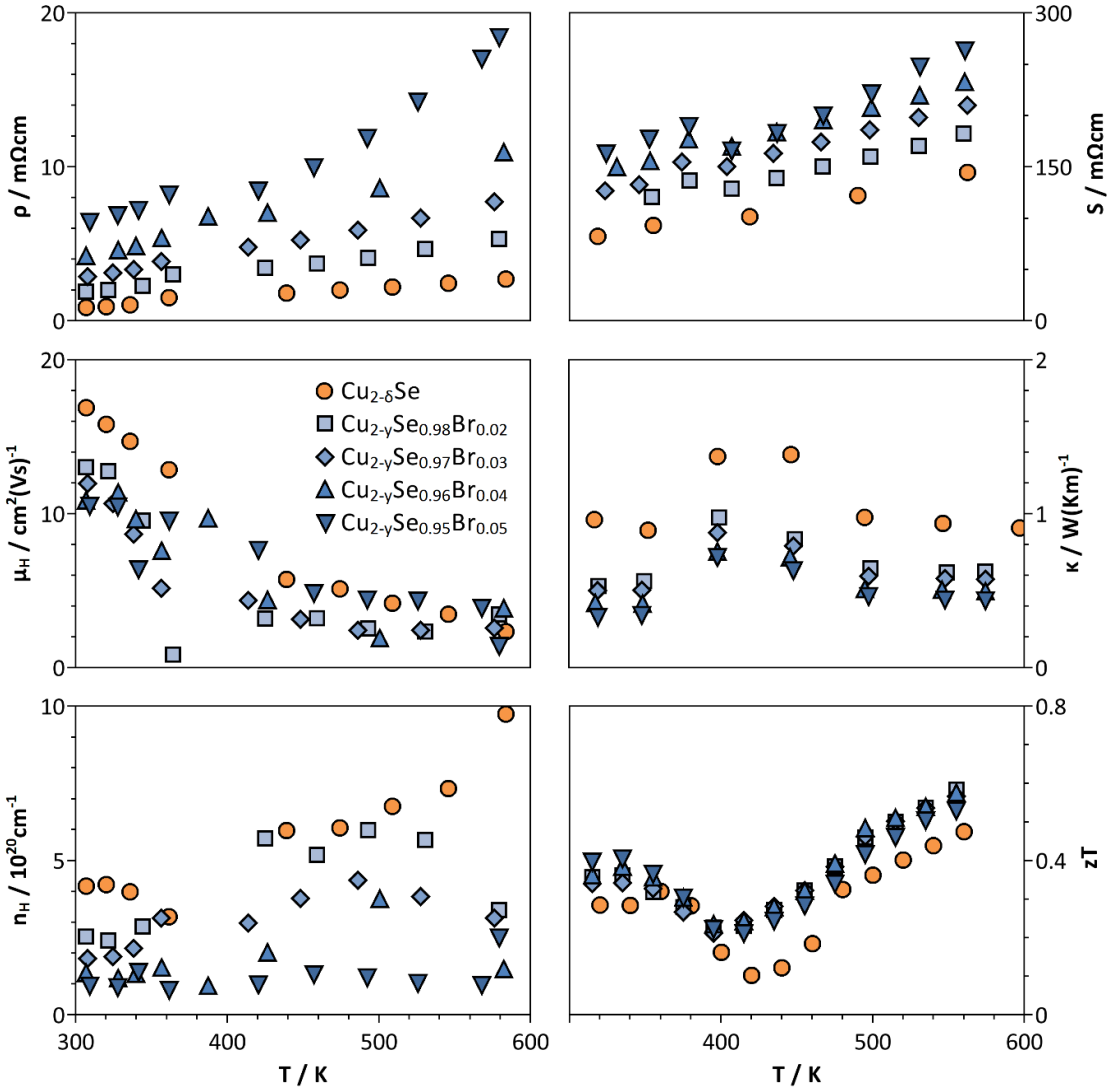

Figure 34. Temperature dependence of the transport properties in $Cu_{2-y}Se_{1-x}Br_x$ with x = 0.00 (orange circles), 0.02 (blue squares), 0.03 (blue diamonds), 0.04 (blue upward triangles) and 0.05 (blue downward triangles). Bromine works as an n-type dopant in copper selenide. With increasing amount of bromide ions the electrical resistivity ρ and the Seebeck coefficient S increase over the investigated temperature regime due to the decreasing hole carrier concentration n_H. The total thermal conductivity decreases as well as a result of the reduced electronic contribution. Note that the Hall mobility μ_H decreases with decreasing Hall carrier concentration and the zT values of the doped samples only increase slightly.

Bromine has been shown to be a very effective n-type dopant in PbTe and PbSe thermoelectrics.[160,161] Copper selenide has been doped with iodine before, but this did not create an appreciable change in the room-temperature *zT*, and no Hall carrier concentrations were reported.[155,162] Comparing the transport of an undoped material (x = 0.0) with a large hole carrier concentration with the data for doped samples, it is clear that substituting Br for Se has the desired effect of reducing the carrier concentrations. The Seebeck coefficient and Hall carrier concentrations are all positive, indicating holes as the majority carriers in this system. The Hall carrier concentration n_H of the holes decreases as the amount of Br increases. The resistivity ρ and the Seebeck coefficient *S* both increase as x increases. The samples with x greater than zero all have markedly lower thermal conductivity than $Cu_{2-\delta}Se$ due to the reduced electronic contribution via the Wiedemann-Franz law.

7.4 Defect formation mechanism and compensating defects.

While the substitution of Br for Se clearly decreases the Hall carrier concentrations of the holes, the actual changes are lower than expected. The doping efficiency of Br, calculated with respect to the high carrier concentration of the undoped $Cu_{2-\delta}Se$ is below 100% (Figure 35a). Table 3 shows the expected and measured carrier concentrations as well as the doping efficiencies.

Table 3. Measured and expected charge carrier concentration for $Cu_{2-y}Se_{1-x}Br_x$. Here, the expected charge carrier concentration represents 100 % doping efficiency with respect to the undoped sample. With the relative differences to the undoped sample the doping efficiency for the measured carrier concentrations can be calculated.

x / %	cc (measured) / $10^{20}cm^{-3}$	cc (expected) / $10^{20}cm^{-3}$	Doping efficiency / %
0	4.9	4.9	0
2.2	2.7	0.3	48
3.2	1.9	-1.7	44
4.3	1.5	-4.0	38
5.8	0.9	-7.1	33

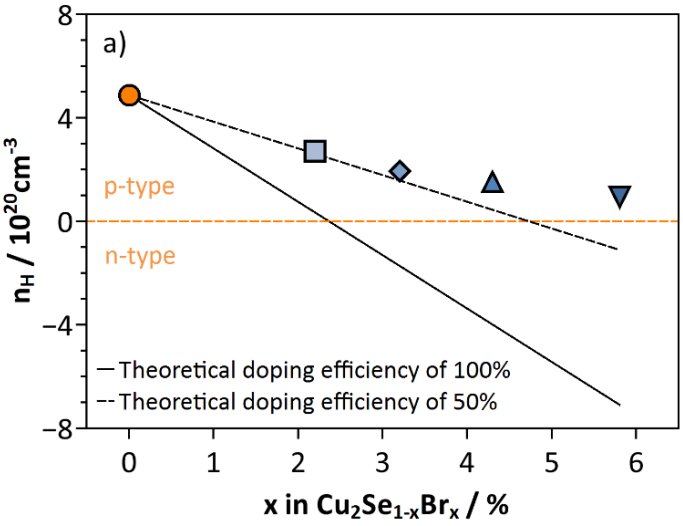

Figure 35. Doping efficiency of Br in $Cu_{2-y}Se_{1-x}Br_x$. The measured Hall carrier concentration is lower than the expected carrier concentration, calculated for one electron introduced per bromide ion.

While Br usually shows high doping efficiencies,[163] low doping efficiencies in thermoelectric materials are not uncommon and often occur visibly in conjunction with phase segregations due to the Fermi level moving deeper into the band. In this case, however, no secondary phases can be detected by powder x-ray diffraction or XPS. Furthermore, while usually the direction for doping is to move the Fermi level deeper into a band, i.e. increasing the carrier concentration, in this case the substitution aims at moving the Fermi level towards the band edge in an attempt to decrease the amount of carriers present. As seen in Figure 32, with increasing amount of Br the amount of Cu in the samples decreases. Starting from the intrinsic material $Cu_{2-\delta}Se$, the synthesis does not result in a stoichiometric Cu_2Se but leads to $Cu_{2-\delta}Se$ with an excess amount of metallic copper after the synthesis (1). Even though this excess amount of copper has been removed from the reaction product before hot-pressing, it can be regarded as a phase segregation.

The intrinsic, Cu-defective $Cu_{2-\delta}Se$ can be expressed in the Kröger-Vink notation (2),[164] showing that the copper vacancy V'_{Cu} acts as an acceptor and introduces one hole $\delta h^{\bullet}$ per copper vacancy.

$$Cu_2Se \rightarrow Cu_{2-\delta}Se + \delta Cu \quad (1)$$

$$Cu_{2-\delta}Se = 2Cu_{Cu}^{\times} + Se_{Se}^{\times} + \delta V'_{Cu} + \delta h^{\bullet} \quad (2)$$

Note that for simplicity, in equations (3) and (5) the reaction is written using the atomic elements, not the actual synthetic reaction with CuBr. N-type doping with Br^- should lead to a material with composition $Cu_2Se_{1-x}Br_x$ (4), if there were no Cu vacancy formation involved at all, leading to electrons due to the donor Br on the Se site $Br_{Se}^{\bullet}$:

$$2Cu + (1-x)Se + xBr \rightarrow Cu_2Se_{1-x}Br_x \quad (3)$$

$$Cu_2Se_{1-x}Br_x = 2Cu_{Cu}^{\times} + (1-x)Se_{Se}^{\times} + xBr_{Se}^{\bullet} + xe' \quad (4)$$

However, a Cu vacancy mechanism is involved (5,6) where the resulting composition is $Cu_{2-y}Se_{1-x}Br_x$ with y depending on the starting value of δ and x. Equation (6) shows in defect notation how the electrons, created by Br donors $Br_{Se}^{\bullet}$ are partially compensated by the holes resulting from Cu vacancy formation.

$$2Cu + (1-x)Se + xBr \rightarrow Cu_{2-y}Se_{1-x}Br_x + yCu \quad (5)$$

$$Cu_{2-y}Se_{1-x}Br_x \quad (6)$$

$$= 2Cu_{Cu}^{\times} + yV_{Cu}' + (1-x)Se_{Se}^{\times} + xBr_{Se}^{\bullet} + xe' + yh^{\bullet}$$

Comparing the compositions in Figure 33, it seems that the material becomes slightly more Cu deficient with ~ 0.5 Cu vacancies per Br introduced into the system. While bromine introduces an electron into the system, the resulting 0.5 Cu vacancies will introduce half a hole in comparison, leading to a doping efficiency of 50%. This can indeed be observed for lower values of x, whereas at higher doping content the change in the carrier concentration flattens out (Figure 35). The drop in efficiency can be related to segregation (or non-reaction) of CuBr, which should introduce even more holes. As the samples with larger synthetic amount of Br ($x > 0.7$) showed CuBr as secondary phases, this mechanism seems reasonable. While vacancy formation has already been shown to have an important effect on the carrier concentration in AZn_2Sb_2 Zintl phases,[165,166] the compositional data and the resulting carrier concentrations clearly show the influence of Cu vacancy formation as a compensating defect in this material. Zunger has provided a model to understand the influence of defects on the Fermi level in semiconductors.[167] For instance, when an electron producing dopant (donor, Br^- in this case) becomes incorporated in a solid it raises the Fermi level.

When the Fermi level is raised further into the conduction band, at some point the defect formation enthalpy of acceptor defects becomes negative and acceptor defects such

as cation vacancies or interstitials are created (Figure 36). These acceptor defects act as "killer defects", effectively pinning the Fermi level to a maximum.[167] In the case of a p-type material, hole doping (introducing an acceptor) will shift the Fermi level deeper into the valence band and the competing mechanism is either the formation of anion vacancies or cation interstitials, which will also result in the pinning of the Fermi level via killer defects. In the case of $Cu_{2-y}Se_{1-x}Br_x$ the occurrence of copper vacancies V^{-}_{Cu} as "killer dects" occurs when moving the Fermi level closer to the valence band edge and not further into the conduction band. The intrinsic material $Cu_{2-\delta}Se$ already is deficient in Cu, i.e. $\delta > 0$, due to entropic reasons leading to a temperature and intrinsic defect enthalpy dependence of δ. With increasing Br content, the defect formation enthalpy for copper vacancies V'_{Cu} becomes negative (Figure 36, orange line).

This response an also be considered along the lines of Le Chatelier's principle because adding Br alters a system which has an equilibrium Cu defect concentration and Fermi level. The system then adjusts to partially counteract the raising of the Fermi level caused by Br substitutional defects by increasing the concentration of the compensating, copper vacancy defect. In other words, the dependence of the defect formation enthalpy for V'_{Cu} in $Cu_{2-\delta}Se$ is shifted to values where any increase in the Fermi level will introduce more Cu vacancies, which ultimately act as compensating defects in the valence band.

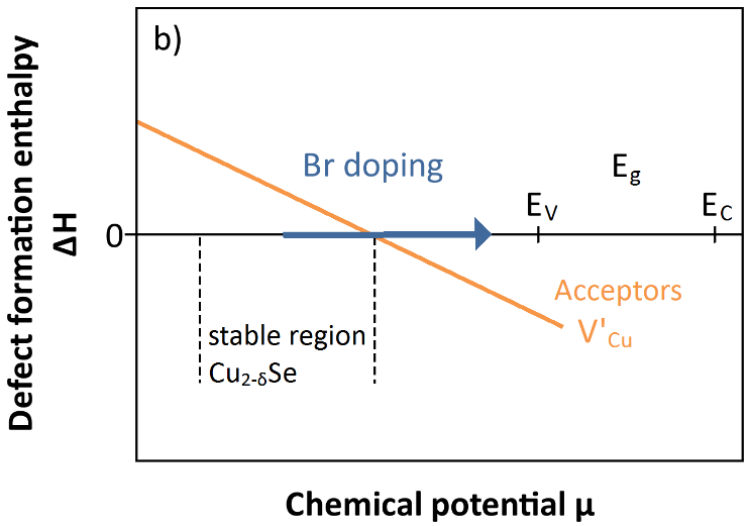

Figure 36. Schematic defect formation enthalpy for $Cu_{2-y}Se_{1-x}Br_x$. The shifting Fermi level to higher energies with increasing Br content x leads to a decreasing (more negative) formation enthalpy of Cu vacancies. The intrinsic defect chemistry leads to the observed lower doping efficiency of 50%, where each bromide ion creates half a killer vacancy of Cu.

7.5 Charge carrier scattering mechanism.

While the parabolic band model in Figure 23 predicts an improvement of the figure of merit at room temperature, the measured *zT* values do not exceed unity, and those at high temperatures are only slightly greater than the *zT* values of $Cu_{2-\delta}Se$. This is in accordance with the findings for iodine doped $Cu_{2-\delta}Se$.[155] To understand why doping with Br did not result in the predicted high *zT* values, we look at the results of the SPB model for data at 305 K, shown in Figure 37. All parameters for the model at 305 K and a full transport model and description for the temperature of 550 K can be found in the Supporting Information. Figure 37b shows a prediction of how *S* should change with n_H in copper selenide using Pisarenko relations. Orange symbols denote $Cu_{2-\delta}Se$ and blue symbols denote $Cu_{2-y}Se_{1-x}Br_x$. Each material was analyzed separately.

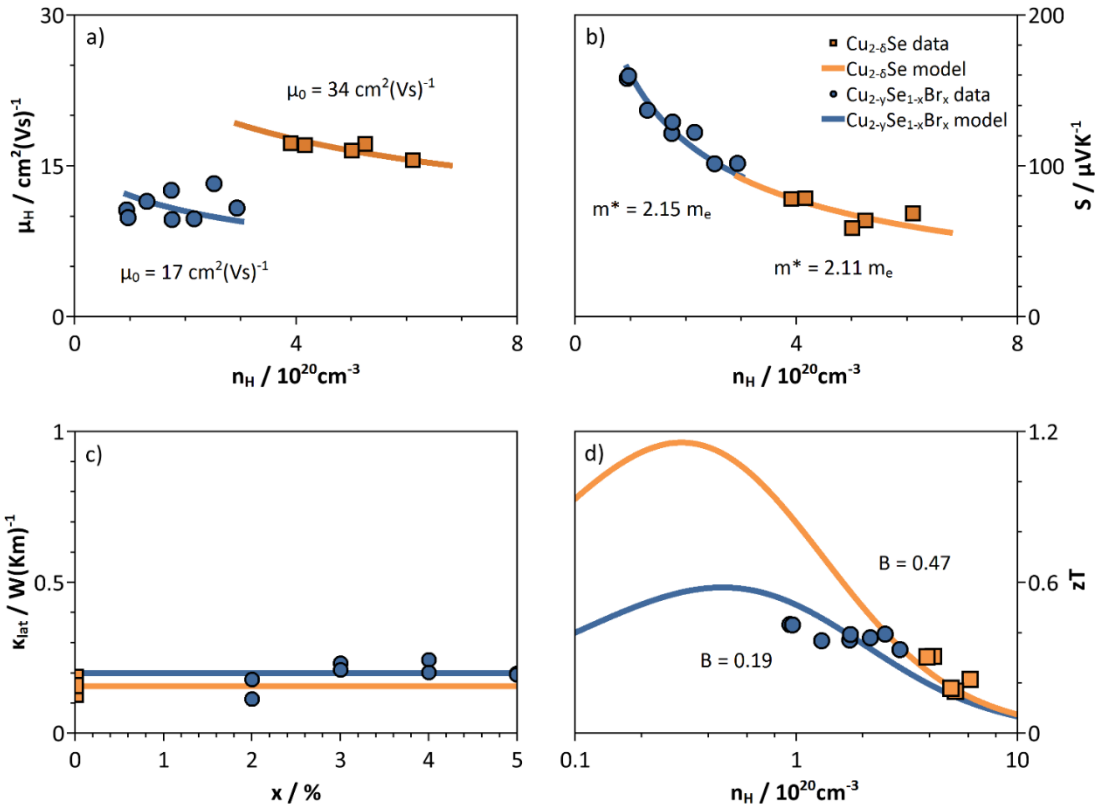

Figure 37. Results for the SPB model for $Cu_{2-\delta}Se$ and $Cu_{2-y}Se_{1-x}Br_x$ at 305 K under the assumption of acoustic phonon scattering. The Pisarenko relation (a) predicts how *S* changes with n_H in copper selenide. Orange squares denote $Cu_{2-\delta}Se$ and blue circles denote $Cu_{2-y}Se_{1-x}Br_x$. The effective masses are basically identical and Br does not have a huge influence on the curvature of the valence band of $Cu_{2-\delta}Se$. However, the n_H dependence of the mobility parameter does not represent the expected trends (modeled lines) for acoustic phonon scattering (a) as n_H increases slightly with μ_H for $Cu_{2-y}Se_{1-x}Br_x$.

The effective masses for each material are within 2 % of one another and it appears that Br does not change the curvature, and hence density of states effective mass, of the valence band of $Cu_{2-\delta}Se$. The values for the lattice thermal conductivity (Figure 37c) are also the same within the measurement uncertainty, 0.16 and 0.20 W $(Km)^{-1}$ for $Cu_{2-\delta}Se$ and $Cu_{2-y}Se_{1-x}Br_x$, respectively. The most striking difference between the two materials is the change in the mobility parameter (Figure 37a). Copper selenide has a mobility parameter of 34 $cm^2(Vs)^{-1}$, but $Cu_{2-y}Se_{1-x}Br_x$ has a mobility parameter of only 17 $cm^2(Vs)^{-1}$. It appears that adding Br drastically reduces the mobility of the holes in the valence band. In a material influenced by a single parabolic band and with acoustic phonons as the main scatterers of electrons, the Hall mobility should decrease with increasing Hall carrier concentration.[168,169] The Hall mobility data for $Cu_{2-y}Se_{1-x}Br_x$ in Figure 37a exhibit a slight upward trend with Hall carrier concentration. In order to understand this unexpected behavior, we need to incorporate another scattering mechanism to understand this contradiction of our assumptions. The scattering mechanism for electrons and holes has been discussed in section 2.6. Since two kinds of atoms occupy the Se site (Se and Br), it is logical to include an alloy scattering mechanism (equation 2.18). The densities, and respective speeds of sounds for the different compositions can be found in Table 4. As stated in chapter 2.6, the total relaxation time τ is related to the total scattering rate $1/\tau$.

$$\tau^{-1} = \tau_{ac}^{-1} + \tau_{alloy}^{-1} \qquad 7.1$$

The scattering mechanism determines the parameter λ, which in turn determines the order of the Fermi integrals used to calculate the transport properties. Since τ_{ac} and τ_{alloy} have the same dependence on λ (λ = 0), including alloy scattering into the modeling does not change the order of the Fermi integrals, and μ_0 can be modeled separately. Using τ and the effective mass m^* the mobility parameter μ_0 can be calculated via:

$$\mu_0 = e\tau/m^* \qquad 7.2$$

Applying the combined acoustic phonon/alloy scattering model to values of μ_0 computed for each value of x with the deformation potential Ξ and the alloy scattering potential U as free parameters, we obtain a deformation potential of 5.8 eV and an alloy scattering potential of 1.1 eV.

Table 4. Densities and speeds of sound data of $Cu_{2-\delta}Se$ and $Cu_{2-y}Se_{1-x}Br_x$ at room temperature.V_l represents the longitudinal speed of sound, v_t represents the transverse speed of sound.

x nominal	d kgm^{-3}	v_l ms^{-1}	v_s ms^{-1}
0.00	6618	3250	1860
0.02	6530	3250	1270
0.03	6542	2700	1350
0.04	6444	2900	1270
0.05	6336	2640	1270

The deformation potential obtained for $Cu_{2-y}Se_{1-x}Br_x$ is equal to that obtained for $Cu_{2-\delta}Se$ and alloy scattering potentials around 1.1 can be found in several other solid solutions like n-type $PbSe_{1-x}Te_x$, $Cd_{1-x}Zn_xTe$ or $Al_{1-x}Ga_xAs$.[170,171,172] The Hall mobility versus Hall carrier concentration curve accounting for acoustic phonon and alloy scattering is shown in Figure 38, showing that due to increased alloy scattering via Br introduction a reduction of the mobility can be observed. This reduction in μ_0 in the Br-doped samples due to alloy scattering reduces the quality factor B (Eq. 13) of $Cu_{2-\delta}Se$ from 0.47 to 0.19 (Figure 37d). The quality factor B is a measure of the maximum zT at a given temperature and is given by:[173,174]

$$B = \frac{8\pi e}{3}\left(\frac{k_B}{e}\right)^2\left(\frac{2m_e k_B}{h^2}\right)^{3/2}\frac{\mu_0(m^*/m_e)^{3/2}T^{5/2}}{\kappa_{lat}} \qquad \text{(Eq. 3)}$$

While Br acts as an electron donor, i.e. it reduces the hole carrier concentration and increases the Seebeck coefficient, the additional scattering from the dissimilar atoms on the anion site reduces the maximum possible zT to 0.6. Figure 37d shows how the figure of merit's increase with decreasing carrier concentration slows down due to a changing mobility. Similar effects have been observed in lead chalcogenides and has recently systematically been investigated by Wang et al.,[163] where it was shown that the mobility reduction due to chemical substitution on a certain sublattice depends on its contribution to the charge conducting band.

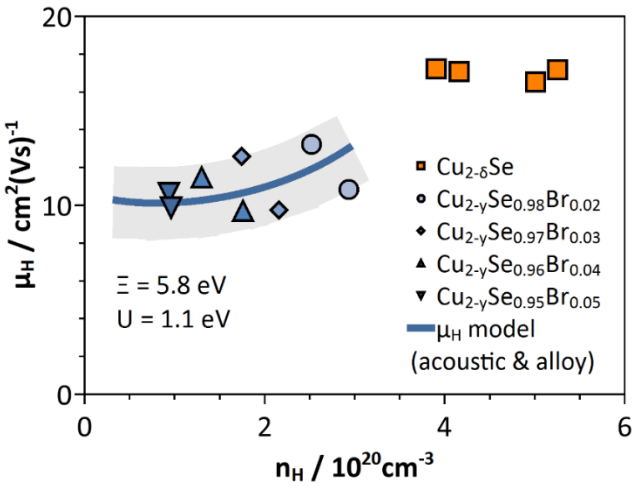

Figure 38. Hall mobility versus Hall carrier concentration at 305 K in $Cu_{2-y}Se_{1-x}Br_x$ for the undoped (orange squares) and doped (blue) samples. Two pellets for each composition with x>0 were measured. The blue line represents the model for the Hall mobility including acoustic phonon and alloy scattering. An error in mobility of 10% is represented by the thick grey line. Alloy scattering can explain decreasing mobility for the doped samples using a deformation potential of 5.8 eV and an alloy scattering potential of 1.1 eV.

The huge degree of mobility reduction observed in $Cu_{2-y}Se_{1-x}Br_x$ indicates a high contribution of the anion atomic orbitals to the valence band states close to the Fermi energy, which strongly influences the hole mobility. Due to the complex crystal structure at room temperature, band structure calculations are only available for the high temperature modification. However, the available calculations show a large contribution of the anion sublattice to the valence band at high temperature.[175] It should be noted, however, that another possible scattering mechanism could be ionized impurity scattering, which would express itself as an increase of the Hall carrier mobility at higher carrier concentrations, due to screening effects.[176] One might think that ionized impurity scattering would play a role in $Cu_2Se_{1-x}Br_x$ due to the charge differences in Se^{2-} and Br^- and an upward trend of μ_H with n_H can indeed be seen. A combined acoustic phonon and ionized impurity scattering model was applied to the data at 305 K using the equation for the ionized impurity scattering relaxation time (equation 2.14) and 11.6 for the relative permittivity of $Cu_2Se_{1-x}Br_x$.[177] The S versus n_H data along with curves resulting from combining acoustic phonon scattering with ionized impurity and alloy scattering are shown in Figure 39.

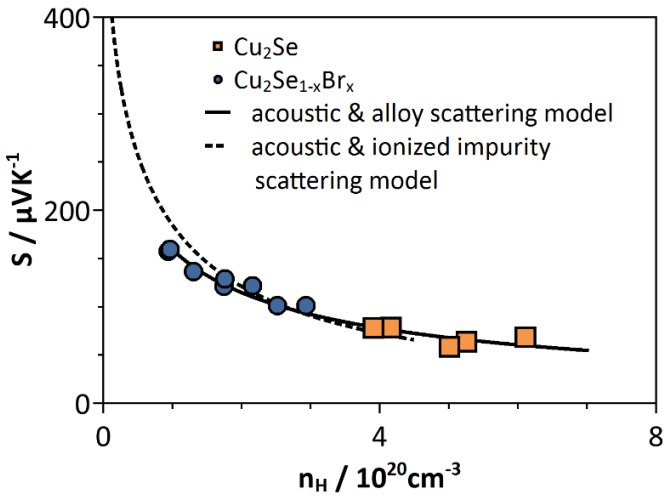

Figure 39. Pisarenko plot of undoped and doped copper selenide samples at 305 K. The black solid line represents the predicted curve for the combined acoustic and alloy scattering model and the black dashed line for the combined acoustic and ionized impurity scattering model. The overestimation of the Seebeck coefficient at low carrier concentrations rules out ionized impurity scattering.

Ionized impurity scattering is known to increase the Seebeck coefficient relative to that for acoustic phonon scattering.[178] At the lowest values of n_H measured in $Cu_2Se_{1-x}Br_x$, where ionized impurity scattering would have the greatest effect, the Seebeck curve generated by the combined acoustic phonon and ionized impurity scattering model predicts Seebeck coefficients up to 25 % greater than those actually observed. This systematic over-prediction of the Seebeck coefficient rules out the presence of ionized impurity scattering in this material. This is encouraging because it suggests that doping with something other than Br may not affect the mobility parameter possibly leading to larger quality factors and figures of merit, whereas ionized impurity scattering implies that any dopant would reduce μ_0 and therefore reduce the maximum potential zT. In this context an investigation of corresponding cation doped copper selenides would be very interesting as the reduction of the mobility could be much less pronounced here due to a smaller contribution of the cation sublattice to the valence band. To our knowledge cation doped copper selenide has never been successfully synthesized, which might be due to the different chemistry of copper compared to the other 3d elements. Our own doping attempts with nickel and zinc led to the formation of nickel and zinc selenide (NiAs structure) even for very low substitution grades. However, as Zunger has pointed out designing growth and synthesis conditions may be effective in obtaining the predicted high figure of merit without detrimental effects on the carrier mobility.[167]

7.6 Results of the SPB model at 550 K in $Cu_{2-y}Se_{1-x}Br_{x.}$

The SPB model was also applied to transport data on $Cu_{2-y}Se_{1-x}Br_x$ at 550 K. The results are shown in Figure 40. The effective masses of $Cu_{2-\delta}Se$ and of the Br-doped samples are increased relative to the values at 305 K. This increase in effective mass is responsible for the reduction in μ_0 in $Cu_{2-y}Se_{1-x}Br_x$ relative to $Cu_{2-\delta}Se$ at 550 K; μ_0 depends on $m^{*-5/2}$. The trend of the Hall mobility rising with carrier concentration in the Br-doped samples at 305 K is gone at 550 K. At the higher temperature, the Hall mobility decreases with Hall carrier concentration, as expected for acoustic phonon scattering. This is because the relaxation time for acoustic phonon relaxation time will be much shorter and will dominate the total scattering rate.

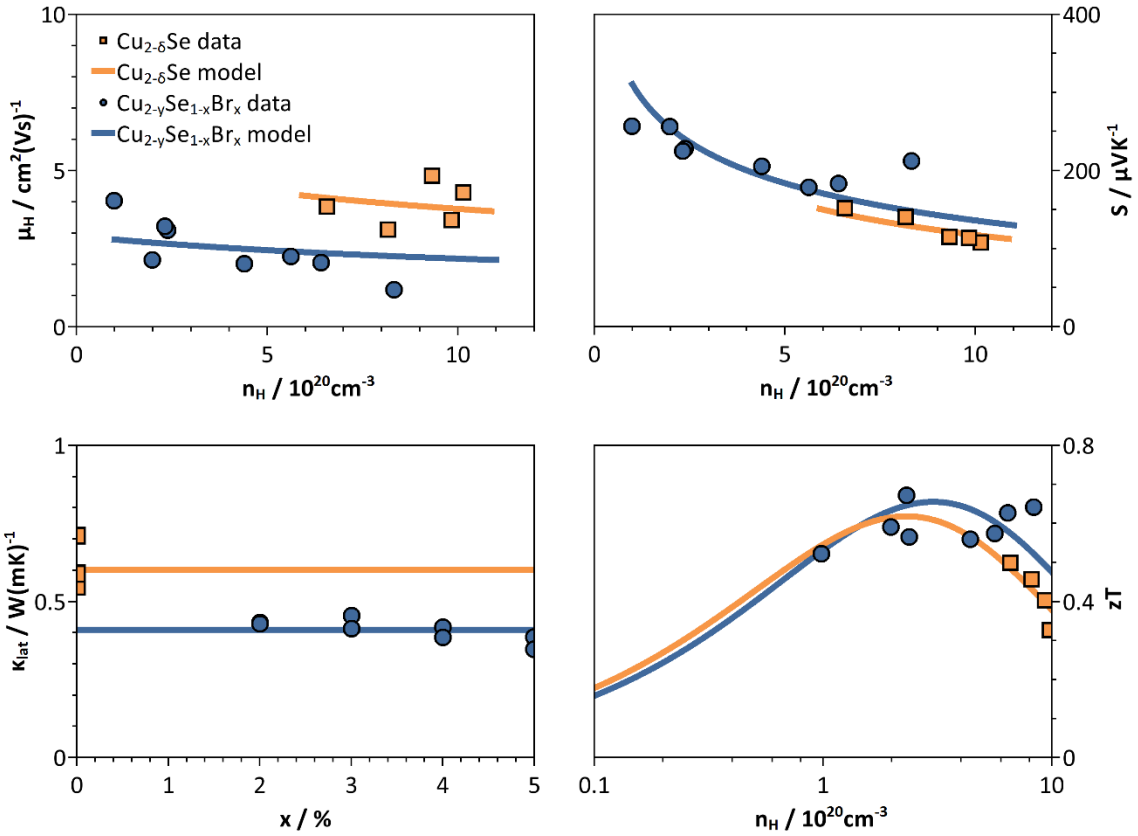

Figure 40. Results for the SPB model for $Cu_{2-\delta}Se$ and $Cu_{2-y}Se_{1-x}Br_x$ at 550 K with acoustic phonon scattering. Orange symbols denote $Cu_{2-\delta}Se$ and blue symbols denote $Cu_{2-y}Se_{1-x}Br_x$. In contrast to the results at 300 K the Hall mobility is not rising with the Hall carrier concentration for the bromine doped samples butt follows the expected trend for acoustic phonon scattering. This is in line with expectations as the relaxation time of acoustic phonon scattering depends on $T^{-3/2}$, whereas that for alloy scattering depends on $T^{-1/2}$. Therefore acoustic phonon scattering will dominate the total charge carrier relaxation time at high temperatures.

Table 5. SPB results for $Cu_{2-y}Se_{1-x}Br_x$ for different temperatures.

T / K	m* / m_e		μ_0 / $cm^2(Vs)^{-1}$		κ_{lat} / $W(mK)^{-1}$	
	$Cu_{2-\delta}Se$	$Cu_2Se_{1-x}Br_x$	$Cu_{2-\delta}Se$	$Cu_2Se_{1-x}Br_x$	$Cu_{2-\delta}Se$	$Cu_2Se_{1-x}Br_x$
305	2.1	2.1	34	17	0.16	0.20
350	2.3	2.4	23	12	0.31	0.30
400	3.0	2.5	12	9.1	1.3	0.68
450	2.7	3.2	11	5.5	1.0	0.58
500	3.1	3.8	8.1	3.9	0.61	0.42
550	3.5	4.3	6.1	3.3	0.60	0.41

The lower lattice thermal conductivity of the Br-doped samples (0.4 $W(Km)^{-1}$ versus 0.6 $W(Km)^{-1}$) gives them a slight edge over $Cu_{2-\delta}Se$ in maximum *zT* at 550 K, as shown by the predicted *zT* versus Hall carrier concentration curves in the bottom right plot of Figure 34. The SPB results for $Cu_{2-y}Se_{1-x}Br_x$ at all temperatures at which the SPB model was applied are shown in Table 5.

Chapter 8

Thermoelectric transport in Cu_7PSe_6

Thermoelectric transport in the Argyrodite Cu_7PSe_6 with high copper ionic mobility

The following section is in parts reprinted with permission from *J. Am. Chem. Soc.* **2014**, *136* (34), 12035-12040, Copyright 2014, American Chemical Society.

In this chapter we describe the synthesis and chemical characterization of Cu_7PSe_6 as well as the characterization of the thermoelectric transport properties, including Seebeck coefficient, electrical resistivity and thermal conductivity. Simultaneous measurements of electrical resistivity and Hall coefficients provided additional information on the electrical transport. Speed of sound measurements were performed in order to estimate the Debye temperature and the minimal lattice contribution to the thermal conductivity. The obtained data are compared with those of the closely related superionic thermoelectric material Cu_2Se in order to obtain a deeper understanding of the thermoelectric transport in ionic conductors within the phonon-liquid electron-crystal concept.

8.1 Chemical characterization.

The thermoelectric properties of Argyrodite-type compounds have not been investigated yet, and therefore phase purity of the measured samples is very important. Even small amounts of impurities can have a huge influence on the electronic and thermal properties of a material, for example through enhanced phonon scattering due to nano-sized impurities on grain boundaries.[179]

Samples of Cu_7PSe_6 were checked for phase purity via x-ray powder diffraction, and all reflections could be indexed to the simple-cubic (space group $P2_13$) Cu_7PSe_6 phase. No secondary phases were observed (Figure 41). With the unit cell parameter of a = 10.1057(8) Å, R_{wp} = 6.221 % and GoF = 1.268, the calculated data are in very good agreement with the lattice parameters reported by Kuhs et al., displaying a high purity of the prepared samples.[129] The isotropic thermal displacement parameters for copper were significantly higher than the parameters for selenium or phosphorous, which reflects the high mobility of the copper ions at room temperature.

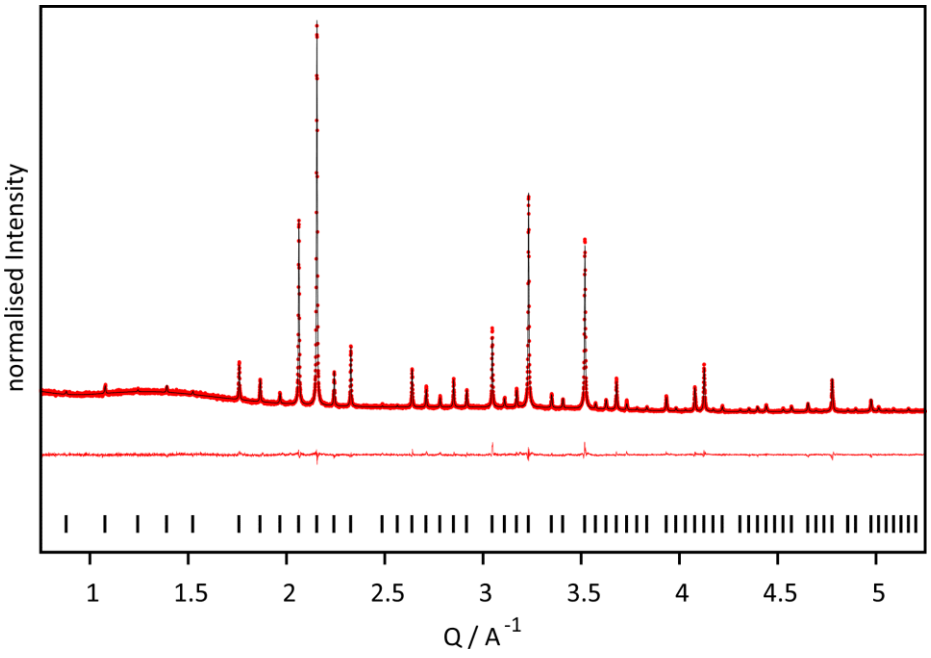

Figure 41. X-ray powder diffraction data for Cu_7PSe_6 (red dots), including profile fit (black solid line) and profile difference (red solid line) from the corresponding Rietveld refinement. All reflections could be indexed to the simple-cubic Cu_7PSe_6 phase with a = 10.1057(8) Å, R_{wp} = 6.221 % and GoF = 1.268. No side phases were observed using standard laboratory x-ray diffraction data.

TGA/DSC analysis shows an exothermic event at around 325 K, representing the phase transition from the partially-ordered, cubic primitive phase to the disordered face-centered-cubic phase. A small mass loss of about 0.5% could be observed at temperatures between 625 K and 875 K probably associated to sample decomposition; therefore the following measurements of the thermoelectric transport properties of Cu_7PSe_6 were carried out only up to 575 K.

8.2 Electronic transport in Cu_7PSe_6

The temperature dependent electrical resistivity of Cu_7PSe_6 is shown in Figure 42 (left). In the temperature region between 325 K and 425 K a strong decrease of the electrical resistivity was observed, which might be related to the phase transition from the partially cation ordered to the fully disordered high temperature phase with an increasing amount of mobile copper ions.[106,110] A rate-dependent hysteretic-like behavior was observed between the heating and cooling data. This is possibly due to the cation disordering during the heating process and the cation ordering during the cooling process, which seems to appear gradually over a certain temperature range. Above 425 K this hysteresis disappears and the resistivity decreases with increasing temperature, as expected for a semiconductor. In this case the temperature dependence of the conductivity is governed by an Arrhenius-like, thermally activated process across the band gap which can be described through $\sigma = A \exp(-E_a/(2k_BT))$, where σ is the electric conductivity, A is a constant, E_a is the activation energy and k_B the Boltzmann constant. An Arrhenius plot of the data from 425 K to 575 K is shown in the inset of Figure 42 (top). The calculated activation energy of 0.28 ± 0.01 eV is larger compared to the value of 0.17 eV for the high temperature modification and 0.22 eV for the low temperature modifications reported by Beeken et al.. [110] However, the activation energies are in good agreement since the absolute values are very small.

Temperature dependent Hall measurements were performed in order to obtain Hall carrier mobilities μ_H and Hall carrier concentrations n_H. The Hall carrier mobilities are very small and positive (Figure 42, bottom), which might be expected for an ionic conducting material. The huge degree of disorder in the structure, which is correlated to the ionic conducting nature of this compound, leads to trapping of electronic states at the Fermi energy.[180]

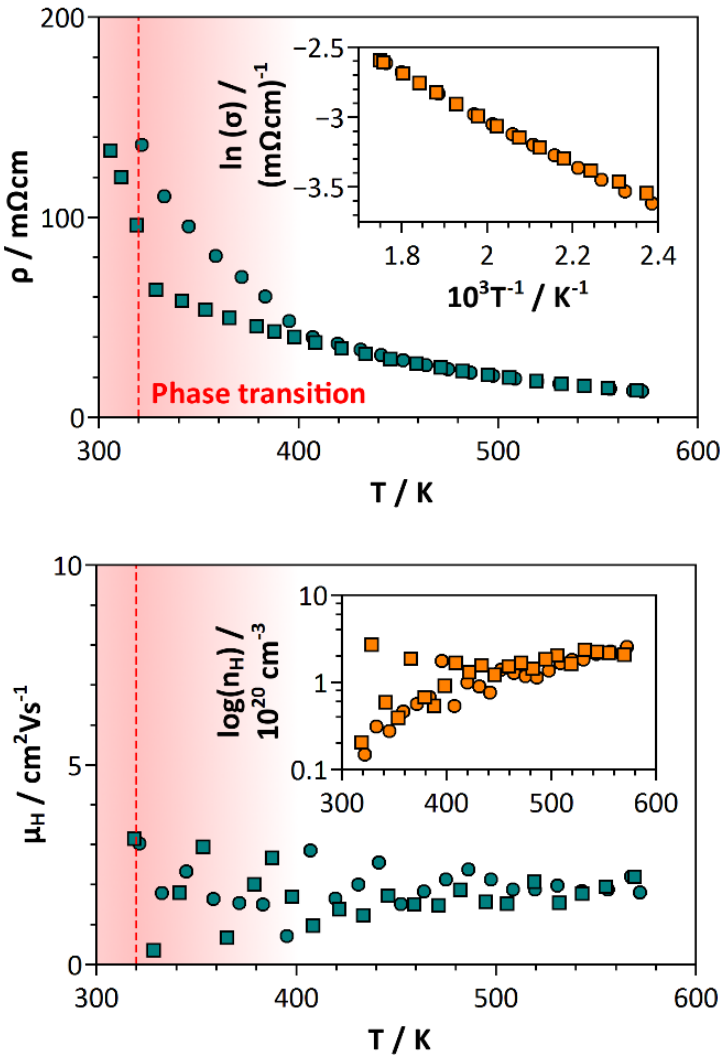

Figure 42. Electronic Transport in Cu_7PSe_6. Temperature dependences of the electrical resistivity ρ with Arrhenius plot (top), as well as Hall mobility μ_H and Hall carrier concentration n_H (bottom). Circles represent heating data, squares represent cooling data. A temperature range of 80 K is highlighted in red around the phase transition of Cu_7PSe_6 (red dashed line), where the rate dependent hysteretic like behavior can be observed in the resistivity data. Cu_7PSe_6 illustrates semiconducting behavior with an activation energy of 0.28 ± 0.01 eV, showing extrinsic hole transport as a result of intrinsic defects.

The positive values indicate that holes are the major charge carriers resulting from intrinsic defects, possibly induced by slight losses of selenium or phosphorous during the synthesis. Despite a slight decrease of n_H in the temperature range of the phase transition, which could be attributed to an additional increase of disorder, no significant temperature dependence could be observed for the Hall mobilities. As a consequence, no general statement can be made in relation to the scattering mechanism which is consistent with the resistivity and Hall data. Intrinsic conduction caused by thermal excitation of carriers is

not the main contributor in the observed temperature range, which would result in a peak Seebeck coefficient followed by decline. This observation is consistent with the calculated activation energy of 0.28 eV. The Hall carrier concentration n_H increases significantly with temperature (see inset Figure 3b.) in the temperature region of the structural phase transition from the partial cation disordered simple cubic phase to the fully cation-disordered phase, which is consistent with the decreasing activation energy.[106] After the phase transformation the carrier concentration increases slightly, which can be attributed to the contribution of a growing number of holes, resulting from intrinsic defects in the material.

The temperature dependence of the Seebeck coefficient is shown in Figure 4; the Seebeck coefficient increases from about +40 μV/K at room temperature to +175 μV/K at 575 K. This increase in the thermopower indicates extrinsic hole transport, which is consistent with the resistivity and Hall data. Intrinsic conduction caused by thermal excitation of carriers is not the main contributor in the observed temperature range, which would result in a peak Seebeck coefficient followed by decline. This observation is consistent with the calculated activation energy of 0.28 eV.

8.3 Thermal transport in Cu_7PSe_6

The total thermal conductivity of Cu_7PSe_6 increases slightly from 0.3 $W(Km)^{-1}$ to 0.4 $W(Km)^{-1}$ in the measured temperature range (see Figure 44, left). Cu_7PSe_6 has not yet been optimized with respect to the electronic properties, therefore, the electrical resistivities are still high compared to typical resistivities in related thermoelectric materials. Due to this, the electronic contribution to the total thermal conductivity is negligible at lower temperatures and below 10 % at higher temperatures.[98,99] The electronic contribution to the thermal conductivity has been estimated, using the Wiedemann-Franz law ($\kappa_{el} = LT\rho^{-1}$), with $L = 1.5 \cdot 10^{-8}$ $W\Omega K^{-2}$ for non-degenerate materials. The obtained values of the lattice contribution to the thermal conductivities are significantly lower than the lattice thermal conductivities of most of the state of the art thermoelectric materials, which usually are above 1 $W(Km)^{-1}$. Further, almost no temperature dependence of the thermal conductivity can be seen over the investigated temperature range.

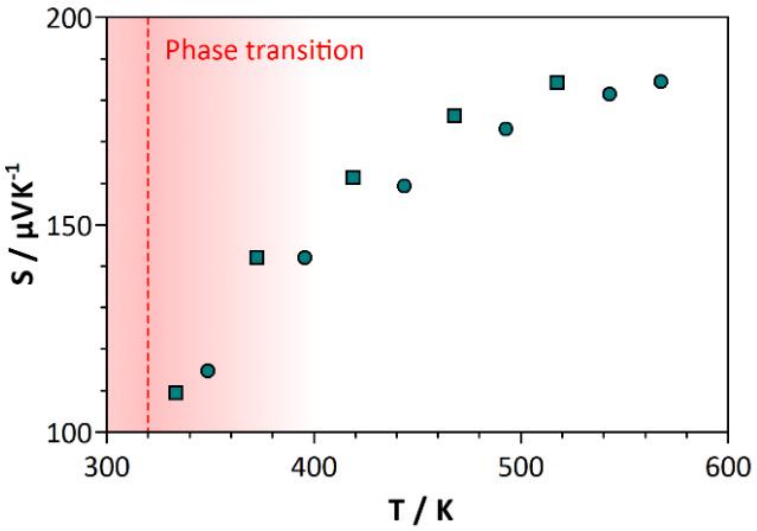

Figure 43. Temperature dependence of the Seebeck coefficient *S*. in Cu_7PSe_6 Circles represent heating data, squares represent cooling data. The Seebeck coefficient is positive and increases with temperature without reaching a maximum, which is consistent with the electrical resistivity and Hall data.

In contrast, most crystalline solid materials exhibit strong temperature dependence of their lattice thermal conductivity scattering mechanism.[47] However, highly disordered materials like glasses often show different temperature behaviors for the thermal conductivity.[42] For the Argyrodite Cu_7PSe_6, the ionic conducting character leads to a very high positional disorder resulting in very low, temperature independent lattice thermal conductivities. The melt-like behavior of the mobile Cu ions is responsible for a very short phonon mean free path, which results in κ_{lat} values in range of the glass limit. Furthermore, the low thermal conductivity can be attributed to the large unit cell of Cu_7PSe_6, composed of 56 atoms. This leads to a larger number of optical modes with low group velocities, which contribute less to the thermal conductivity.[42] The more complex structure might explain the lower lattice thermal conductivity of Cu_7PSe_6 compared to the related superionic conductor Cu_2Se, which has a lattice thermal conductivity around 0.4-0.6 $W(mK)^{-1}$ at high temperatures.[98]

Ultrasonic measurements of longitudinal and transverse sound velocities were performed at room temperature to estimate the Debye temperature Θ_D and the minimal thermal conductivity κ_{min}. The longitudinal and transversal speed of sounds were found to be v_L = 3580 ms^{-1} and v_t = 1870 ms^{-1}, respectively. With these, the Debye temperature was estimated to be 215 K via equation 3.6 and 3.7.[42,43] The low Debye temperature is typical for a material with a less rigid crystal structure. According to Cahill's formulation,

the glassy limit for the thermal conductivity κ_{min} can be estimated.[181] The high temperature limit for the minimum lattice thermal conductivity (equation 3.15) leads to a value of κ_{min} = 0.49 W(Km)$^{-1}$. Interestingly, the calculated value of κ_{min} is higher than the measured lattice thermal conductivity over the whole temperature range, which is in accordance with observations made on the superionic compounds Cu_2Se and Cu_2S.[98,99]

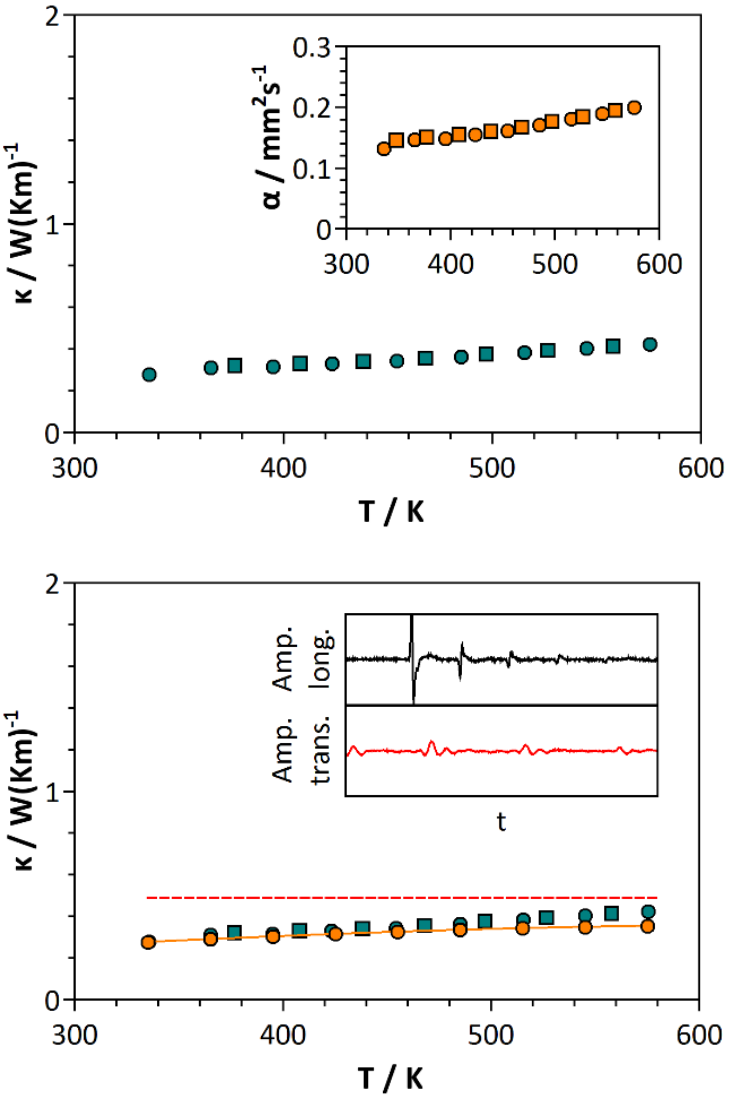

Figure 44. Thermal transport in in Cu_7PSe_6. The top picture shows the temperature dependences of the thermal conductivity κ with related thermal diffusivity α (inset). The cyan circles and squares represent the total thermal conductivity κ (heating and cooling). The bottom picture additionally shows the lattice thermal conductivity κ_{lat} as orange circles, which has been estimated from the Wiedemann-Franz law. The glassy limit of the lattice thermal conductivity κ_{min} has been determined by Cahill's formulation and is represented by the red dotted line which lies above the measured values for κ. Ultrasonic measurements of longitudinal and transverse sound velocities are shown in the inset.

Cahill's formulation of the glass limit employs a summation over all sound modes with their associated speeds of sound. Removing a fraction of the heat propagating modes will lead to a lower value of κ_{min}. For instance, in order to bring the κ_{min} calculated here for Cu_7PSe_6 in the range of the measured value of κ_{lat}, half of the shear modes would have to be removed. [99] Some examples for materials with thermal conductivities below the predicted minimal limit are known in disordered layered materials, which is attributed to a localization of lattice vibrations, making them unable to contribute to heat conduction.[182] In other words, these low lattice thermal conductivities may be due to shear modes, which do not propagate through the lattice. Therefore Cu_7PSe_6 might show lattice thermal transport behavior close to a real liquid, where shear modes do not propagate at all. The assumption of an influence of the high-mobility cations in superionic compounds on transverse lattice modes can be supported by the comparison of the longitudinal and transverse speed of sound data of Cu_7PSe_6 and Cu_2Se.

The longitudinal speed of sound of Cu_7PSe_6 (v_L=3580 ms^{-1}) is a little higher compared to Cu_2Se with v_L=3350 ms^{-1}, while the transverse speed of sound is significantly lower (v_t=2320 ms^{-1} for Cu_2Se and v_t=1870 ms^{-1} for Cu_7PSe_6). While both speed of sound measurements were performed at room temperature, Cu_7PSe_6 is ion-conducting during the measurement, whereas Cu_2Se is superionic only above 400 K. [98] The much lower transverse speed of sound is an indication for a significant softening of shear modes due to the melt-like copper sub lattice. It has to be taken in consideration that Cahill's formulation is based on assumptions which might not hold for superionic materials. Further investigations will be performed to provide a more detailed understanding of the extraordinarily low thermal conductivities in Argyrodite-type ionic conducting compounds.

8.4 Figure of merit.

The maximum *zT* of 0.35 at 575 K is very promising (Figure 6), as exclusively a nominally valence precise compound was studied in this work. Similar to the related binary superionic compounds Cu_2Se and Cu_2S, the power factor needs to be optimized via substitution in order to obtain higher values for the figure of merit in Cu_7PSe_6 or related compounds.[12,13]

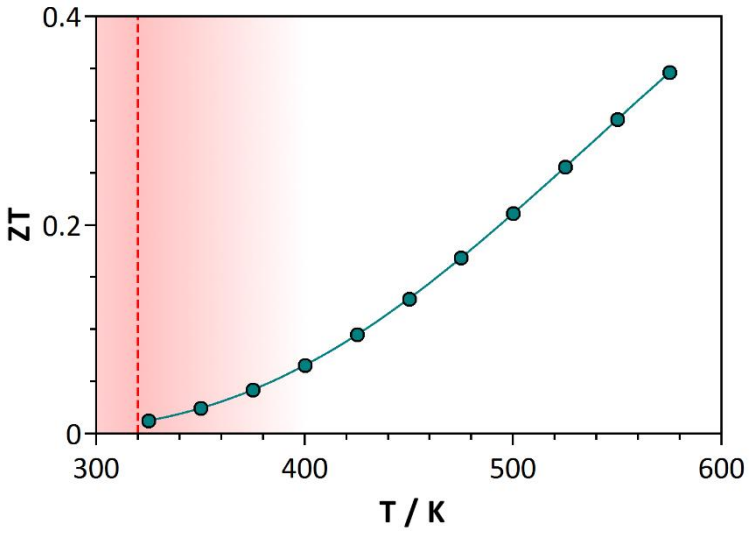

Figure 45. Temperature dependence of the dimensionless figure of merit *zT*.

Chapter 9

Thermoelectric transport in $(Cu,Ag)_7PSe_6$

Thermoelectric properties of the $(Cu,Ag)_7PSe_6$ series of solid solutions

Building on the promising thermoelectric properties of Cu_7PSe_6, the series of solid solutions $(Cu,Ag)_7PSe_6$ is regarded, in order to investigate the effects of structural aspects on the thermoelectric transport in PLEC thermoelectrics. Besides Cu_7PSe_6, which has been investigated in the previous chapter, $Cu_6Ag_1PSe_6$, $Cu_4Ag_3PSe_6$, $Cu_2Ag_5PSe_6$ and Ag_7PSe_6 have been synthesized. Here, the influence of the substitution of copper and silver on the thermoelectric properties can be easily investigated, which is much more difficult in binary systems.

In particular, the effect of the mobile cation substitution on the room-temperature thermal conductivity can be investigated using the Callaway model, as all investigated samples have the same structure at room-temperature.

9.1 Chemical characterization

Samples of $(AgCu)_7PSe_6$ were checked for phase purity via x-ray powder diffraction, and all reflections could be indexed to the simple-cubic Argyrodite phase of Cu_7PSe_6 (space group $P2_13$). No secondary phases were observed. Rietveld refinements against standard laboratory x-ray powder diffraction data with the published structure models do not provide reasonable information on positions or site occupancies with respect to the substitution of copper versus silver due to the large isotropic thermal displacement parameters for copper and silver in the simple-cubic phase. However, lattice parameters have been derived from Pawley-fits (Figure 46 - Figure 49) and are summed up in Table 6. The phases exhibit a linear dependence of the lattice parameters on the composition (Vegard-like behavior) indicating a direct substitution of copper versus silver without any reconstruction processes (Figure 50). TGA/DSC analysis was used to examine the phase transition temperatures from the partially-ordered, cubic primitive phase to the disordered face-centered-cubic phase which are represented by exothermic events. As it was already observed for Cu_7PSe_6, very small mass losses of less than 0.5 % could be observed at temperatures between 625 K and 875 K, probably associated to sample decomposition.

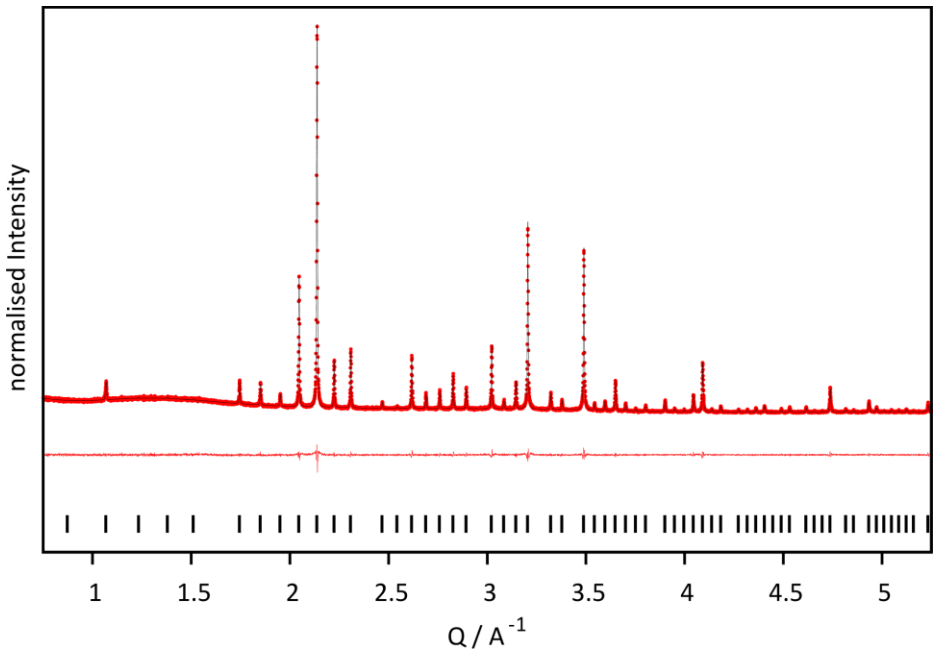

Figure 46. X-ray powder diffraction data for Cu_6AgPSe_6 (red dots), including profile fit (black solid line) and profile difference (red solid line) from the corresponding Pawley fit. All reflections could be indexed to the simple-cubic Cu_7PSe_6 phase with a = 10.1900(0) Å, R_{wp} = 5.673 % and GoF = 1.174.

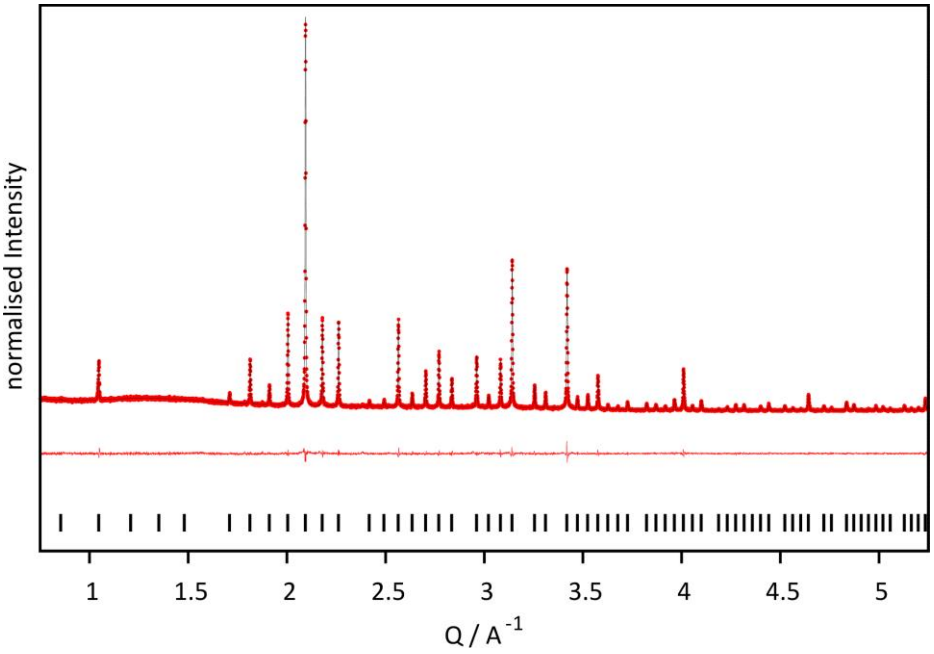

Figure 47. X-ray powder diffraction data for $Cu_4Ag_3PSe_6$ (red dots), including profile fit (black solid line) and profile difference (red solid line) from the corresponding Pawley fit. All reflections could be indexed to the simple-cubic Cu_7PSe_6 phase with a = 10.396(6) Å, R_{wp} = 6.189 % and GoF = 1.300.

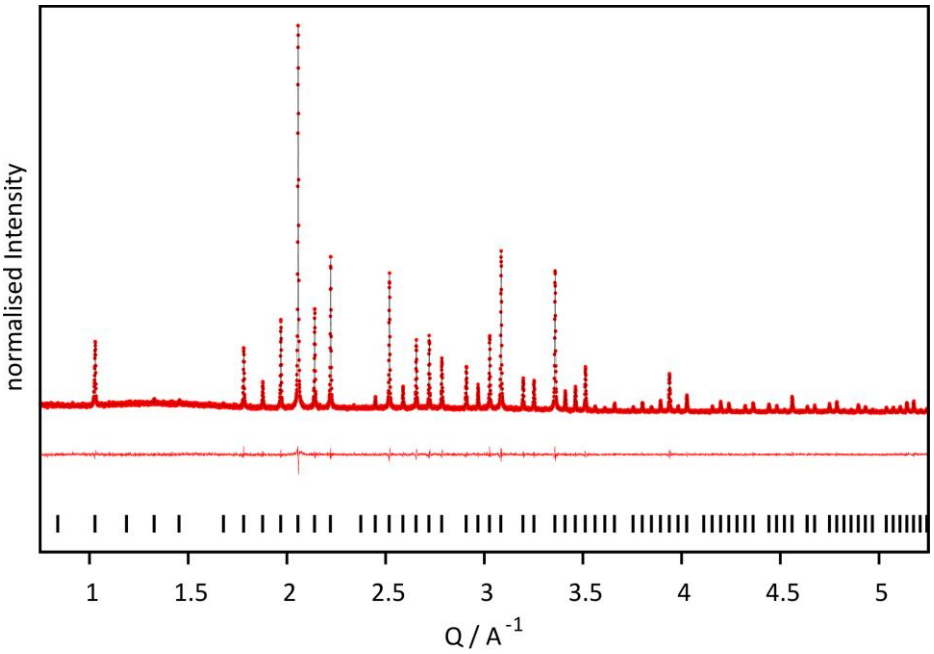

Figure 48. X-ray powder diffraction data for $Cu_2Ag_5PSe_6$ (red dots), including profile fit (black solid line) and profile difference (red solid line) from the corresponding Pawley fit. All reflections could be indexed to the simple-cubic Cu_7PSe_6 phase with a = 10.585(5) Å, R_{wp} = 7.683 % and GoF = 1.697.

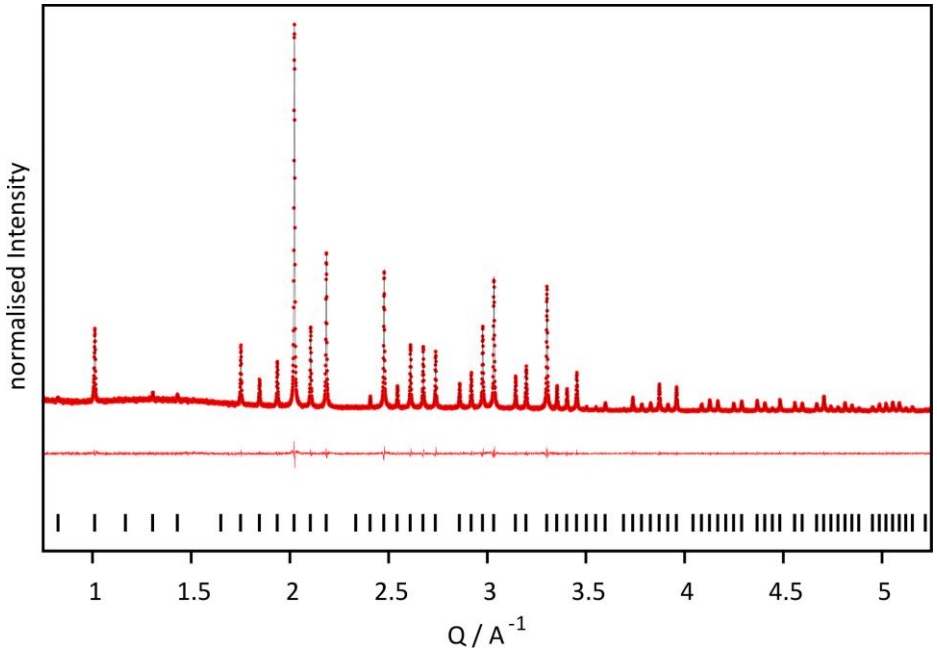

Figure 49. X-ray powder diffraction data for Ag_7PSe_6 (red dots), including profile fit (black solid line) and profile difference (red solid line) from the corresponding Pawley fit. All reflections could be indexed to the simple-cubic Cu_7PSe_6 phase with a = 10.767(5) Å, R_{wp} = 6.476 % and GoF = 1.402.

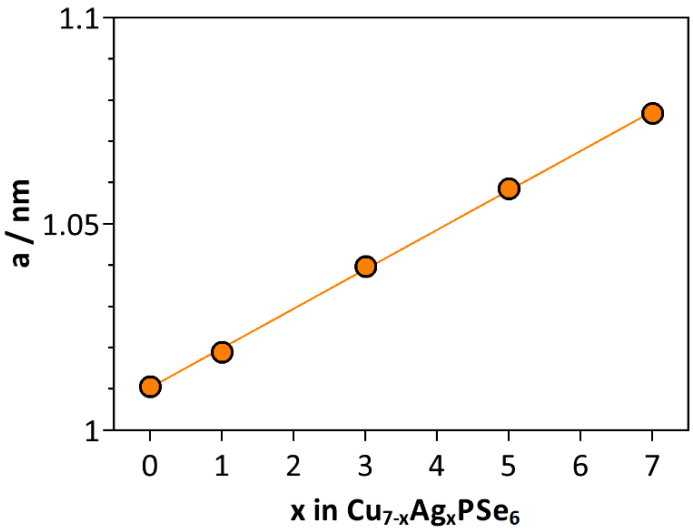

Figure 50. Lattice parameters versus composition for $Cu_{7-x}Ag_xPSe_6$, showing a linear dependence (Vegard-like). The error bars are smaller than the symbols.

Table 6. Lattice parameters for $Cu_{7-x}Ag_xPSe_6$ derived from Pawley fits, as well as phase transition temperatures from the cubic primitive room temperature phase to the face-centered-cubic high temperature phase, which is increasing with increasing *x*.

x in $Cu_{7-x}Ag_xPSe_6$	Lattice parameter / Å	Phase transition temperature / K
0	10.105(7)	340
1	10.190(0)	350
3	10.396(6)	380
5	10.585(5)	410
7	10.767(5)	450

9.2 Electronic transport in $(AgCu)_7PSe_6$

In summary all silver containing samples show drastically increasing electrical resistivities with increasing silver content which makes the determination of Hall coefficients very difficult due to high contact resistances. Therefore only Seebeck coefficients and electrical resistivities are regarded. The temperature dependent electrical resistivity of Cu_6AgPSe_6 is shown in Figure 51 (top). As already found for Cu_7PSe_6, a decrease of the electrical resistivity can be observed at temperatures close to the phase transition at 350 K. However the rate-dependent hysteretic-like behavior between the heating and cooling data at the phase transition cannot be observed here.

In contrast to Cu_7PSe_6, the electrical resistivity of Cu_6AgPSe_6 reaches a minimum value of about 30 mΩcm at 520 K and increase again at higher temperatures. On cooling the resistivity does not go back to the minimum but increases continuously at higher resistivity values. On a second run with the same pellet and conditions of measurement the low resistivity values are not observed again and both heating and cooling curve follow the cooling curve of the first resistivity measurement. A similar behavior has been found for Cu_7PSe_6 when heating to temperatures above 600 K which should be attributed to partial degradation and slight losses of Selenium or Phosphorous during the measurement. Although there are no signs of decomposition visible on the pellets after the measurement this decomposition leads to changes in the electronic transport properties.

The temperature dependence of the Seebeck coefficient is shown in Figure 51 (bottom); the Seebeck coefficient increases from about ± 0 µV/K at room temperature to +175 µV/K at 600 K indicating extrinsic hole transport. In contrast to the resistivity measurement, signs of decomposition cannot be observed up to 600 K within two Seebeck measurement runs on the same pellet. Although both Seebeck measurements were performed under vacuum, the pellets are fully covered by grafoil and the two heating blocks which prevents evaporation from the pellet surface and therefore hinders decomposition.

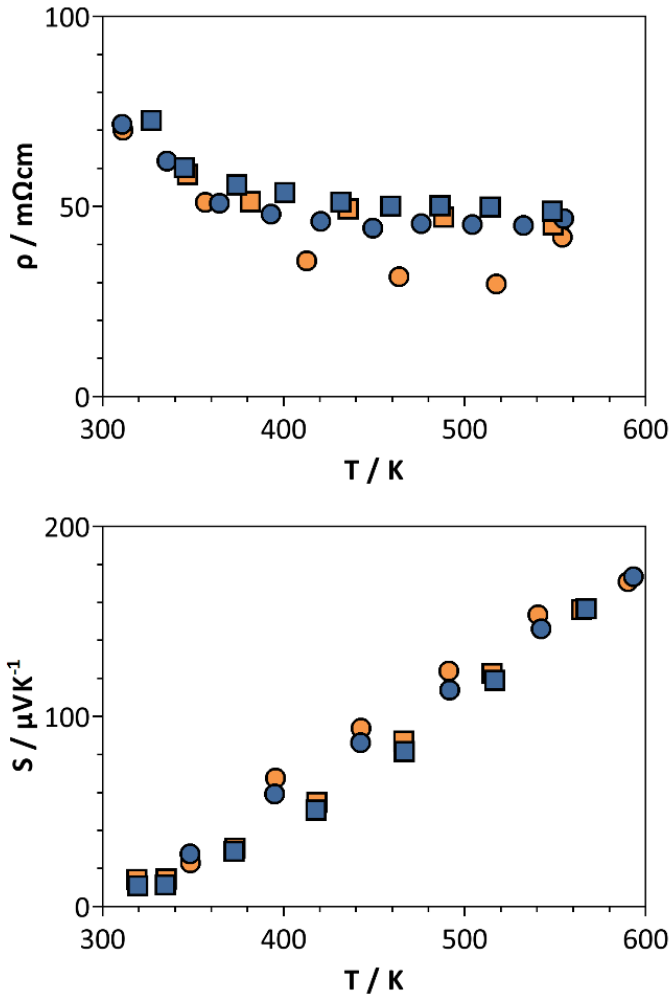

Figure 51. Electronic transport in Cu_6AgPSe_6. Temperature dependences of the electrical resistivity ρ (top) and Seebeck coefficient (bottom). Circles represent heating data, squares represent cooling data. Orange data represents the first measurement, blue data represents the second measurement on the same pellet. A minimum of the electrical resistivity can only be observed at the first heating run indicating a decomposition of the compound at temperatures above 520 K. The Seebeck coefficient is positive and increases with temperature without reaching a maximum. Signs of decomposition cannot be observed up to 600 K.

The temperature dependent electrical resistivity of $Cu_4Ag_3PSe_6$ is shown in Figure 52 (top). Again, the electrical resistivity shows a decreasing trend with temperature. However the absolute values are much higher in Cu_6AgPSe_6 compared to Cu_7PSe_6, leading to much lower charge carrier concentrations. In addition both electrons and holes seem to have a significant contribution to the electrical transport properties as the Seebeck coefficient is very hard to determine. Figure 52 (bottom) shows three different Seebeck measurements on three pellets which were pressed from the $Cu_4Ag_3PSe_6$ powder of the same ampoule. Still, the three pellets show extremely different temperature behavior of the Seebeck coefficient.

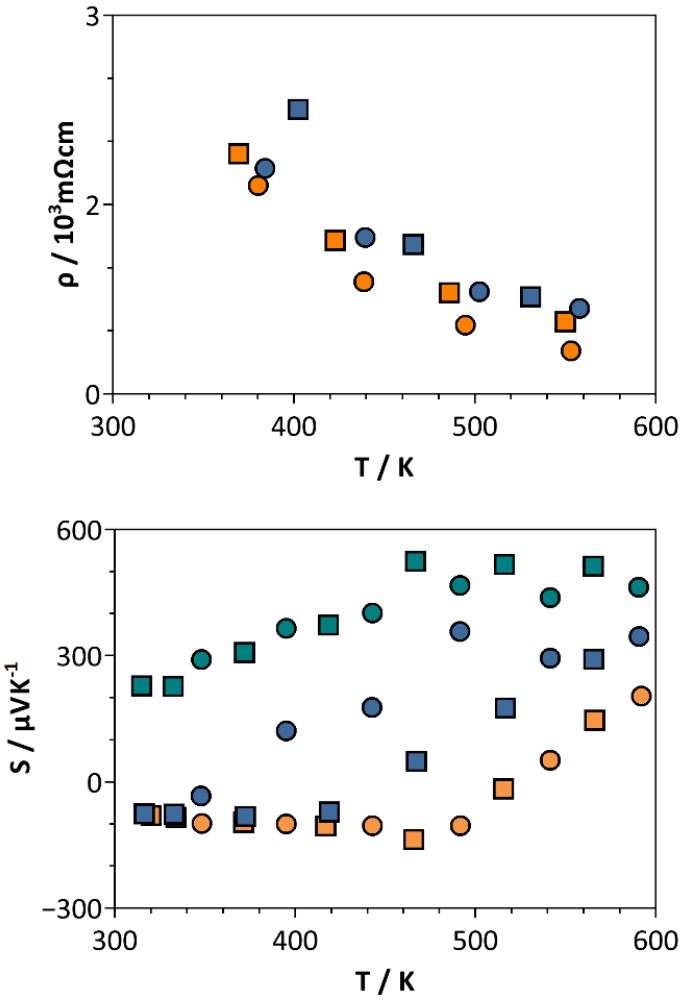

Figure 52. Electronic transport in $Cu_4Ag_3PSe_6$ Temperature dependences of the electrical resistivity ρ (left) and Seebeck coefficient (right). Circles represent heating data, squares represent cooling data. Different colors represent data of different pellets from the same compound. The absolute values of the electrical resistivity are much higher than the resistivities measured for Cu_7PSe_6, Cu_6AgPSe_6. The temperature dependence of the Seebeck coefficient cannot be determined reproducible, as both electrons and holes in small concentrations are present in the material.

Two of the pellets have negative Seebeck coefficients at room temperature indicating that electrons dominate the electronic transport. With increasing temperature the Seebeck coefficient increases for all three pellets. At high temperatures above the phase transition the Seebeck coefficient of all samples is positive.

Very similar behavior can be observed for the Seebeck coefficient of $Cu_2Ag_5PSe_6$. Here, the determination of electrical resistivity using the van der Pauw method is very difficult due to the large contact resistances of the 4 probes, making quantitative results very hard to obtain. This explains the huge discrepancy between heating in cooling data in Figure 53 (left). However, the absolute values of the electrical resistivity are very high.

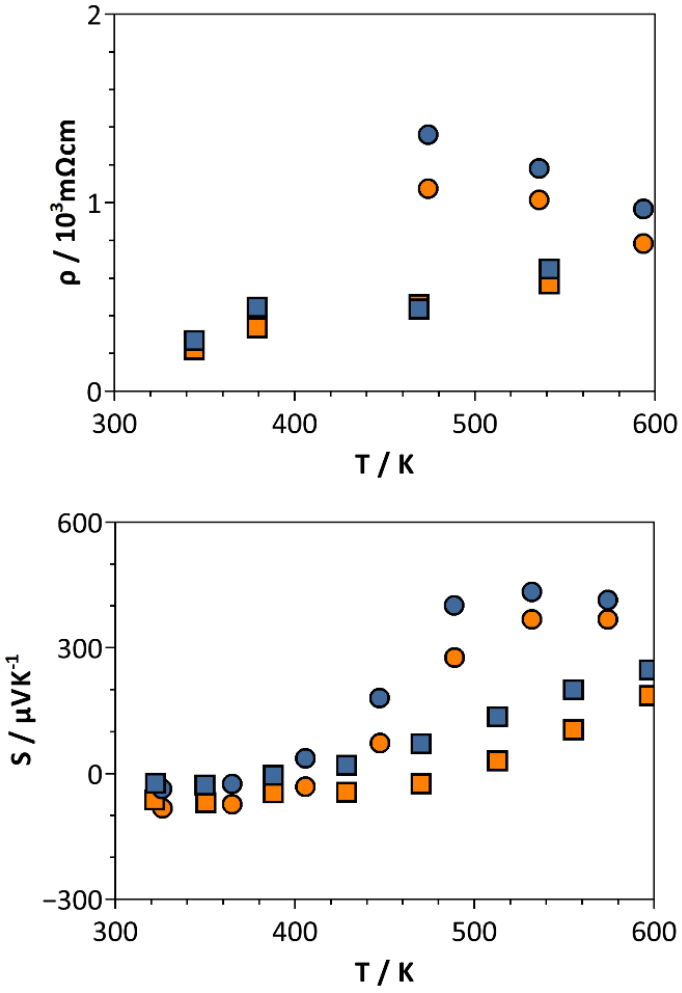

Figure 53. Electronic transport in $Cu_2Ag_5PSe_6$ Temperature dependences of the electrical resistivity ρ (left) and Seebeck coefficient (right). Circles represent heating data, squares represent cooling data. Different colors represent data of different pellets from the same compound. The temperature dependence of the Seebeck coefficient cannot be determined reproducible, as both electrons and holes in small concentrations are present in the material.

This applies also to Ag_7PSe_6 where the measured electrical resistivities are even higher (Figure 54, left). The most striking difference to the copper containing compositions is a negative Seebeck coefficient over the whole temperature range (Figure 54, right). This transition from p-type transport in Cu_7PSe_6 to n-type transport in Ag_7PSe_6 in combination with the overall low charge carrier concentrations are responsible for the huge difficulty in obtaining reproducible electronic transport data. In addition, Hall mobilities and Hall carrier concentrations were calculated from Hall coefficients. Similar to the electrical resistivity data Hall data are not considered to be significant with respect to the absolute values due to the large contact resistances.

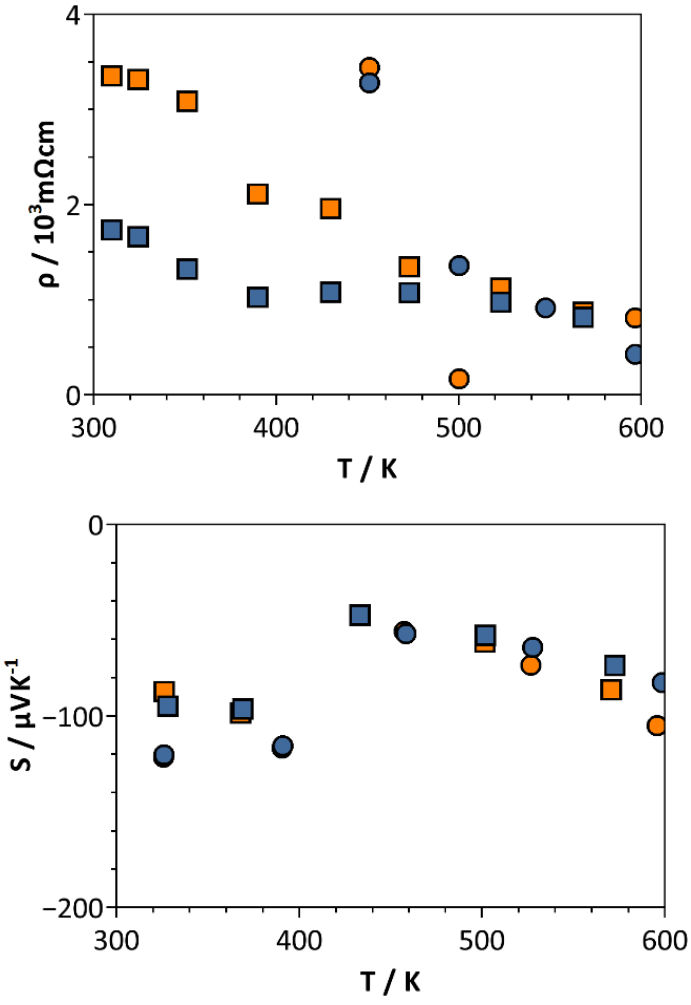

Figure 54. Electronic transport in Ag_7PSe_6 Temperature dependences of the electrical resistivity ρ (left) and Seebeck coefficient (right). Circles represent heating data, squares represent cooling data. Different colors represent data of different pellets from the same compound. Ag_7PSe_6 is the only representative of the solid solution series with a negative Seebeck coefficient over the whole temperature range.

Generally, Hall carrier concentrations show an overall decreasing trend with increasing silver content from roughly 10^{20} cm^{-3} for Cu_7PSe_6 to 10^{17} cm^{-3} for Ag_7PSe_6, which is consistent with the resistivity data.

9.3 Thermal transport in $(AgCu)_7PSe_6$

The temperature dependences of the total thermal conductivity κ for Cu_6AgPSe_6, $Cu_4Ag_3PSe_6$, $Cu_2Ag_5PSe_6$ and Ag_7PSe_6 are shown in Figure 55. Similar to Cu_7PSe_6, the total thermal conductivity of the synthesized samples show a slightly increasing trend in the investigated temperature range. As the electrical resistivities of the silver containing samples are even higher than the resistivity of Cu_7PSe_6, the total thermal conductivity shown in Figure 55 represents the lattice thermal conductivity in good approximation as the electronic contributions to the thermal conductivity are close to zero.

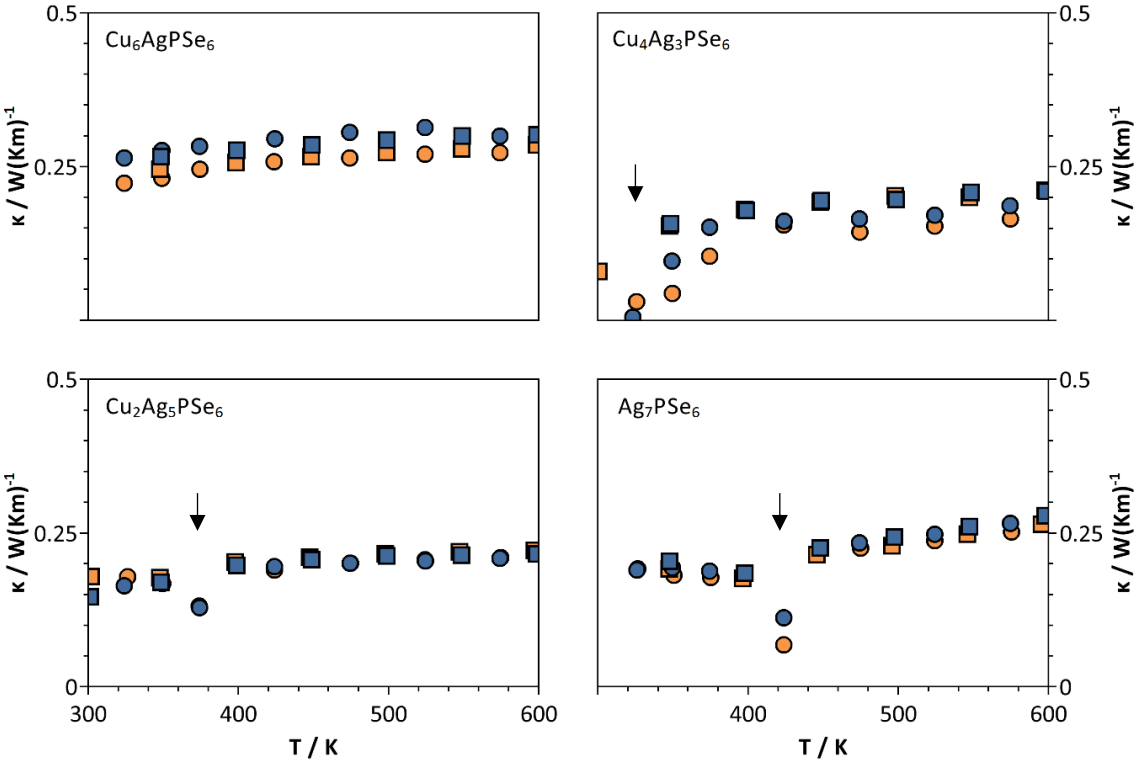

Figure 55. Thermal transport in $(Cu,Ag)_7PSe_6$. Circles represent heating data, squares represent cooling data. Different colors represent data of different pellets from the same compound. The phase transition from the room temperature phase to the high temperature phase shifts to higher temperatures with increasing silver content, represented by the minimum in the thermal conductivity. The small black arrows mark the temperature of the phase transition which increases with increasing temperature.

Every sample exhibits a slightly increasing temperature dependence which also has been observed for Cu_7PSe_6 and is typical for glasslike materials due to an increase in specific heat (see section 3.3).

At the temperature of the phase transition, a minimum of the thermal conductivity can be observed which is due to λ-anomaly in the specific heat which is typical for a second order phase transition and often observed in superionic compounds.[183] The absolute values of the thermal conductivity in the silver containing samples are even lower than the thermal conductivity of Cu_7PSe_6. This is attributed to the lager atomic mass and the softer bonding character of silver compared to the lighter homologue. Besides the average molar mass of the cations, the substitution leads to additional disorder creating mass and strain contrast, both acting as phonon scattering centers.[57] As a consequence the lattice thermal conductivity decreases with increasing disorder on the cation site and therefore the lowest lattice thermal conductivity should be found at 50 % substitution.

Figure 56 shows the lattice thermal conductivity of the complete solid solution series $Cu_{7-x}Ag_xPSe_6$ with x = 0-7 versus composition for several temperatures. As expected, a maximum reduction of the lattice thermal conductivity up to about 30% can be observed as a result of increased disorder due to the cation substitution. This trend appears most pronounced at high temperatures where the cations are fully disordered. In order to differentiate between mass and strain contrast in the disordered system, κ_{lat} can be calculated using the Callaway model introduced in section 3.6.

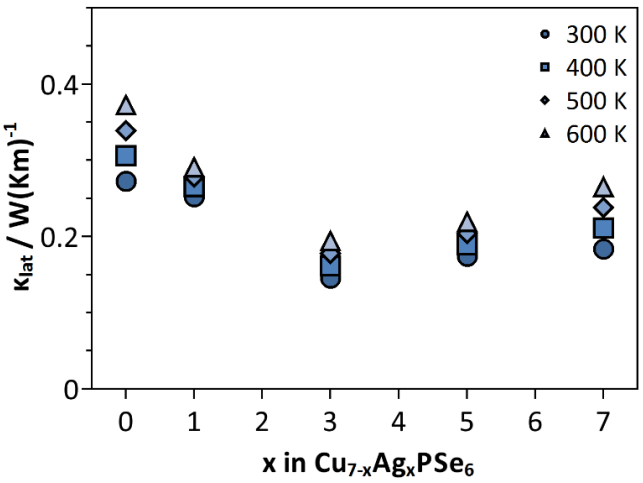

Figure 56. Lattice thermal conductivity of $Cu_{7-x}Ag_xPSe_6$ versus x for several temperatures. A maximum reduction of the lattice thermal conductivity up to about 30 % can be observed as a result of increased disorder due to the cation substitution.

The measured thermal conductivities of Cu_7PSe_6 and Ag_7PSe_6 were used to as κ_{lat}^{pure}. As only speed of sound data of Cu_7PSe_6 at room temperature was available, average speed of sound and Debye temperature of Cu_7PSe_6 had to be used for Ag_7PSe_6 and all intermediate compositions. The lattice thermal conductivities at room temperature compared to the lattice thermal conductivities obtained from the Callaway model are shown in Figure 57. Here, the modeled lattice thermal conductivity with mass contrast only (grey line) and with mass and strain contrast (orange line) are shown. A fitting parameter of $\epsilon = 30$ has been used for weighing the strain contrast which leads to a reasonable fit and is similar to fitting parameters which have been used on similar chalcogenide compounds.[56] The good agreement of the fit with the measured data indicates that the Callaway model can be used for modeling the reduction of the lattice thermal conductivity due to the substitution of mobile cations in superionic compounds.

However, it has to be taken in consideration that the Callaway model is based on assumptions which might not hold for the investigated superionic materials. First, Callaway's model is only valid if Umklapp scattering and impurity scattering dominate phonon scattering which is not given in the investigated solid solution series. As mentioned before, a domination of Umklapp scattering would result in a *1/T* temperature dependence of the lattice thermal conductivity.

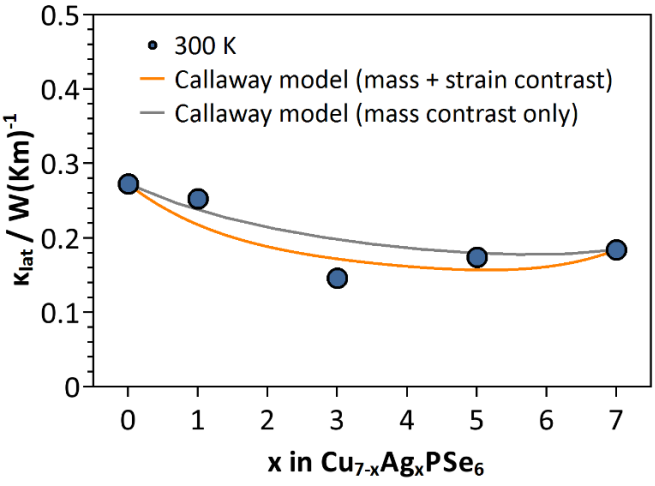

Figure 57. Callaway model in $Cu_{7-x}Ag_xPSe_6$. Measured lattice thermal conductivity at room temperature and modeled lattice thermal conductivities of the solid solution series $Cu_{7-x}Ag_xPSe_6$ with x = 0-7 versus composition. The gray line represents modeled data with mass contrast only ($\epsilon = 0$), the orange line represents modeled data with mass and strain contrast ($\epsilon = 30$).

Here, the mean free path is limited by geometrical effects due to the highly disordered nature of the structure with mobile cations leading to almost temperature independent lattice thermal conductivities. Second, there should be an influence of the phase transition from the simple-cubic room temperature phase to the face-centered-cubic high temperature phase which represents the melting of the cation lattice. This phase transition takes place at temperatures close to room temperature for Cu_7PSe_6 and shifts to higher temperatures with increasing silver content.

Therefore the room temperature lattice thermal conductivity of Cu_7PSe_6 might already be reduced as a result of additional disorder due to the melting cation lattice. The assumption that the melting of the cation lattice in Cu_7PSe_6 already starts at room temperature is supported by the hysteresis between heating and cooling data in the electrical resistivity measurement of Cu_7PSe_6 (Figure 42) between 300 and 400 K.

Chapter 10

Thermoelectric transport in Ag_8SiSe_6

Thermoelectric properties of the Argyrodite Ag_8SiSe_6

We have synthesized the silver ion conducting Argyrodite Ag_8SiSe_6 and characterized the thermoelectric transport properties. Initially, Ag_8SiSe_6 was prepared in order to investigate the influence of the amount of mobile cations per formula unit on the thermoelectric properties by comparing the thermoelectric properties with Ag_7PSe_6. In fact, both materials show very different thermoelectric properties. As shown in the prvious chapter (chapter 9), Ag_7PSe_6 shows an extremely high electrical resistivity without any potential for thermoelectric application. In contrast, Ag_8SiSe_6 shows extremely high figure of merits at low temperatures due to an extraordinarily low thermal conductivity, which arises from a high structural disorder and a liquid-like behavior of the material. Furthermore we have demonstrated that Ag_8SiSe_6 has the potential to reach even higher figure of merits at low temperature, if the intrinsic heavily doped character can be altered.

Therefore, the thermoelectric properties of Ag_8SiSe_6 are potentially competitive with bismuth telluride, which is the currently best thermoelectric material, when the temperature of the heat source is moderate.

10.1 Chemical characterization.

X-ray powder diffraction data of the synthesized samples are shown in Figure 58. Position and intensity of the main reflections fit well to the simple cubic Argyrodite phase. However between 2Θ = 30° and 50° a large amount of additional reflections can be observed, indicating that the symmetry of Ag_8SiSe_6 is much lower than the symmetry of the room temperature phase in Cu_7PSe_6. Due to the large number of additional reflections solving the structure with x-ray powder diffraction data is not possible. Regarding only the major reflections, which are marked with (#) in the right image of Figure 58 and using the simple cubic room temperature structure of Cu_7PSe_6, Pawley fits were used in order to obtain the unit cell size of a hypothetic cubic cell. The Pawley fit is shown in Figure 59 and leads to a unit cell size of 10.90 Å, which is reasonable as the unit cell size is slightly larger than the unit cell size of Ag_7PSe_6 with 10.77 Å, which contains one silver cation less. In order to solve the room temperature structure of Ag_8SiSe_6, single crystal x-ray diffraction data would be needed. Unfortunately the size and quality of the synthesized crystals was not high enough to measure single crystal x-ray diffraction.

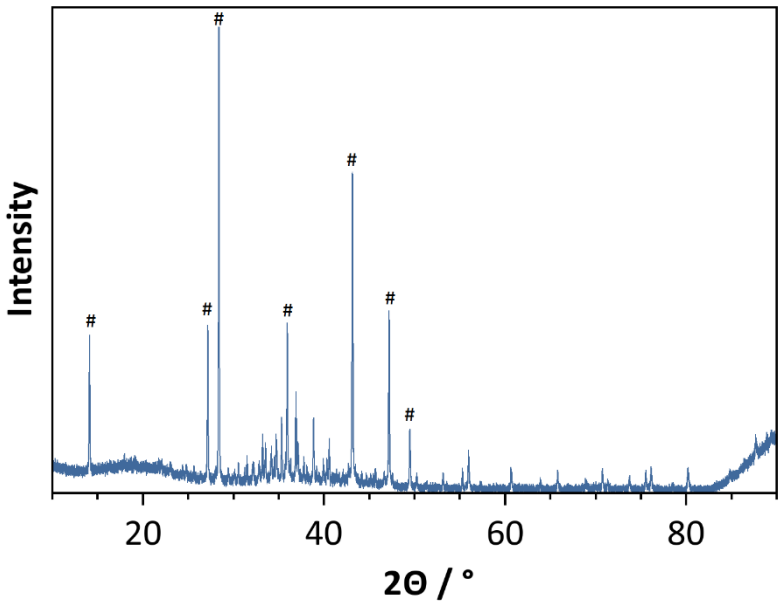

Figure 58. Room temperature x-ray powder diffraction data of Ag_8SiSe_6. The main reflections, which are marked with (#) fit well to the simple cubic cell with a = 10.89 Å. No reflections of starting materials or possible impurity phases could be observed.

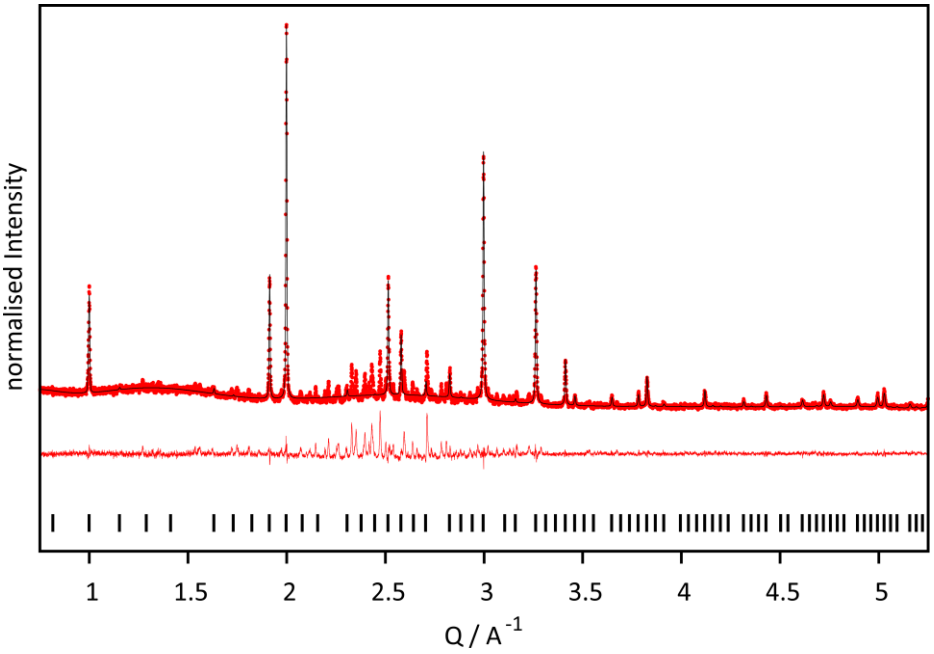

Figure 59. X-ray powder diffraction data for Ag_8SiSe_6 (red dots), including profile fit (black solid line) and profile difference (red solid line) from the corresponding Pawley fit. The major reflections could be indexed to the simple-cubic Cu_7PSe_6 phase with a = 10.8978(0) Å, R_{wp} = 13.3 % and GoF = 1.9.

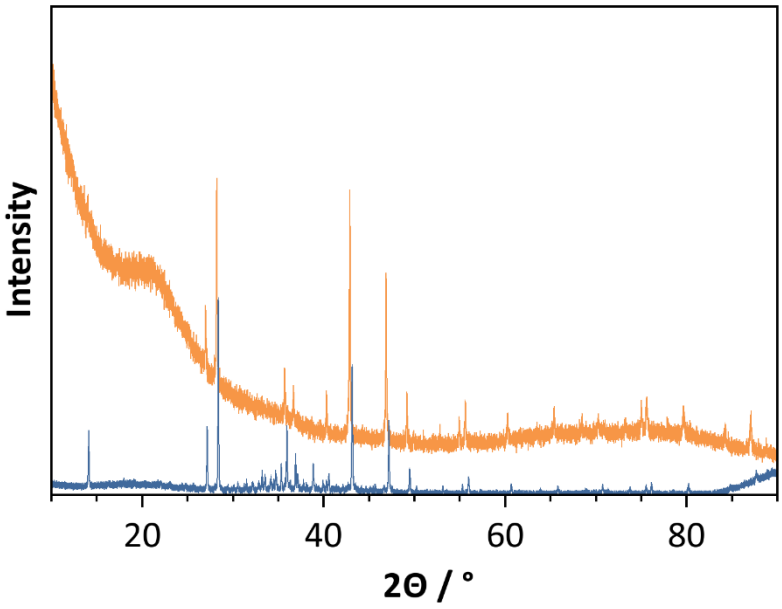

Figure 60. High temperature x-ray powder diffraction data of Ag_8SiSe_6 (orange). The blue curve represent s x-ray diffraction data at 300K, the orange curve represents x-ray diffraction data at 410 K. The additional reflections between 2Θ = 30° and 50° are only observed at room temperature, indicating that the room temperature phase has a much more complex structure.

As it was not possible to solve the room temperature structure of Ag_8SiSe_6 and check for phase purity, high temperature x-ray powder diffraction data was measured in order to proof that the additional reflections are the result of a low symmetry of the room temperature phase and no impurity phases are present. The high temperature x-ray diffraction data measured at 410 K is shown in Figure 60. As expected, at high temperatures, only the reflections of the simple cubic Argyrodite phase can be observed, indicating that a reduced symmetry of the room temperature phase in Ag_8SiSe_6 is responsible for the additional reflections in the room temperature x-ray powder diffraction data.

10.2 Electronic transport in Ag_8SiSe_6

The temperature dependent electrical resistivity of Ag_8SiSe_6 is shown in Figure 61 (top, left) and the temperature dependence of the Seebeck coefficient is shown in Figure 61 (top, right). In the temperature region between 300 K and 380 K a decrease of the electrical resistivity was observed, as expected for a semiconductor. At 390 K a phase transition from the low symmetry room temperature phase to the simple cubic high temperature phase can be observed. Similar to Cu_7PSe_6 a rate-dependent hysteresis-like behavior can be observed between the heating and cooling data at the phase transition. The cation disordering during the heating process and the cation ordering during the cooling process appears gradually over a temperature range of 20 to 30 K. Above 410 K the hysteresis disappears. However the temperature dependence of the electrical resistivity above the phase transition cannot be investigated as the sample start to decompose above 440 to 450 K.

The Seebeck coefficient increases from about -120 μV/K at room temperature to -90 μV/K at 430 K. The negative values indicate that electrons are the major charge carriers, resulting from intrinsic defects. The decreasing absolute values indicate that intrinsic conduction caused by the thermal excitation of charge carriers plays a role even at moderate temperatures as a result of a small band gap. An Arrhenius plot has been obtained from the electrical resistivity data below the phase transition led to a band gap around 0.1 eV. However this value might be inaccurate, due to the small investigated temperature interval. In contrast to Cu_7PSe_6 the overall values of the electrical resistivity are much lower.

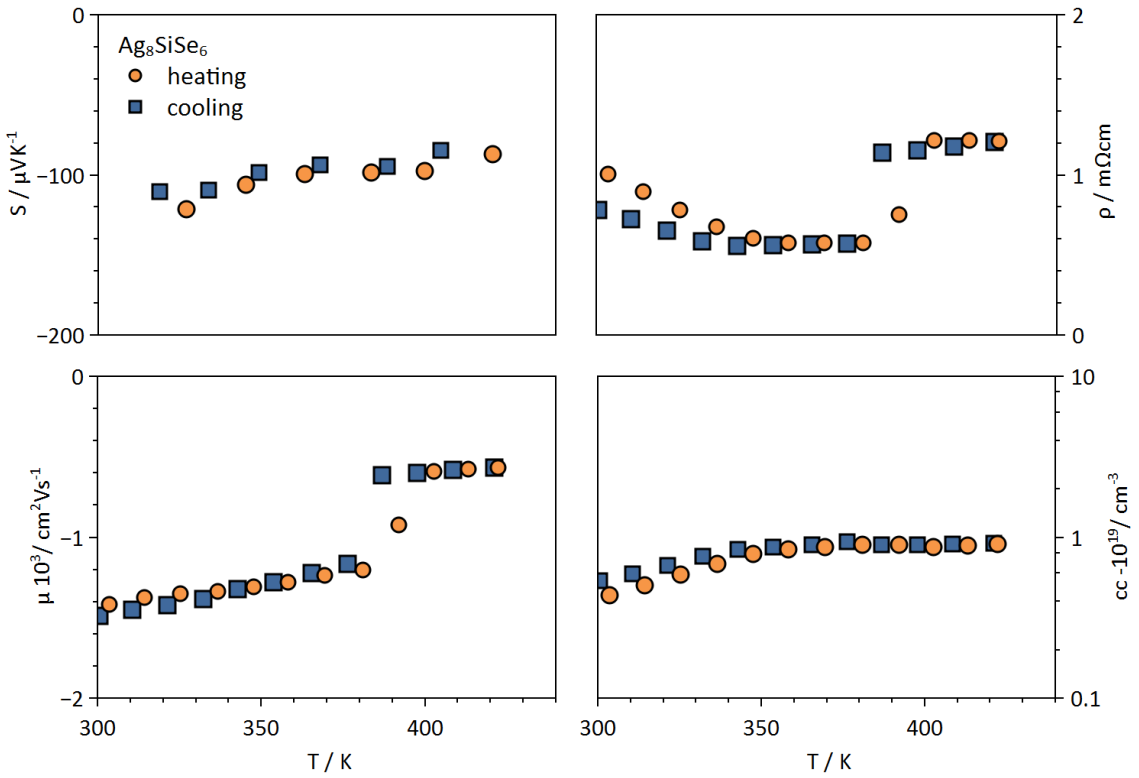

Figure 61. Electrical transport properties in Ag_8SiSe_6 including Seebeck coefficient (top left), electrical resistivity (top right), Hall mobility (bottom left) and Hall carrier concentration (bottom right). Orange circles represent heating data, blue squares represent cooling data. At 390 K a phase transition between the room temperature phase and the cubic high temperature phase is observed. Ag_8SiSe_6 shows extrinsic electron transport as a result of intrinsic defects.

Temperature dependent Hall measurements were performed in order to obtain Hall carrier mobilities μ_H and Hall carrier concentrations n_H. In contrast to Cu_7PSe_6 the Hall carrier mobilities are extremely large and negative (Figure 61, bottom left). The carrier mobilities at room temperature are around -1500 $cm^2(Vs)^{-1}$ and decrease with increasing temperature.

At the phase transition the Hall mobilities drop to -500 $cm^2(Vs)^{-1}$ which can be attributed to the increase of disorder in the cation sublattice leading to additional charge carrier scattering. The Hall carrier concentration shows a slightly increasing trend from 300 to 350 K (Figure 61, bottom right). At higher temperatures, the Hall carrier concentration stays constant around 10^{19} cm^{-3}.

10.3 Thermal transport in Ag_8SiSe_6

The total thermal conductivity of Ag_8SiSe_6 is shown in Figure 62. The absolute values are around 1 $W(Km)^{-1}$ before the phase transition and drop to 0.75 $W(Km)^{-1}$ after the phase transition. However, the electrical resistivities in Ag_8SiSe_6 are much lower compared to the electric resistivities in Cu_7PSe_6, therefore the electronic contribution to the total thermal conductivity is significant over the whole temperature range.

The electronic contribution to the thermal conductivity has been estimated, using the Wiedemann-Franz law ($\kappa_{el} = LT\rho^{-1}$), with $L = 1.5 \cdot 10^{-8}$ $W\Omega K^{-2}$ for non-degenerate materials. The obtained values of the lattice contribution to the thermal conductivities are around 0.5 $W(Km)^{-1}$ at room temperature and decrease slightly to around 0.3 at higher temperatures. These values are similar to the lattice thermal conductivities in Cu_7PSe_6 and the drop in the total thermal conductivity can be attributed to the electronic contribution to the lattice thermal conductivity. As already determined in the previous chapters, thermal conductivities in Argyrodite-type compounds are much lower than typical lattice thermal conductivities of 1 $W(Km)^{-1}$ found in thermoelectric materials. Again, this should be a result of the low symmetry crystal structure and high cation disorder. In the case of Ag_8SiSe_6, no ultrasonic measurements of sound velocities were performed which would allow to estimate the glass limit of the thermal conductivity and the Debye temperature.

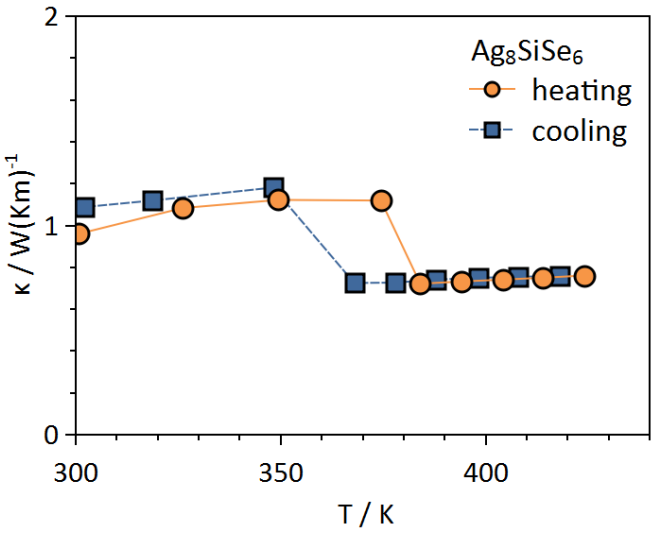

Figure 62. Thermal conductivity κ in Ag_8SiSe_6 (left). The orange circles represent heating data, blue squares represent cooling data.

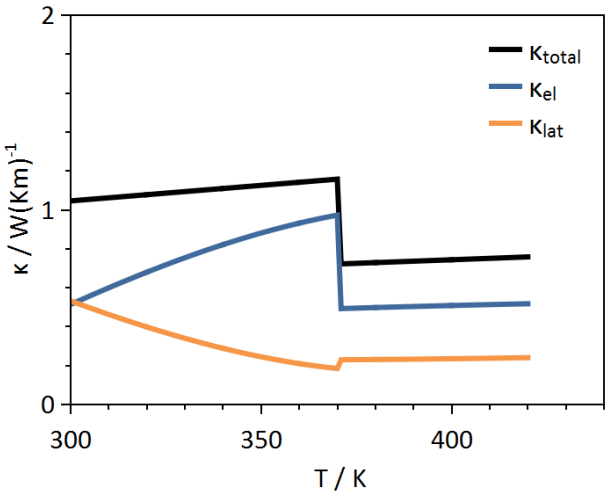

Figure 63. Electronic and lattice contribution to the κ in Ag_8SiSe_6. The black line shows a rough fit of the total thermal conductivity, the blue line shows the electronic contribution to the total thermal conductivity, which has been estimated from the Wiedemann-Franz law. The resulting lattice thermal conductivity is shown in orange, illustrating that the jump in the total thermal conductivity is fully a result of the electronic contribution. Overall the lattice thermal conductivity shows a slightly decreasing trend.

10.4 Figure of merit.

The maximum *zT* of 0.6 to 0.7 at 300 K to 350 K is very promising (Figure 64), as exclusively a nominally valence precise bulk material was studied.

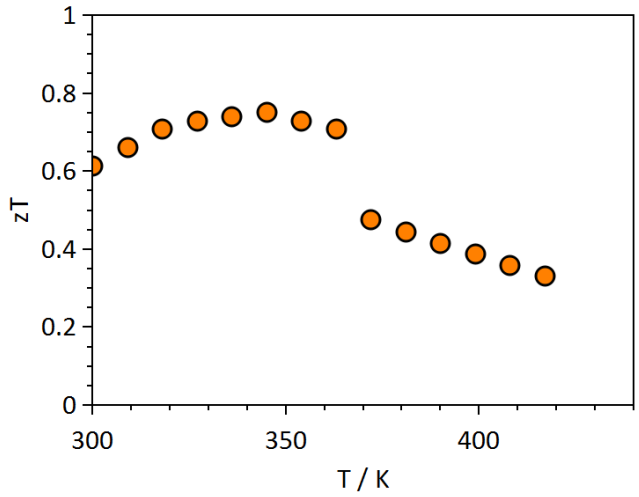

Figure 64. Temperature dependence of the dimensionless figure of merit *zT*.

This value is comparable to the *zT* value for not optimized bulk Bi_2Te_3 at room temperature, which is around 0.8. Here, the power factor needs to be optimized via substitution and doping in order to obtain higher values for the figure of merit in Ag_8SiSe_6. In order to analyze the transport and predict the optimum carrier densities for a maximum figure of merit, a single parabolic band model has been applied to the thermoelectric transport data of Ag_8SiSe_6.[127] The resulting prediction of *zT* versus Hall carrier concentration is shown in Figure 65.

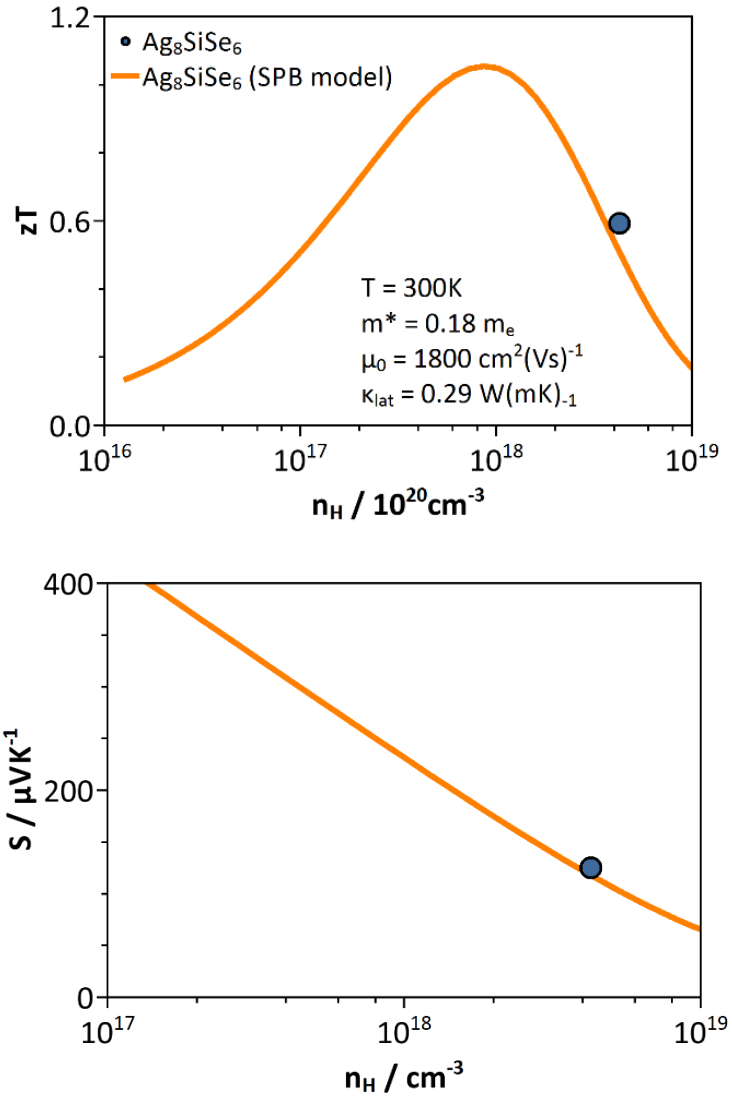

Figure 65. Single parabolic band model of the transport data of Ag_8SiSe_6 leading to estimates of the effective mass m^* and the mobility parameter μ_0 allowing a prediction of the thermoelectric figure of merit *zT* for different carrier concentrations. The model assumes acoustic phonon scattering limits the carrier mobility. Reducing the electron-carrier concentration in Ag_8SiSe_6 by one order of magnitude is predicted to result in a maximum *zT* of 1.1 at 300 K.

Assuming acoustic phonon scattering to limit the carrier mobility Ag_8SiSe_6 is predicted to reach a maximum *zT* of 1.1 at 300 K. This value is comparable to the state-of-the-art *zT* value for bulk materials at room temperature, which is around 1.1 achieved in $Bi_{2-x}Sb_xTe_3$.[184,185] Figure 23 shows that the samples of Ag_8SiSe_6 intrinsically have a Hall carrier concentration of 5×10^{18} carriers per cm^3, much greater than the optimum value of 8×10^{17} cm^{-3}. Doping this material with an electron acceptor should reduce the amount of electrons in Ag_8SiSe_6 and therefore lower the carrier concentrations into a range of much higher figures of merit.

Chapter 11

Thermoelectric transport in $Cu_{1+x}Fe_{1+y}Te_2$

Thermoelectric Properties of Layered $Cu_{1+x}Fe_{1+y}Te_2$ with Variable Cation Content

The last chapter of this thesis focusses on $Cu_{1+x}Fe_{1+y}Te_2$-type compounds which are closely related to chalcopyrites. Chalcopyrite-type compounds crystallizes in a tetrahedrally bonded network structure and some representatives achieve extremely high thermoelectric efficiencies. Copper-iron-telluride, however, crystallizes in the layered Rickardite structure. In addition to the tetrahedral bonded ions within the layers, this structure provides additional pyramidal cation sites between the layers leading to compositions with variable amounts of cations ($Cu_{1+x}Fe_{1+y}Te_2$). As the phase pure bulk synthesis of this compound is difficult, there is hardly any research on the physical properties of these compounds.

In this context a method for the phase pure bulk synthesis of this compound has been developed and the thermoelectric properties of $Cu_{1+x}Fe_{1+y}Te_2$ have been investigated for the first time with regard to changes in x and y.

11.1 Chemical characterization

Samples of $Cu_{1+x}Fe_{1.22}Te_2$ and $Cu_{1.33}Fe_{1+y}Te_2$ were checked for phase purity via x-ray powder diffraction. As the thermoelectric properties of $Cu_{1+x}Fe_{1+y}Te_2$ compounds have not been investigated yet, phase purity of the measured samples is very important. Here, even small amounts of impurities can have a huge influence on the electronic and thermal properties of a material. All reflections of $Cu_{1+x}Fe_{1.22}Te_2$ could be indexed to the tetragonal phase of Rickardite $Cu_{2.8}Te_2$ (space group *P*4/*nmm*).[186] No secondary phases were observed and the large background is due to fluorescence of Fe-ions as Cu K_α radiation was used. Iron and copper-ions cannot be distinguished by x-ray diffraction techniques due to their similar atomic scattering form factors for x-rays. However, lattice parameters were derived from Pawley-fits (Figure 66 to Figure 69). Unfortunately, the lattice parameters for the different compositions do not vary significantly nor do these values display a trend upon increasing iron or copper-ion concentration. Pawley-fits of $Cu_{1.13}Fe_{1+y}Te_2$ are shown in Figure 70 - Figure 73.

Table 7. Lattice parameters for $(Cu,Ag)_7PSe_6$ derived from Pawley fits,

x in $Cu_{1+x}Fe_{1+y}Te_2$	y in $Cu_{1+x}Fe_{1+y}Te_2$	c / Å	a / Å	R_{wp} / %	GoF
1.15	1.22	3.983(1)	6.107(4)	2.8	1.3
1.20	1.22	3.980(0)	6.117(0)	2.8	1.3
1.25	1.22	3.980(5)	6.130(9)	3.0	1.5
1.30	1.22	3.975(3)	6.128(5)	3.0	1.5
1.13	1.25	3.988(5)	6.107(1)	3.6	1.5
1.13	1.30	3.990(0)	6.101(9)	3.8	1.6
1.13	1.35	3.989(0)	6.099(7)	5.2	2.3
1.13	1.40	3.987(7)	6.097(1)	6.1	3.0

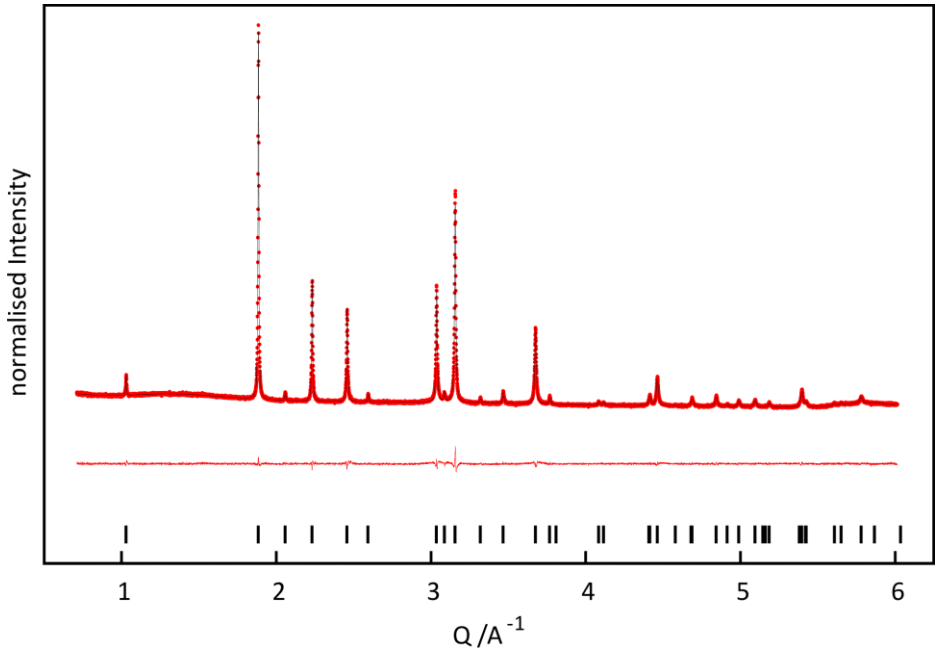

Figure 66. X-ray powder diffraction data for $Cu_{1.15}Fe_{1.22}Te_2$ (red dots), including profile fit (black solid line) and profile difference (red solid line) from the corresponding Pawley fit. All reflections could be indexed to the tetragonal $Cu_{2.8}Te_2$ phase with a = 3.983 Å, c = 6.107 Å, R_{wp} = 2.8 % and GoF = 1.3.

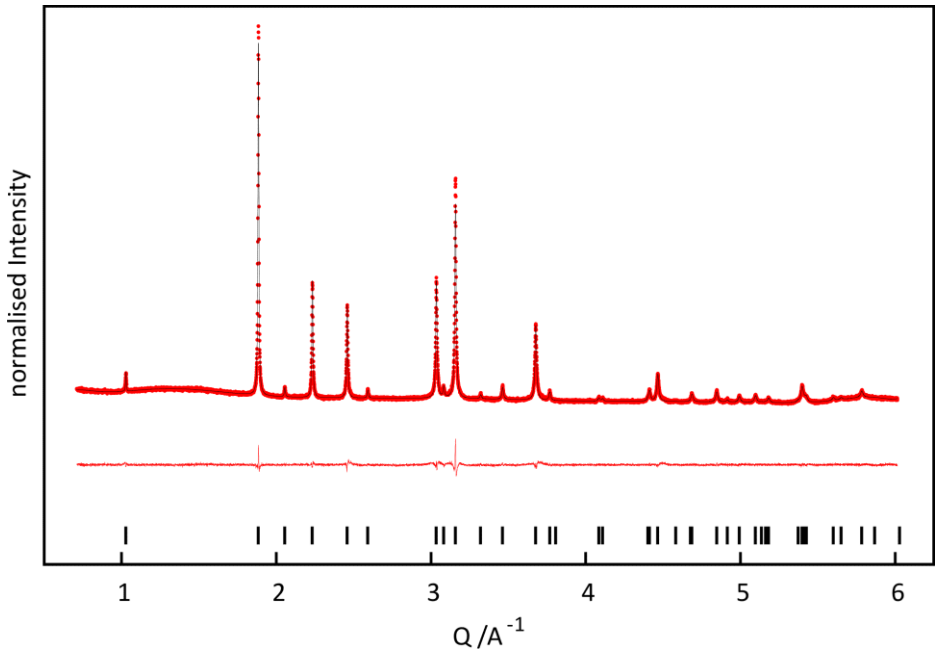

Figure 67. X-ray powder diffraction data for $Cu_{1.20}Fe_{1.22}Te_2$ (red dots), including profile fit (black solid line) and profile difference (red solid line) from the corresponding Pawley fit. All reflections could be indexed to the tetragonal $Cu_{2.8}Te_2$ phase with a = 3.980 Å, c = 6.117 Å, R_{wp} = 2.8 % and GoF = 1.3.

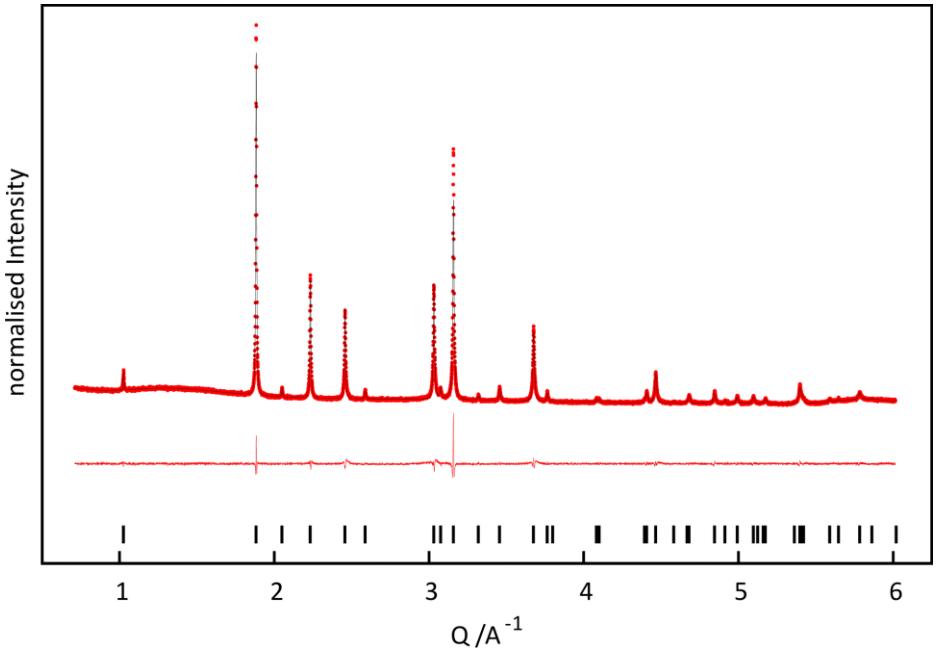

Figure 68. X-ray powder diffraction data for $Cu_{1.25}Fe_{1.22}Te_2$ (red dots), including profile fit (black solid line) and profile difference (red solid line) from the corresponding Pawley fit. All reflections could be indexed to the tetragonal $Cu_{2.8}Te_2$ phase with a = 3.985 Å, c = 6.131 Å, R_{wp} = 3.0 % and GoF = 1.5.

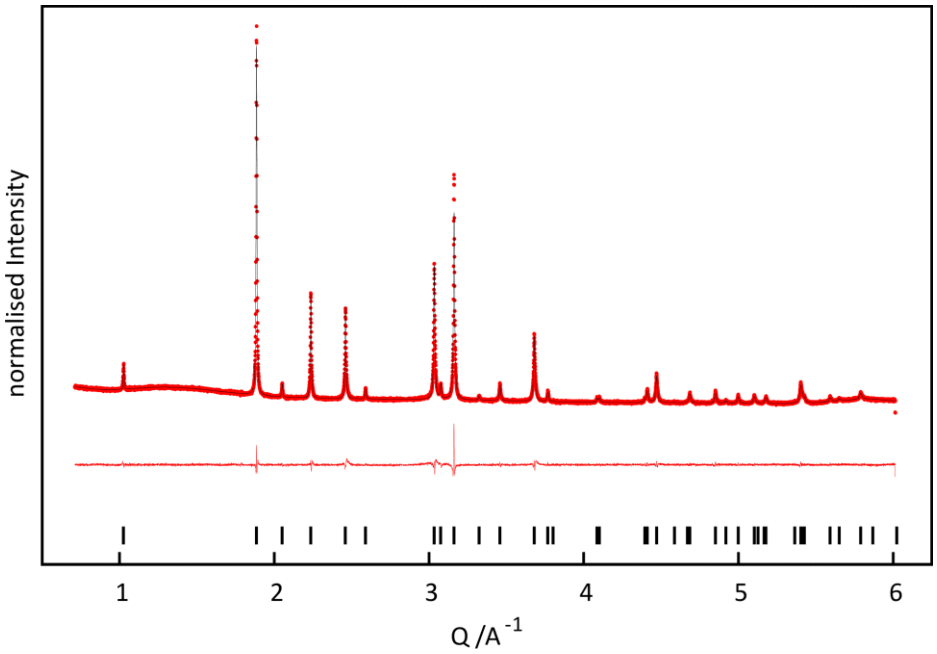

Figure 69. X-ray powder diffraction data for $Cu_{1.30}Fe_{1.22}Te_2$ (red dots), including profile fit (black solid line) and profile difference (red solid line) from the corresponding Pawley fit. All reflections could be indexed to the tetragonal $Cu_{2.8}Te_2$ phase with a = 3.983 Å, c = 6.128 Å, R_{wp} = 2.8 % and GoF = 1.3.

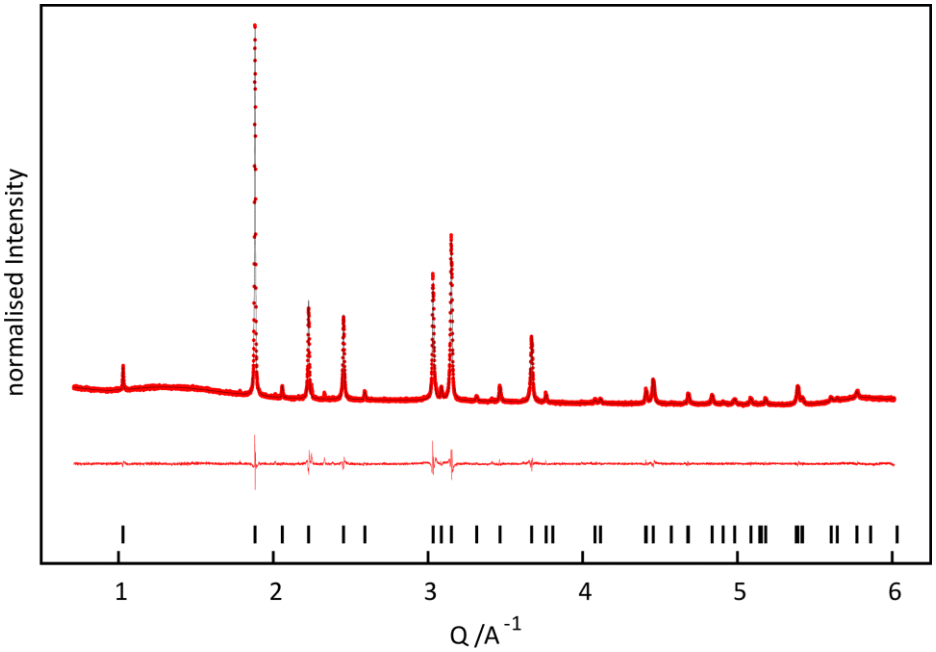

Figure 70. X-ray powder diffraction data for $Cu_{1.13}Fe_{1.25}Te_2$ (red dots), including profile fit (black solid line) and profile difference (red solid line) from the corresponding Pawley fit. All reflections could be indexed to the tetragonal $Cu_{2.8}Te_2$ phase with a = 3.989 Å, c = 6.107 Å, R_{wp} = 3.6 % and GoF = 1.5.

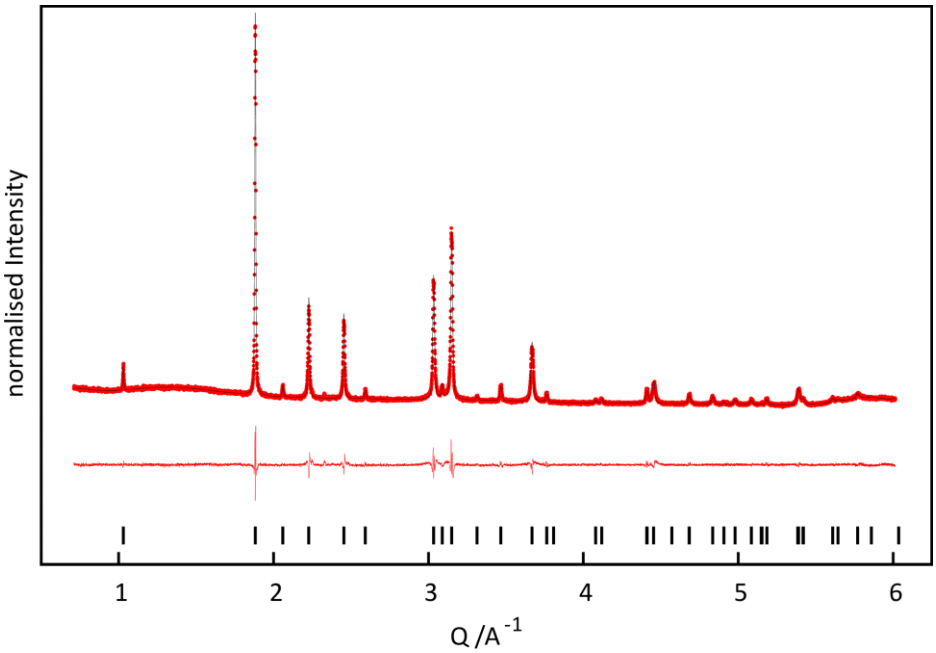

Figure 71. X-ray powder diffraction data for $Cu_{1.13}Fe_{1.30}Te_2$ (red dots), including profile fit (black solid line) and profile difference (red solid line) from the corresponding Pawley fit. All reflections could be indexed to the tetragonal $Cu_{2.8}Te_2$ phase with a = 3.990 Å, c = 6.102 Å, R_{wp} = 3.8 % and GoF = 1.6.

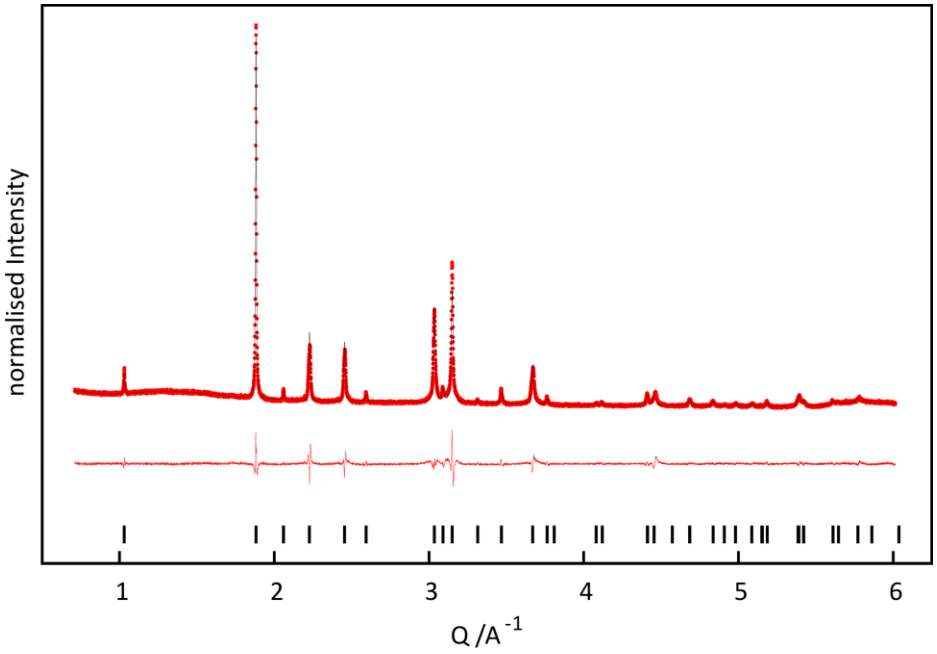

Figure 72. X-ray powder diffraction data for $Cu_{1.13}Fe_{1.35}Te_2$ (red dots), including profile fit (black solid line) and profile difference (red solid line) from the corresponding Pawley fit. All reflections could be indexed to the tetragonal $Cu_{2.8}Te_2$ phase with a = 3.989 Å, c = 6.100 Å, R_{wp} = 5.2 % and GoF = 2.3.

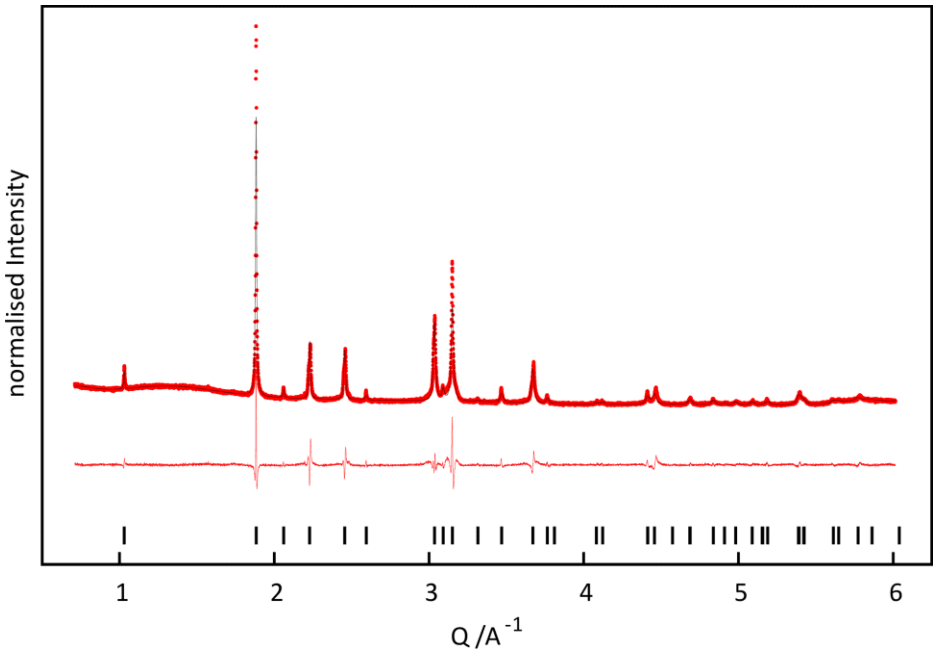

Figure 73. X-ray powder diffraction data for $Cu_{1.13}Fe_{1.40}Te_2$ (red dots), including profile fit (black solid line) and profile difference (red solid line) from the corresponding Pawley fit. All reflections could be indexed to the tetragonal $Cu_{2.8}Te_2$ phase with a = 3.988 Å, c = 6.097 Å, R_{wp} = 6.1 % and GoF = 3.0.

$Cu_{1.13}Fe_{1.25}Te_2$ and $Cu_{1.13}Fe_{1.30}Te_2$ show very small additional reflections which might be attributed to a second phase of $FeTe_2$ (Frohbergite), which crystallizes in an orthorhombic unit cell with a = 5.268, b = 6.273 and c = 3.879.[187] They are not included in the fits, as only two reflections stand out well from the background. Interestingly $Cu_{1.13}Fe_{1.35}Te_2$ and $Cu_{1.13}Fe_{1.40}Te_2$ don't show these additional reflections. However, shape and intensities of the reflections are not described very well by the Pawley fits and R_{wp} and GoF values of the fits are much higher compared to the other samples. Here, most reflections are asymmetric due to small shoulders left to the maximum, which might be attributed to two types of unit cells with different site occupancy and different unit cell size. This explanation would assume, that Cu^+ and Fe^{3+} are not statistically distributed on the different voids in the anion lattice and that there is a more complex site occupation. However, due to their similar atomic form factors for x-rays, Fe^{3+} and Cu^+ cannot be distinguished by x-ray diffraction techniques and a Rietveld refinement of the site occupancies with the given data is not possible. Here, neutron diffraction data would be needed to elucidate the nature of the underlying disorder in these compounds.

11.2 Electronic transport in $Cu_{1+x}Fe_{1+y}Te_2$

The temperature dependent electrical resistivity of $Cu_{1.13}Fe_{1.22}Te_2$, as well as the phases with most additional copper and iron ($Cu_{1.30}Fe_{1.22}Te_2$ and $Cu_{1.13}Fe_{1.40}Te_2$, respectively) are shown in Figure 74 (top). Even though the absolute values of the electrical resistivities are very low, they decreases with increasing temperature, as expected for a semiconductor. Here, the temperature dependence of the conductivity is governed by an Arrhenius-like, thermally activated process across the band gap which can be described through $\sigma = A\exp(-E_a/(2k_BT))$, where σ is the electric conductivity, A is a constant, E_a is the activation energy and k_B the Boltzmann constant. Arrhenius plots of the data from 300 K to 500 K are shown in Figure 75. The calculated activation energies are summed up in Table 8. The activation energies are below 0.1 eV for all three compositions, indicating that all compounds are semimetals. Temperature dependent Hall measurements were performed in order to obtain Hall carrier mobilities μ_H and Hall carrier concentrations n_H. The Hall carrier mobilities randomly scattered around zero, indicating that both electrons and holes contribute to the electrical conductivity. In this case the values obtained for the Hall carrier concentrations are not reasonable.

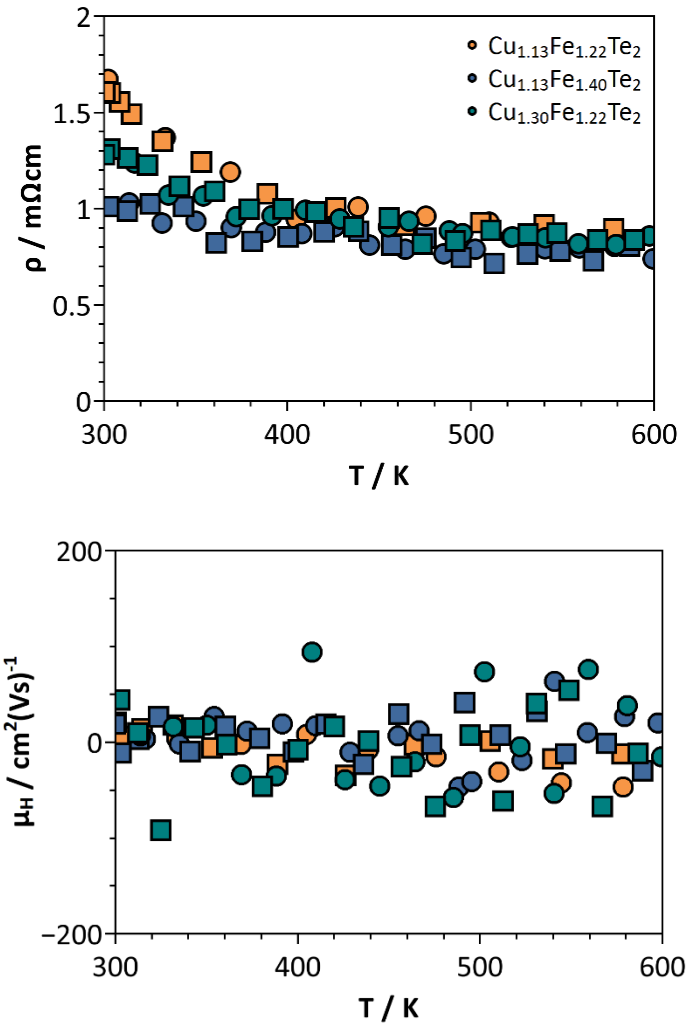

Figure 74. Electronic transport in $Cu_{1+x}Fe_{1+y}Te_2$. Temperature dependences of the electrical resistivity ρ (top) and Hall mobility (bottom). Circles represent heating data, squares represent cooling data. Orange data represents $Cu_{1.13}Fe_{1.22}Te_2$, blue data represents $Cu_{1.13}Fe_{1.40}Te_2$ and cyan data represents $Cu_{1.30}Fe_{1.22}Te_2$. The electrical resistivity decreases slightly with increasing temperature, which is typical for a semiconductor. However, the absolute values are very low, indicating that all samples are semimetals. This assumption is supported by the Hall mobility values which are randomly jumping from positive to negative values, indicating that both holes and electrons contribute to the electrical conductivity.

Table 8. Activation energies of $Cu_{1.13}Fe_{1.22}Te_2$, $Cu_{1.13}Fe_{1.40}Te_2$ and $Cu_{1.30}Fe_{1.22}Te_2$.

x in $Cu_{1+x}Fe_{1+y}Te_2$	y in $Cu_{1+x}Fe_{1+y}Te_2$	E_A
1.13	1.22	0.08 eV
1.30	1.22	0.05 eV
1.13	1.40	0.04 eV

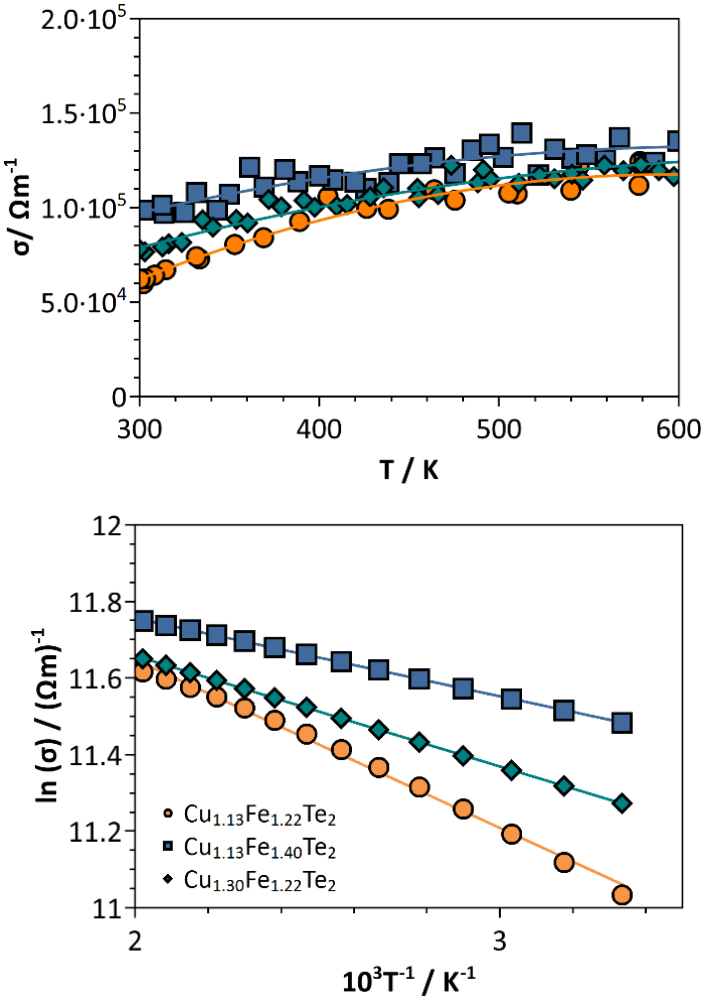

Figure 75. Temperature dependence of the electrical conductivity in $Cu_{1+x}Fe_{1+y}Te_2$ with corresponding fit curves (top). Circles represent heating data, squares represent cooling data. The fits were used for obtaining Arrhenius plots for $Cu_{1+x}Fe_{1+y}Te_2$ (bottom). Orange data represents $Cu_{1.13}Fe_{1.22}Te_2$, blue data represents $Cu_{1.13}Fe_{1.40}Te_2$ and cyan data represents $Cu_{1.30}Fe_{1.22}Te_2$. In the temperature range from 300 to 500 K *ln(σ)* shows an almost linear *1/T* dependence as predicted for a thermally activated, Arrhenius-like process. Linear fits of the data lead to very small activation energies of 0.04 to 0.08 eV, indicating that all compounds show semi-metallic transport behavior.

The Temperature dependences of the Seebeck coefficient is shown in Figure 76. As expected for semimetals the Seebeck coefficients for all investigated compositions are extremely small and show almost no temperature dependence. The Seebeck coefficient of $Cu_{1.13}Fe_{1.22}Te_2$ is about -20 µV/K and the Seebeck coefficients of the samples with increased iron and copper content are even lower. Over the whole temperature range, intrinsic conduction caused by thermal excitation of carriers is the main contributor to the electrical conductivity, creating both electrons and holes. This observation is consistent with the very small calculated activation energies.

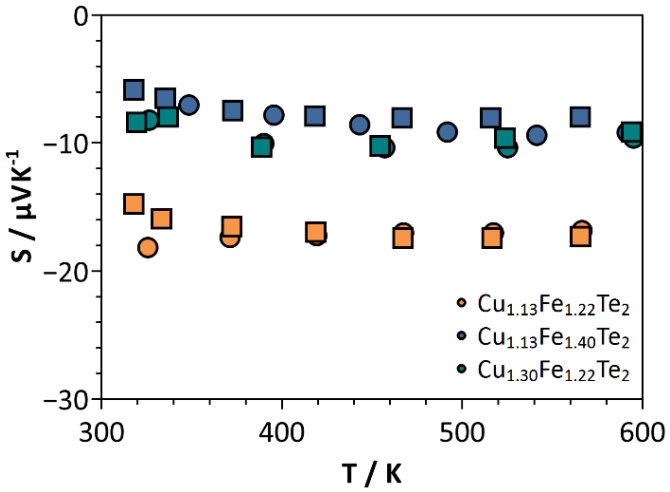

Figure 76. Temperature dependences of the Seebeck coefficient in $Cu_{1+x}Fe_{1+y}Te_2$. Circles represent heating data, squares represent cooling data. Orange data represents $Cu_{1.13}Fe_{1.22}Te_2$, blue data represents $Cu_{1.13}Fe_{1.40}Te_2$ and cyan data represents $Cu_{1.30}Fe_{1.22}Te_2$. Measured Seebeck coefficients are extremely small and show almost no temperature dependence.

11.3 Thermal transport in $Cu_{1+x}Fe_{1+y}Te_2$

The total thermal conductivity of $Cu_{1+x}Fe_{1+y}Te_2$ increases slightly from 1.5 $W(Km)^{-1}$ to 2.3 $W(Km)^{-1}$ in the measured temperature range (Figure 77). The absolute values for $Cu_{1.13}Fe_{1.22}Te_2$, $Cu_{1.13}Fe_{1.40}Te_2$ and $Cu_{1.30}Fe_{1.22}Te_2$ are very similar.

As all investigated samples of $Cu_{1+x}Fe_{1+y}Te_2$ show similar and very low absolute values of the electrical resistivities, the electronic contribution to the total thermal conductivity is significant over the whole temperature range and only differs slightly for the different samples. The electronic contribution to the thermal conductivity has been estimated, using the Wiedemann-Franz law ($\kappa_{el} = LT\rho^{-1}$), with $L = 1.5 \cdot 10^{-8}$ $W\Omega K^{-2}$ for non-degenerate materials. The obtained values of the lattice contribution to the thermal conductivities are around 1.2 $W(Km)^{-1}$ for $Cu_{1.13}Fe_{1.22}Te_2$ and around 1.0 for $Cu_{1.30}Fe_{1.22}Te_2$ and $Cu_{1.30}Fe_{1.22}Te_2$ which are a little bit higher compared to the lattice thermal conductivities of Cu_2Se or Argyrodite-type samples investigated in this thesis but can be compared to the values of other typical thermoelectric tellurides like PbTe and Bi_2Te_3. Further, almost no temperature dependence of the thermal conductivity can be seen over the investigated temperature range, which is typical for highly disordered materials.[42] These low, temperature independent thermal conductivities must therefore be the result of a very high positional disorder on the different cation sites or even a “molten” cation sublattice

at higher temperatures. A very short phonon mean free path results in very low lattice thermal conductivities in range of the glass limit. The degree of disorder seems to be increased in the samples with an increased amount of metal ions leading to even lower lattice thermal conductivities. As no ultrasonic measurements of sound velocities were performed on the compounds, no estimation of the Debye temperature or the glass limit for the lattice thermal conductivity were possible.

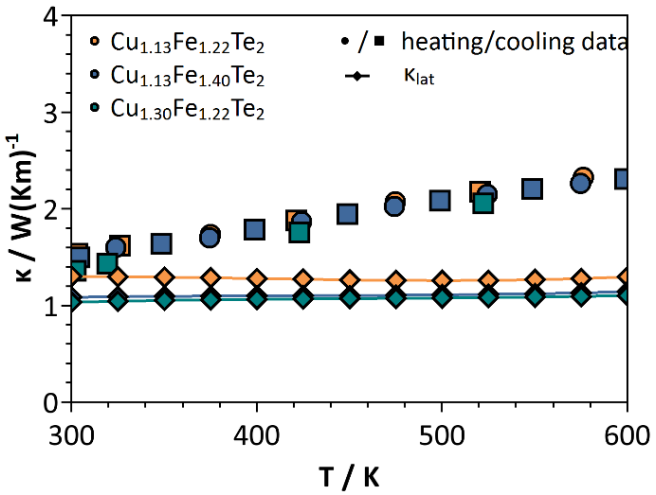

Figure 77. Temperature dependences of the thermal conductivity in $Cu_{1+x}Fe_{1+y}Te_2$. Circles represent heating data, squares represent cooling data. Orange data represents $Cu_{1.13}Fe_{1.22}Te_2$, blue data represents $Cu_{1.13}Fe_{1.40}Te_2$ and cyan data represents $Cu_{1.30}Fe_{1.22}Te_2$. Diamonds represent the corresponding values for the lattice thermal conductivities which show almost no temperature dependence.

Chapter 12

Summary

This thesis discusses the structural and thermoelectric properties of copper and silver ion conducting thermoelectric materials. In this context, we particularly focus on circumventing the high temperature thermal degradation issues which limit the implementation of superionic materials in thermoelectric generators. Two possible approaches are discussed which allow the use of ionic conducting materials as thermoelectric materials at temperatures close to room temperature.

First, we have focused on the compound $Cu_{2-\delta}Se$ which is one of the most comprehensively investigated ionic conducting thermoelectrical materials with high efficiency at high temperatures. In this context, we have demonstrated that $Cu_{2-\delta}Se$ has the potential to be a high-performance thermoelectric material for moderate temperatures, if the intrinsic, heavily doped character can be altered. Using bromide ions as electron donors, we have successfully reduced the hole concentration in $Cu_{2-y}Se_{1-x}Br_x$. Exploring the different possible scattering mechanisms for holes in this material, we have elucidated that doping on the selenide site with bromide ions, which mostly contribute to the valence band, leads to enhanced alloy scattering and to a reduced mobility.

Although bromide ions are not an ideal dopant to achieve the anticipated thermoelectric performance in $Cu_{2-\delta}Se$ for that reason, different strategies for improvement may be applied as ionized impurity scattering was excluded. Furthermore, we have discussed the reduced doping efficiency of bromide ions by a counteracting increasing amount of copper vacancies. The interesting defect chemistry of $Cu_{2-\delta}Se$ shows, for the first time, that compensating defects and an effective pinning of the Fermi level can be achieved when shifting the chemical potential towards the valence band edge. This work demonstrates the need of a complete understanding of the underlying scattering mechanisms as well as the crystal and defect chemistry of a material in order to achieve high figure of merit thermoelectrics.

Secondly, we have investigated the thermoelectric properties of several Argyrodite-type materials, representing a class of more complex ionic conductors ($A^{x+}_{12-y/x}B^{y+}Q^{2-}_6$ for ternary compounds). The ionic conductivity results from a molten A-cation sublattice, while the immobile B-cations and the Q-anions form the lattice. The huge variety of compositions in the Argyrodite family provides a huge playground for the investigation of structure-property relationships making this class of materials an excellent model system for “phonon-liquid electron-crystal” thermoelectric materials.

As the first representative of copper-ion conducting Argyrodites, we have synthesized Cu_7PSe_6 and characterized its thermoelectric transport properties. Cu_7PSe_6 shows potential as a thermoelectric material due to an extraordinarily low thermal conductivity which arises from a high structural disorder and a liquid-like behavior of the cation sublattice. The “molten” Cu-sublattice leads to a softening of phonon modes, ultimately affecting the thermal transport. In order to investigate the effect of mobile cation substitution on the thermoelectric properties, we have synthesized the series of solid solutions $Cu_{7-x}Ag_xPSe_6$. Throughout the series a Vegard-like behavior of lattice parameters is observed. In contrast to Cu_7PSe_6, the silver containing compounds do not show potential as a thermoelectric material due to a much higher electrical resistivity. In addition, a transition from p-type transport in Cu_7PSe_6 to n-type transport in Ag_7PSe_6 is observed. The effect of the isovalent cation substitution on the room temperature thermal conductivity has been investigated and revealed a reduction of the lattice thermal conductivity of around 30 %. Predictions for the lattice thermal conductivity using the Callaway model indicate that both, mass and strain contrast, give rise to the thermal conductivity reduction.

In order to investigate the influence of the amount of mobile cations per formula unit on the thermoelectric properties of Argyrodite-type compounds, we have synthesized the silver ion conducting Argyrodite Ag_8SiSe_6 and characterized the transport properties. Although the compounds degrades at relatively low temperatures, Ag_8SiSe_6 shows a very high figure of merit at moderate temperatures. In contrast to the electrically insulating Ag_7PSe_6, Ag_8SiSe_6 provides high electrical conductivity with extremely high electron mobilities in combination with a low thermal conductivity making this compound potentially competitive to bismuth-telluride-type materials. Furthermore, we have demonstrated that Ag_8SiSe_6 has the potential to reach even higher figure of merits at a low temperature, if the charge carrier concentration can be reduced. Thus, Argyrodites are a new and promising approach to novel thermoelectric materials within the phonon-liquid electron-crystal concept.

In the last part of this thesis, we have investigated $Cu_{1+x}Fe_{1+y}Te_2$ of the layered Rickardite structure type, which is closely related to the Chalcopyrite structure type. This structure type provides additional pyramidal-quadratic cation sites between the layers leading to cation rich non-stoichiometric phases ($Cu_{1+x}Fe_{1+y}Te_2$) allowing the investigation of the influence of x and y on the thermoelectric properties. In this context, we have developed and optimized a phase pure bulk synthesis of this compound with variable cation content and investigated the thermoelectric transport properties. Since all investigated samples were semimetals with very small Seebeck coefficients further research on these compounds is necessary. For example, parts of the telluride anions could be substituted with selenide anions which might lead to higher Seebeck coefficients.

Curriculum vitae

[redacted]

[redacted]

References

(1) Vining, C. B. *Nat. Mat.* **2009**, *8*, 83.

(2) Armaroli, N.; Balzani, V. *Angew. Chem., Int. Ed.* **2007**, *46*, 52-66.

(3) DiSalvo, F. J. *Science* **1999**, *285* (5428), 703-706.

(4) Bell, L. E. *Science* **2008**, *321* (5895), 1457-1461.

(5) Snyder, G. J.; Toberer, E. S. *Nat. Mater.* **2008**, *7* (2), 105-114.

(6) Tritt, T.; Subramanian, M. *MRS Bull.* **2006**, *31*, 188-198.

(7) Goldsmid, H. J. *Thermoelectric Refrigeration*; Plenum Press: New York, 1964.

(8) Goldsmid, H. J. *Applications of Thermoelectricity*; Butler & Tanner Ltd: London, 1960.

(9) Rowe, D. M. in *Thermoelectrics Handbook: Macro to Nano*; Rowe, D. M., Ed., 2nd ed.; CRC Press: Boca Raton, 2006.

(10) Ashcroft, N.W.; Mermin, N. D. *Solid State Physics*; Thomson Learning Inc.: United States of America, 1976.

(11) Ziman, J. M. *Electrons and Phonons. The Theory of Transport Phenomena in Solids*; Oxford University Press: London, 1963.

(12) Sootsman, J. R.; Chung, D. Y.; Kanatzidis, M. G. *Angew. Chem., Int. Ed.* **2009**, *48*, 8616.

(13) Eliott, S. R. in *The Physics and Chemistry of Solids*; John Wiley & Sons, 1998.

(14) Demtröder, W. *Experimentalphysik 3,* Springer-Verlag, 2010**.**

(15) Slack, G. A. in *Design concepts for improved thermoelectric materials*, MRS Proceedings. Vol. 478. Cambridge University Press, 1997.

(16) Slack, G. A. in *Handbook of Thermoelectrics*; Rowe, D. M., Ed.; CRC Press: Boca Raton, 1995, p 407.

(17) Kittel, C. *Introduction to solid state physics* Wiley, 2005.

(18) Jones, W.; March, N. H. *Theoretical solid state physics: Perfect lattices in equilibrium* (Vol. 1). Courier Corporation, 1985.

(19) Cox, P. A. *The Electronic Structure and Chemistry of Solids*, Oxford University Press, 1987.

(20) Davies, J. H. *The physics of low-dimensional semiconductors: an introduction*, Cambridge university press, 1997.

(21) Goldsmid, H. J. *Introduction to Thermoelectricity*; Springer Verlag: Berlin, 2009.

(22) Pei, Y., LaLonde, A., Iwanaga, S., Snyder, G. J. *Energy Environ. Sci.* **2011**, *4*(6), 2085-2089.

(23) Heremans, J.; Hansen, O. P. *J. Phys. Chem. C* **1979**, *12*(17), 3483.

(24) May, A. F.; Snyder, G. J. in *Thermoelectrics Handbook: Thermoelectrics and its Energy Harvesting*; Rowe, D. M., Ed.; CRC Press: Boca Raton, FL, 2012; Chapter 11.

(25) May, A. F. *Ph.D. Thesis*, California Institute of Technology, 2010.

(26) Tremel, W.; Seshadri, R.; Finckh, E. W. *Chem. unserer Zeit* **2001**, 42.

(27) Whangbo, M.-H.; Canadell, E. *Chem. Rev.* **1991**, *91*, 965.

(28) Hoffmann, R. *Angew. Chem.* **1987**, *99*, 871.

(29) Böttger, P. H.; Pomrehn, G. S.; Snyder, G. J.; & Finstad, T. G. *Phys. Status Solidi A* **2011**, *208*(12), 2753-2759.

(30) Toberer, E. S.; May, A. F.; Snyder, G. J. *Chem. Mater.* **2010**, *22*, 624.

(31) Ferry, D. *Semiconductor transport*, CRC Press, 2000.

(32) Bhandari, C. M.; Rowe, D. M. in *Thermoelectrics Handbook: Thermoelectrics and its Energy Harvesting*; Rowe, D. M., Ed.; CRC Press: Boca Raton, FL, 2012; Chapter 11.

(33) Fistul, V. I. *Heavily Doped Semiconductors*, Plenum Press, New York, 1969.

(34) Wilson, A.H. *The Theory of Metals*, The Syndics of the Cambridge University Press, 1958.

(35) Bardeen, J.; Shockley, W. *Phys. Rev.* **1950**, *80*, 72-80.

(36) Chattopadhyay, D.; Queisser, H. J. *Rev. Mod. Phys.* **1981**, *53*, 745.

(37) Harrison, J. W.; Hauser, J. R. *Phys. Rev. B* **1976**, *13*, 5347-5350.

(38) Kim, H. S.; Gibbs, Z. M.; Tang, Y.; Wang, H.; Snyder, G. J. *APL Mater.* **2015**, *3*(4), 041506.

(39) Debye, P. in *Vorträge über die kinetische Theorie der Materie und Elektrizität*, by M. Planck et al., B.G. Teubner, Leipzig, 1914.

(40) Peierls, R. *Ann. Phys.* **1929**, *395*(8) 1055-1101.

(41) Kittel, C. *Phys. Rev.* **1949**, *75*(6), 972–974.

(42) Anderson, O. *J. Phys. Chem. Solids* **1963**, *24*, 909-917.

(43) Toberer, E. S.; Zevalkink, A.; Snyder, G. J. *J. Mater. Chem.* **2011**, *21*, 15843.

(44) Steigmeier, E.; Abeles B. *Phys. Rev.* **1964**, *136*, 1149–1155.

(45) Klemens, P. G. *Solid State Physics*, 7th ed.; Academic Press: New York, 1958.

(46) Soma, T. *Solid State Comm*. **1980**, *34*, 927–932.

(47) Slack, G. in *Solid state Phys.* Vol. 34, 1-71, Academic Press: New York, 1979.

(48) Frenkel, J. in *Kinetic Theory of Liquids*, 188–249, Oxford Univ. Press, 1947.

(49) Trachenko, K. *Phys. Rev. B* **2008**, *78*, 104021.

(50) Cahill, D.; Watson, S.; Pohl, R. *Phys. Rev. B* **1992**, *46*(10), 6131.

(51) Callaway, J.; Baeyer, H. C. *Phys. Rev.* **1960**, *126*, 1149-1154.

(52) Alekseeva, G.; Efimova, B.; Ostrovsk, L. M.; Serebrya, O. S.; Tsypin, M. *Sov. Phys. Semicond.* **1971**, *4*, 1122.

(53) Yang, J.; Meisner, G. P.; Chen, L. *Appl. Phys. Lett.* **2004**, *85*, 1140.

(54) Meisner, G.; Morelli, D.; Hu, S.; Yang, J.; Uher, C. *Phys. Rev. Lett.* **1998**, *80*, 3551-3554.

(55) Zhou, Z.; Uher, C.; Jewell, A.; Caillat, T. *Phys. Rev. B* **2005**, *71*, 235209.

(56) Heinrich, C. P.; Day, T. W.; Zeier, W.; Snyder, G.; Tremel, W. *J. Am. Chem. Soc.* **2014**, *136*, 442-8.

(57) Wang, H.; Lalonde, A. D.; Pei, Y.; Snyder, G. J. *Adv. Funct. Mater.* **2013**, *23* (12), 1586-1596.

(58) Snyder, G. J. *Electrochem. Soc. Interface* **2008**, 17(3), 54.

(59) Snyder, G. J. *Appl. Phys. Lett.* **2004**, *84*, 2436-2438.

(60) Snyder, G. J. in *Thermoelectrics Handbook: Macro to Nano*; Rowe, D. M., Ed., 2nd ed.; CRC Press: Boca Raton, 2006, Chapter 9.

(61) Vining, C. B. *Nat. Mater.* **2009**, *8*, 83.

(62) Scherrer, H.; Scherrer, S. in *Thermoelectics Handbook: Macro to Nano*, CRC Press LLC, Boca Raton 2006, chapter 27.

(63) Kim, S. Il; Mun, H. A.; Kim, H. S.; Hwang, S. W.; Roh, J. W.; Yang, D. J.; Shin, W. H.; Li, X. S.; Lee, Y. H.; Snyder, G. J.; Kim, S. W. *Science* **2015**, *348*(6230), 109–115.

(64) LaLonde, A. D.; Pei, Y.;Wang, H.; Jeffrey Snyder, *G. Mater. Today* **2011**, *14*, 526-532.

(65) Mahan, G. D.; Sofo, J. O. *Proc. Natl. Acad. Sci. U.S.A.* **1996**, *93*, 7436-7439.

(66) Wang, H.; Pei, Y.; Lalonde, A. D.; Snyder, G. J. *Proc. Natl. Acad. Sci. U.S.A.* **2012**, *109*, 9705–9709.

(67) Pei, Y.; Wang, H.; Snyder, G. J. *Adv. Mater.* **2012**, *24*, 6125-6135.

(68) Pei, Y.; LaLonde, A. D.; Wang, H.; Snyder, G. J. *Energy Environ. Sci.* **2012**, *5*, 7963-7969.

(69) Heremans, J. P.; Jovovic, V.; Toberer, E. S.; Saramat, A.; Kurosaki, K.; Charoenphakdee, A.; Yamanaka, S.; Snyder, G. J. *Science* **2008**, *321*(5888), 554-557.

(70) Zhang, Q.; Wang, H.; Liu, W.; Wang, H.; Yu, B.; Zhang, Q.; Tian, Z.; Ni, G.; Lee, S.; Esfarjani, K.; Chen, G.; Ren, Z. *Energy Environ. Sci.* **2012**, *5*, 5246-5251.

(71) Jaworski, C.; Heremans, *J. Phys. Rev. B* **2012**, *85*, 033204.

(72) Nielsen, M.; Levin, E.; Jaworski, C.; Schmidt-Rohr, K.; Heremans, J. *Phys. Rev. B* **2012**, *85*, 045210.

(73) Liu, W.; Tan, X.; Yin, K.; Liu, H.; Tang, X.; Shi, J.; Zhang, Q.; Uher, C. *Phys. Rev. Lett.* **2012**, *108*, 166601.

(74) Pei, Y.; Shi, X.; LaLonde, A.; Wang, H.; Chen, L.; Snyder, G. J. *Nature* **2011**, *473*, 66-69.

(75) Zebarjadi, M.; Esfarjani, K.; Dresselhaus, M. S.; Ren, Z. F.; Chen, G. *Energy Environ. Sci.* **2012**, *5*, 5147-5162.

(76) Yang, J.; Meisner, G. P.; Chen, L. *Appl. Phys. Lett.* **2004**, *85*, 1140-1142.

(77) Abeles B. *Phys. Rev.* **1963**, *131*, 1906-1911.

(78) Callaway, J. *Phys. Rev.* **1959**, *111*, 1046-1051.

(79) Meisner, G.; Morelli, D.; Hu, S.; Yang, J.; Uher, C. *Phys. Rev. Lett.* **1998**, *80*, 3551-3554.

(80) Zhou, Z.; Uher, C.; Jewell, A.; Caillat, T. *Phys. Rev. B* **2005**, *71*, 235209.

(81) Shi, X.; Yang, J.; Salvador, J. R.; Chi, M.; Cho, J. Y.; Wang, H.; Bai, S.; Yang, J.; Zhang, W.; Chen, L. *J. Am. Chem. Soc.* **2011**, *133*, 7837-7846.

(82) Pei, Y.; Heinz, N. A.; LaLonde, A.; Snyder, G. J. *Energy Environ. Sci.* **2011**, *4*, 3640-3645.

(83) Pei, Y.; Lensch-Falk, J.; Toberer, E. S.; Medlin, D. L.; Snyder, G. J. *Adv. Funct. Mater.* **2011**, *21*(2), 241-249.

(84) Johnsen, S.; He, J.; Androulakis, J.; Dravid, V. P.; Todorov, I.; Chung, D. Y.; Kanatzidis, M. G. *J. Am. Chem. Soc.* **2011**, *133*, 3460-3470.

(85) Minnich, A. J.; Dresselhaus, M. S.; Ren, Z. F.; Chen, G. *Energy Environ. Sci.* **2009**, *2*, 466-479.

(86) Poudeu, P. F. P.; D'Angelo, J.; Downey, A. D.; Short, J. L.; Hogan, T. P.; Kanatzidis, M. G. *Angew. Chem. Int. Ed.* **2006**, *45*, 3835–3839.

(87) Hicks, L. D.; Dresselhaus, M. S. *Phys. Rev. B* **1993**, *47*, 16631.

(88) Hicks, L. D.; Dresselhaus, M. S. *Phys. Rev. B,* **1993**, *47*, 16627.

(89) Sharp, J. W.; Jones, E. C.; Williams, R. K.; Martin, P. M.; Sales, B. C. *J. Appl. Phys.* **1995**, *78*, 1013.

(90) Sales, B.; Mandrus, D.; Williams, R. *Science* **1996**, *272*, 1325-1328.

(91) Nolas, G.S.; Morelli, D.T.; Tritt, T.M. *Annu. Rev. Mater. Sci.* **1999**, 89–116.

(92) Liu, M.-L.; Chen, I.-W.; Huang, F.-Q.; Chen, L.-D. *Adv. Mater.* **2009**, *21*, 3808-3812.

(93) Zeier, W. G.; Pei, Y.; Pomrehn, G.; Day, T.; Heinz, N.; Heinrich, C. P.; Snyder, G. J.; Tremel, W. *J. Am. Chem. Soc.* **2013**, *135*, 726-732.

(94) Liu, H.; Shi, X.; Kirkham, M.; Wang, H.; Li, Q.; Uher, C.; Zhang, W.; Chen, L. *Mater. Lett.* **2013**, *93*, 121-124.

(95) Ferhat, M.; Nagao, J. *J. Appl. Phys.* **2000**, *88*, 813.

(96) Day, T.; Drymiotis, F.; Zhang, T.; Rhodes, D.; Shi, X.; Chen, L.; Snyder, G. J. *J. Mater. Chem. C* **2013**, *1*, 7568-7573.

(97) Drymiotis, F.; Day, T. W.; Brown, D. R.; Heinz, N. a.; Jeffrey Snyder, G. *Appl. Phys. Lett.* **2013**, *103*, 143906.

(98) Liu, H.; Shi, X.; Xu, F.; Zhang, L.; Zhang, W.; Chen, L.; Li, Q.; Uher, C.; Day, T.; Snyder, G. J. *Nat. Mater.* **2012**, *11*, 422-425.

(99) He, Y.; Day, T.; Zhang, T.; Liu, H.; Shi, X.; Chen, L.; Snyder, G. J. *Adv. Mater.* **2014**, *26*. 3974-3978.

(100) Hermite, E.; Cooper, C. F. *GB patent* 2835, 2836, 1901.

(101) Brown, D. R.; Day, T.; Borup, K. a.; Christensen, S.; Iversen, B. B.; Snyder, G. J. J. *APL Mater.* **2013**, *1* (2013), 052107.

(102) Miyatani, S. Y.; Suzuki, Y. *J. Phys. Soc. Jpn.* **1953**, *8*, 680.

(103) Hinderman, J.D. *Thermoelectric Materials Evaluation Program. Annual technical report for fiscal year* 1979 (Report No. MMM-2331-0642) doi: 10.2172/5741759.

(104) Hinderman, J.D. *SIG Galileo final converter. Technical summary report.* (Report No. DOE/ET/33008-1) (DOE 1979).

(105) Evain, M.; Gaudin, E.; Boucher, F.; Petricek, V.; Taulelle, F. *Acta Crystallogr. Sect. B Struct. Sci.* **1998**, *54*, 376–383.

(106) Gaudin, E.; Boucher, F.; Petricek, V.; Taulelle, F.; Evain, M. *Acta Crystallogr. Sec. B Struct. Sci.* **2000**, *56*, 402–408.

(107) Gaudin, E.; Petricek, V.; Boucher, F.; Taulelle, F.; Evain, M. *Acta Crystallogr. Sect. B Struct. Sci.* **2000**, *56*, 972–979.

(108) Beeken, R. B.; Driessen, C. R.; Hinaus, B. M.; Pawlisch, D. E. *Solid State Ion.* **2008**, *179*, 1058-1060.

(109) Beeken, R. B.; Driessen, C. R.; Wilson, L. a. *J. Phys. Chem. Solids* **2009**, *70*, 1181–1184.

(110) Beeken, R. B.; Hinaus, B. M. *J. Phys. Chem. Solids* **2011**, *72*, 1081-1084.

(111) Deiseroth, H.-J.; Kong, S.-T.; Eckert, H.; Vannahme, J.; Reiner, C.; Zaiss, T.; Schlosser, M. *Angew. Chem., Int. Ed.* **2008**, *47*, 755-758.

(112) Rao, R. P.; Adams, S. *Phys. Status Solidi* **2011**, *208*, 1804-1807.

(113) Nilges, T.; Pfitzner, A. *Z. Krist.* **2005**, *220*, 281-294.

(114) Hahn, H.; Schulze, H.; Sechser, L. *Naturwissenschaften* **1965**, *52*, 451.

(115) Sorokin, G. P.; Papshev, Y. M. and Oush P. T. *Sov. Phys., Solid State* **1966**, *7(7)*, 1810-1811.

(116) Chatov, V. A., Iorga, T. P. & Inglizyan, P. N. *Fiz. Tekh. Poluprovodn.* **1980**, *14*, 807–809.

(117) Boyce, J. B. & Huberman, B. A. Phys. Rep. **1979**, *51*, 189-265.

(118) Kashida, S.; Akai, J. *J. Phys. C Solid State Phys.* **1988**, *21*, 5329-5336.

(119) Borchert, W. *Z. Kristallogr*. **1954**, *106* (1), 5-25.

(120) Stevels A. L. N.; Jellinek, F. *Rec. Trav. Chim. Pays-Bas* **1971**, *90 (3)*, 273-283.

(121) Murray, R. M.; Heyding, R. D. *Can. J. Chem.* **1975**, *53*, 878-887.

(122) Vučić, Z.; Milat, O.; Horvatić, V.; Ogorelec, Z. *Phys. Rev. B* **1981**, *24* (9), 5398-5401.

(123) Yamamoto, K.; Kashida, S. *J. Solid State Chem.* **1991**, *93*(1), 202-211.

(124) Hall, R. B.; Meakin, J. D. *Thin Solid Films* **1979**, *63*, 203.

(125) Bragagnolo, J.; Barnett, A. M.; Phillips, J. E.; Hall, R. B.; Rothwarf, A.; Meakin, J. D. *IEEE Trans. Electron. Dev.* **1980**, *27*(4), 645.

(126) Ishikawa, T.; Miyatani, S.Y. *J. Phys. Soc. Jpn.* **1977**, *42*, 159-167.

(127) El Akkad, F.; Mansour, B.; Hendeya, T. *Mater. Res. Bull.* **1981**, *16*, 535.

(128) Hahn, H.; Schulze, H.; Sechser, L. *Naturwissenschaften* **1965**, *52*, 451.

(129) Kuhs, W. F.; Schulte-Kellinghaus, M.; Krämer, V.; Nitsche, R. *Z. Naturforsch.* **1977**, *32b*, 1100-1101.

(130) Kuhs, W. F.; Nitsche, R.; Scheunemann, K. *Mat. Res. Bull.* **1979**, *14*, 241-248.

(131) Evain, M.; Gaudin, E.; Boucher, F.; Petricek, V.; Taulelle, F. *Acta Crystallogr. Sect. B Struct. Sci.* **1998**, *54* (4), 376–383.

(132) Andrae, H.; Blachnik, R. *J. Therm. Anal.* **1993**, *39*, 1031.

(133) Tripathi, M. N.; Bhandari, C. M. *J. Phys. Condens. Matter*, **2003**, *15*(31), 5359.

(134) Joshi, G.; Lee, H.; Lan, Y.; Wang, X.; Zhu, G.; Wang, D.; Ren, Z. *Nano lett.* **2008** *8*(12), 4670-4674.

(135) Dughaish, Z. H. *Physica B: Condensed Matter*, **2002**, *322*(1), 205-223.

(136) Mastronardi, K.; Young, D.; Wang, C. C.; Khalifah, P.; Cava, R. J.; Ramirez, A. P. *Appl. Phys. Lett.* **1999**, *74*(10), 1415-1417.

(137) Chen, S.; Ren, Z. *Mater. Today*, **2013**, *16*(10), 387-395.

(138) Poudel, B.; Hao, Q.; Ma, Y.; Lan, Y.; Minnich, A.; Yu, B.; Ren, Z. *Science*, **2008**, *320*(5876), 634-638.

(139) Smith, G. E.; Wolfe, R. *J. Appl. Phys.* **1962**, *33*(3), 841-846.

(140) Forman, S. A.; Peacock, M. A. *Am. Mineral.* **1949**, *34*(5-6), 441-451.

(141) Lamarche, a. M.; Woolley, J. .; Lamarche, G.; Swainson, I. .; Holden, T. *J. Magn. Magn. Mater.* **1998**, *186*(1-2), 121-128.

(142) Vaipolin, A. A.; Prochukhan, V. D.; Rud, V. Yu.; Skoriukin, V. E. *Izv. Acad. Nauk. SSSR Neorg. Mater.* **1984**, *20*, 578.

(143) Heyding, R. D. *Can. J. Chem.* **1966**, *14*, 1233.1236.

(144) LaLonde, A. D.; Ikeda, T.; Snyder, G. J. *Rev. Sci. Instrum.* **2011**, *82*, 025104.

(145) Coelho, A. A. *TOPAS-Academic V4.1, Coelho Software; Brisbane,* Australia, 2007.

(146) Coelho, A. A. *TOPAS-Academic V5, Coelho Software*; Brisbane, Australia, 2012.

(147) Puri, S.; Chand, B.; Mehta, D.; Garg, M.L.; Singh, N.; Trehan, P.N. *Atomic Data and Nuclear Data Tables*; **1995**, *61*, 289.

(148) Fleurial, J. P.; Gailliard, L.; Triboulet, R.; Scherrer, H.; Scherrer, S. *J. Phys. Chem. Solids* **1988**, *49*(10), 1237-1247.

(149) May, A.; Toberer, E.; Saramat, A.; Snyder, G. *Phys. Rev. B* **2009**, *80* (12), 1-12.

(150) Zevalkink, A.; Zeier, W. G.; Pomrehn, G.; Schechtel, E.; Tremel, W.; Snyder, G. J. *Energy Environ. Sci.* **2012**, *5* (10), 9121.

(151) Zevalkink, A.; Toberer, E. S.; Zeier, W. G.; Flage-Larsen, E.; Snyder, G. J. *Energy Environ. Sci.* **2011**, *4* (2), 510.

(152) Zeier, W. G.; Zevalkink, A.; Schechtel, E.; Tremel, W.; Snyder, G. J. *J. Mater. Chem.* **2012**, *22* (19), 9826.

(153) Skomorokhov, a. N.; Trots, D. M.; Knapp, M.; Bickulova, N. N.; Fuess, H. *J. Alloys Compd.* **2006**, *421* (1-2), 64-71.

(154) Zhao, L.; Wang, X.; Wang, J.; Cheng, Z.; Dou, S.; Wang, J.; Liu, L. *Sci. Rep.* **2015**, *5*, 7671.

(155) Zhao, L.; Wang, X.; Yun, F. F.; Wang, J.; Cheng, Z.; Dou, S.; Wang, J.; Snyder, G. J. *Adv. Electron. Mater.* **2015**, *1*.

(156) Liu, Y.; Yang, J.; Gu, E.; Cao, T.; Su, Z.; Jiang, L.; Yan, C.; Hao, X.; Liu, F.; Liu, Y. *J. Mater. Chem. A* **2014**, *2*(18), 6363.

(157) Wang, W.; Zhang, L.; Chen, G.; Jiang, J.; Ding, T.; Zuo, J.; Yang, Q. *Cryst. Eng. Comm.* **2015**, *17* (9), 1975-1981.

(158) Day, T. W.; Zeier, W. G.; Brown, D. R.; Melot, B. C.; Snyder, G. J. *Appl. Phys. Lett.* **2014**, *105* (17), 172103.

(159) J.F. Moulder, W.F. Stickle, P.E. Sobol and K.D. Bomben in *Handbook of X-ray Photoelectron Spectroscopy*, Physical Electronics Inc., Eden Prairie, 1995.

(160) Pei, Y.; Wang, H.; Snyder, G. J. *Adv. Mater.* **2012**, *24* (46), 6125-6135.

(161) Wang, H.; Pei, Y.; LaLonde, a. D.; Snyder, G. J. *Proc. Natl. Acad. Sci.* **2012**, *109* (25), 9705-9709.

(162) Liu, H.; Yuan, X.; Lu, P.; Shi, X.; Xu, F.; He, Y.; Tang, Y.; Bai, S.; Zhang, W.; Chen, L.; Lin, Y.; Shi, L.; Lin, H.; Gao, X.; Zhang, X.; Chi, H.; Uher, C. *Adv. Mater.* **2013**, *25* (45), 6607-6612.

(163) Wang, H.; Cao, X.; Takagiwa, Y.; Snyder, J. *Mater. Horiz.* **2015**, *2*, 323-329.

(164) Kroeger, F. A.; Vink, H. J. *Solid state physics* **1956,** *3*, 307-435.

(165) Pomrehn, G. S.; Zevalkink, A.; Zeier, W. G.; Van De Walle, A.; Snyder, G. J. *Angew. Chem., Int. Ed.* **2014**, *53* (13), 3422-3426.

(166) Zevalkink, A.; Zeier, W. G.; Cheng, E.; Snyder, J.; Fleurial, J.-P.; Bux, S. *Chem. Mater.* **2014**, *26*, 5710-5717.

(167) Zunger, A. *Appl. Phys. Lett.* **2003**, *83* (1), 57-59.

(168) Goldsmid, H. *Applications of Thermoelectricity* Butler &Tanner Ltd, London, 1960.

(169) Ioffe, A. F. *Semiconductor Thermoelements and Thermoelectric Cooling*; Infosearch: London, 1957.

(170) Wang, H.; Lalonde, A. D.; Pei, Y.; Snyder, G. J. *Adv. Funct. Mater.* **2013**, *23*(12), 1586-1596.

(171) Movchan, S.; Sizov, F.; Tetyorkin, V. *Semicond. Phys., Quantum Electron. Optoelectron.* **1999**, *2*, 84-87.

(172) Li, W. L.; Csathy, G. A.; Tsui, D. C.; Pfeiffer, L. N.; West, K. W. *Appl. Phys. Lett.* **2003**, *83*, 2832.

(173) Chasmar, R. P.; Stratton, R. *J. Electron. Control* **1959**, *7*, 52.

(174) Wang, H.; Pei, Y.; Lalonde, A. D.; Snyder, G. J. in *Springer Series in Materials Science*, *182*, Springer Verlag: Berlin, 2013.

(175) Rasander, M.; Bergqvist, L.; Delin, A. *J. Phys.: Condens. Matter* **2013**, *25*, 125503.

(176) Chattopadhyay, D.; Queisser, H. J. *Rev. Mod. Phys.* **1981**, *53*(4), 745–768.

(177) Madelung, O.; Rossler, U.; Schulz, M. in *Copper selenides (Cu_2Se, $Cu_{2-x}Se$): optical and further properties. Non-Tetrahedrally Bonded Elements and Binary Compounds I*, volume 41C of *Landolt-Börnstein-Group III Condensed Matter*, chapter 77, pages 1-6. Springer Berlin Heidelberg, 1998.

(178) Goldsmid; H. J. in *Proceedings ICT 07: Twenty-sixth international conference on Thermoelectrics*, International Thermoelectrics Society, pages 362-365, 2007.

(179) Zeier, W. G.; LaLonde, A.; Gibbs, Z. M.; Heinrich, C. P.; Panthöfer, M.; Snyder, G. J.; Tremel, W. *J. Am. Chem. Soc.* **2012**, *134* (16), 7147–7154.

(180) Lee, P.; Ramakrishnan, T. *Rev. Mod. Phys.* **1985**, *57*, 287–337.

(181) Cahill, D.; Watson, S.; Pohl, R. *Phys. Rev. B* **1992**, *46*.

(182) Chiritescu, C.; Cahill, D. G.; Nguyen, N.; Johnson, D.; Bodapati, A.; Keblinski, P.; Zschack, P. *Science* **2007**, *315*, 351–353.

(183) Boyce, J. B.; Huberman, B. a. *Phys. Rep.* **1979**, *51* (4), 189-265.

(184) Scherrer, H. and Scherrrer, S. *Thermoelectics Handbook: Macro to Nano*, chapter 27. CRC Press LLC, Boca Raton 2006.

(185) Fleurial, J. P.; Gailliard, L.; Triboulet, R.; Scherrer, H.; Scherrer, S. *J. Phys. Chem. Solids* **1988**, *49* (10), 1237-1247.

(186) Forman, S. A.; Peacock, M. A. *Am. Mineral.*, **1949**, *34*, 441.

(187) Pertlik, F. *Anz. Oesterr. Akad. Wiss., Math.-Naturwiss. Kl.* **1986**, 123, 123.